Title: Advanced Technologies for Monitoring CO_2 Saturation and Pore Pressure in Geologic Formations: *Linking the Chemical and Physical Effects to Elastic and Transport Properties*

FINAL TECHNICAL REPORT

Reporting period start date:	October 1, 2009
Reporting period end date:	March 31, 2014
Authors:	G. Mavko (PI), T. Vanorio, S. Vialle, N. Saxena
Report date:	June 2014

DOE Award Number: DE-FE0001159 (SPO #46198)

Recipient: Stanford University, Stanford, California 94305-2215

ABSTRACT

Ultrasonic P- and S-wave velocities were measured over a range of confining pressures while injecting CO_2 and brine into the samples. Pore fluid pressure was also varied and monitored together with porosity during injection. Effective medium models were developed to understand the mechanisms and impact of observed changes and to provide the means for implementation of the interpretation methodologies in the field.

Ultrasonic P- and S-wave velocities in carbonate rocks show as much as 20-50% decrease after injection of the reactive CO_2-brine mixture; the changes were caused by permanent changes to the rock elastic frame associated with dissolution of mineral. Velocity decreases were observed under both dry and fluid-saturated conditions, and the amount of change was correlated with the initial pore fabrics. Scanning Electron Microscope images of carbonate rock microstructures were taken before and after injection of CO_2-rich water. The images reveal enlargement of the pores, dissolution of micrite (micron-scale calcite crystals), and pitting of grain surfaces caused by the fluid-solid chemical reactivity. The magnitude of the changes correlates with the rock microtexture – tight, high surface area samples showed the largest changes in permeability and smallest changes in porosity and elastic stiffness compared to those in rocks with looser texture and larger intergranular pore space.

Changes to the pore space also occurred from flow of fine particles with the injected fluid. Carbonates with grain-coating materials, such as residual oil, experienced very little permanent change during injection.

In the tight micrite/spar cement component, dissolution is controlled by diffusion: the mass transfer of products and reactants is thus slow and the fluid is expected to be close to thermodynamical equilibrium with the calcite, leading to very little dissolution, or even precipitation. In the microporous rounded micrite and macropores, dissolution is controlled by advection: because of an efficient mass transfer of reactants and products, the fluid remains acidic, far from thermodynamical equilibrium and the dissolution of calcite is important. These conclusions are consistent with the lab observations.

Sandstones from the Tuscaloosa formation in Mississippi were also subjected to injection under representative in situ stress and pore pressure conditions. Again, both P- and S-wave velocities decreased with injection. Time-lapse SEM images indicated permanent changes induced in the sandstone microstructure by chamosite dissolution upon injection of CO_2-rich brine. After injection, the sandstone showed an overall *cleaner* microstructure. Two main changes are involved: (a) clay dissolution between grains and at the grain contact and (b) rearrangement of grains due to compaction under pressure

Theoretical and empirical models were developed to quantify the elastic changes associated with injection. Permanent changes to the rock frame resulted in seismic velocity-porosity trends that mimic natural diagenetic changes. Hence, when laboratory measurments are not available for a candidate site, these trends can be estimated from depth trends in well logs. New theoretical equations were developed to predict the changes in elastic moduli upon substitution of pore-filling material. These equations reduce to Gassmann's equations for the case of constant frame properties, low seismic frequencies, and fluid changes in the pore space. The new models also predict the change in elastic moduli upon dissolution or precipitation of mineral, which cannot be described with the conventional Gassmann theory.

TABLE OF CONTENTS

EXECUTIVE SUMMARY

The primary goal of the proposed research is to provide robust methodologies for quantitatively interpreting subsurface CO_2 saturation and state from seismic data. These methodologies will allow quantitative mapping of the movement, presence, and permanence of CO_2 relative to its intended storage location at injection sites. In spite of advanced techniques for geophysical imaging, current methods for interpreting CO_2 saturation from seismic data can be fundamentally flawed. Until now, Gassmann's equations, which relate pore fluid compressibility and the rock frame to overall elastic properties, have been the primary tool for interpreting CO_2 plumes from time-lapse seismic data. Gassmann's model is purely mechanical, and is best suited for conditions of single-phase fluid saturation in relatively inert systems. Yet, CO_2-rich fluid-rock systems can be chemically reactive, altering the rock frame via dissolution, precipitation, and mineral replacement. Furthermore, CO_2 systems are multiphase, with uncertainties in scales of phase mixing in the pore space and solution of one phase in another. Errors from ignoring the physicochemical factors during CO_2 injection can affect not only the magnitude, but also the sign, of predicted seismic velocity changes, resulting in seriously compromised estimates of saturation and pressure of CO_2-rich fluids. This research aims to provide CO_2-optimized rock-fluid models that incorporate the seismic signatures of (1) *saturation scales and free vs. dissolved gas in a CO_2-water mixing*, (2) pore pressure changes, and (3) *CO_2-induced chemical changes to the host rock.*

This research has involved laboratory and theoretical tasks in the field of Rock Physics. Measurements of the geochemical properties of the CO_2-rich fluids and their evolution during the acoustic experiments were made to link the chemical and the physical changes occurring in the rock samples during the injection. High resolution microCT scans were made to image changes to the pore space associated with the injection. Samples were selected based on mineralogy (carbonates, clean sandstones, shaley-sandstones, and calcite-cemented sandstones), microstructure, porosity, pore type, and permeability to understand the control of these factors on induced changes of seismic velocity. Ultrasonic P- and S-wave velocities were measured over a range of confining pressures while injecting CO_2 and brine into the samples. Pore fluid pressure was also varied and monitored together with porosity during injection. Effective medium models were developed to understand the mechanisms and impact of observed changes and to provide the means for implementation of the interpretation methodologies in the field.

Ultrasonic P- and S-wave velocities in carbonate rocks show as much as 20-50% decrease after injection of the reactive CO_2-brine mixture; the changes were caused by permanent changes to the rock elastic frame associated with dissolution of mineral. Velocity decreases were observed under both dry and fluid-saturated conditions, and the amount of change was correlated with the initial pore fabrics. Scanning Electron Microscope images of carbonate rock microstructures were taken before and after injection of CO_2-rich water. The images reveal enlargement of the pores, dissolution of micrite (micron-scale calcite crystals), and pitting of grain surfaces caused by the fluid-solid chemical reactivity. The experiments illustrate that the magnitude of the changes

correlates with the rock microtexture – tight, high surface area samples showed the largest changes in permeability and smallest changes in porosity and elastic stiffness compared to those in rocks with looser texture and larger intergranular pore space.

Changes to the pore space also occurred from flow of fine particles with the injected fluid. Carbonates with grain-coating materials, such as residual oil, experienced very little permanent change during injection.

In order to relate type of microstructure to flow paths, permeability and reactivity, the carbonate rock samples were subdivided into different components, applying definitions in the literature to the qualitative analysis of SEM images and mercury intrusion tests. Order of magnitude estimates for the Péclet numbers of each rock component were made by taking similar conditions as in the experiments. In the tight micrite/spar cement component, dissolution is controlled by diffusion: the mass transfer of products and reactants is thus slow and the fluid is expected to be close to thermodynamical equilibrium with the calcite, leading to very little dissolution, or even precipitation. In the microporous rounded micrite and macropores, dissolution is controlled by advection: because of an efficient mass transfer of reactants and products, the fluid remains acidic, far from thermodynamical equilibrium and the dissolution of calcite is important. These conclusions are consistent with the lab observations.

Sandstones from the Tuscaloosa formation in Mississippi were also subjected to injection under representative insitu stress and pore pressure conditions. Again, both P- and S-wave velocities decreased with injection. Time-lapse SEM images indicated permanent changes induced in the sandstone microstructure by chamosite dissolution upon injection of CO_2-rich brine. After injection, the sandstone shows an overall *cleaner* microstructure. Two main changes are involved: (a) clay dissolution between grains and at the grain contact and (b) rearrangement of grains due to compaction under pressure

Theoretical and empirical models were developed to quantify the elastic changes associated with injection. Permanent changes to the rock frame resulted in seismic velocity-porosity trends that mimic natural diagenetic changes. Hence, when laboratory measurments are not available for a candidate site, these trends can be estimated from depth trends in well logs. New theoretical equations were developed to predict the changes in elastic moduli upon substitution of pore-filling material. These equations reduce to Gassmann's equations for the case of constant frame properties, low seismic frequencies, and fluid changes in the pore space. The new models also predict the change in elastic moduli upon dissolution or precipitation of mineral, which cannot be described with the conventional Gassmann theory.

REPORT DETAILS

INTRODUCTION:

Until now, modeling of pore fluid effects on seismic data has been based almost exclusively on Gassmann's equations (Gassmann, 1951), which describe the interaction of fluid compressibility and rock frame to determine the overall elastic behavior of the rock. In a seismic monitoring scenario, Gassmann's theory quantifies changes in rock seismic velocity and impedance, caused by changes in fluid compressibility associated with variations in saturation, free and dissolved gas, pore pressure, and temperature. Gassmann modeling has been used to interpret CO_2 plumes from time-lapse seismic data at several storage sites (e.g. Arts et al., 2000, 2004; Eiken et al., 2000, Chadwick et al., 2005; Daley et al., 2007; Van der Meer et al., 2001). The problem is that Gassmann's model, being purely mechanical (Mavko et al, 2009), is best suited for conditions of **single-phase fluid saturation** in relatively **inert systems**, in which the pore fluids and minerals are at, or close to, chemical equilibrium. Yet, CO_2-rich fluid-rock systems can be chemically reactive, altering the rock frame via dissolution, precipitation, and mineral replacement. Errors from ignoring the physicochemical processes during CO_2 injection can affect not only the magnitude, but also the sign, of predicted seismic velocity changes, resulting in seriously compromised estimates of saturation and pressure of CO_2-rich fluids. Other factors that can interfere with accurate mapping of CO_2 distributions and saturation are ambiguities in the seismic signatures of free vs. dissolved gas in a CO_2-water system, effective stress, and scales of CO_2-water saturations (ie., fine-scale vs. *patchy* saturation) in the pore space.

Management and control of multiphase subsurface flow associated with CO_2 injection pose formidable uncertainties and risks. We believe that geophysical interpretations of at least some previous CO_2 pilot studies may have been seriously flawed, since they ignored chemical effects, as well as uncertainties in fluid properties and saturation heterogeneity (e.g. "patchy" vs. "uniform" saturation). Classical fluid substitution schemes very likely oversimplify the complex rock-fluid interactions that occur while injecting CO_2 underground and hence, are inadequate for measuring the effects of CO_2-bearing reactive fluids on in-situ seismic velocities. This project's goal of providing, for the first time, the

fundamental understanding necessary to simultaneously model geophysical signatures of chemical and physical reservoir responses to CO_2 injection represents a necessary major step forward in the technology for management and monitoring of CO_2 sequestration.

The primary goal of the project is to provide robust CO_2-optimized physical-chemical models for quantitatively interpreting subsurface CO_2 saturation and state from seismic data. These methodologies will allow quantitative mapping of the movement, presence, and permanence of CO_2 relative to its intended storage location. This overall goal entails two specific research objectives:

1) Understand the seismic signatures of pore pressure, free gas versus dissolved gas and scales of gas-liquid saturations in CO_2-water systems, as well as the conditions that control these saturation states.

2) Determine the impact of fluid-solid chemical reactions on the rock frame and measurable rock elastic properties.

APPROACH:

This research involves laboratory and theoretical tasks in the field of Rock Physics. Measurements of the cation concentration of the CO_2-rich fluids and their evolution during the acoustic experiments were performed to link the chemical and the physical changes occurring in the rock samples during the injection. Samples studied include carbonates, clean sandstones, and calcite-cemented, iron-rich sandstones from Tuscaloosa formation, Mississippi. High-resolution SEM images were taken in addition to porosity and permeability measurements to assess changes to the pore space and microstructure associated with the injection. Ultrasonic P- and S-wave velocities were measured over a range of confining pressures while injecting CO_2 and brine into the samples. Pore fluid pressure was also varied and monitored together with porosity during injection.

Effective medium models were developed to understand the mechanisms and impact of observed changes and to provide the means for implementation of the interpretation methodologies in the field.

LABORATORY MEASUREMENTS OF ROCK PROPERTY CHANGES DURING CO_2 INJECTION

[*key publications: Joy et al. 2011; Vanorio, et al., 2011; Vanorio and Mavko, 2011; Vialle and Vanorio, 2011; Grombacher, et al., 2012*]

A methodical laboratory study was undertaken to discover and understand the geophysical response of reservoir and aquifer rocks to injection of CO_2 and CO_2-bearing brine. Samples studied included carbonates with a range of microstructures, plus sandstones, with compositions ranging from clean sandstones to calcite-cemented and clay-bearing sandstones from Tuscaloosa formation, Mississippi. Changes of porosity, permeability, and elastic properties were monitored and combined with high resolution imaging to reveal chemical and physical changes that can affect fluid transport and that can have distinct seismic signatures from geophysical remote sensing.

The objective of the work was not to simulate exact 3D aquifer systems, but rather to recognize, quantify, and understand changes to the rock that can occur when fluid injection causes changes to local stresses and disturbs chemical equilibrium.

The experimental device, shown schematically in Figure 1, consists of a circuit for fluid injection and a high pressure vessel, equipped with three linear potentiometers to measure length changes of the samples as a function of stress, and with two pairs of transducers for the measurement of P- and S-wave velocities.

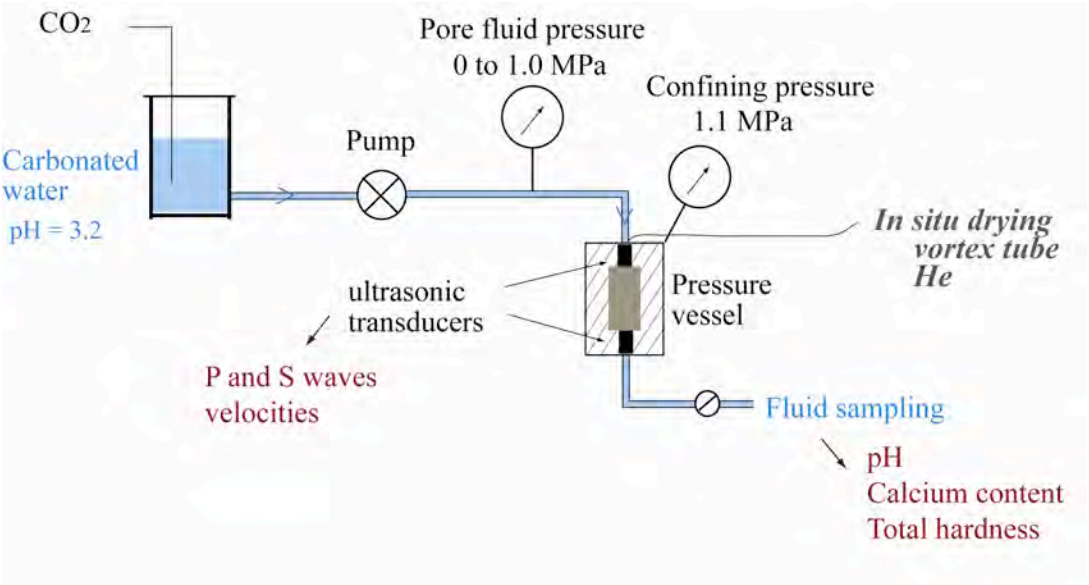

Figure 1: Experimental device scheme. The device consists of a circuit for fluid injection and a pressure vessel equipped with a pair of transducers for the measurement of P- and S-wave velocities, under both saturated and *in situ* dry conditions. Fluids can be sampled for chemical analysis.

The acoustic setup consists of a pulse generator (Panametrics 5052 PR), a digital oscilloscope (Tektronix TDS 420 A) and two pairs of transducers (Panametrics V103 for 1 MHz P-waves and V154 for 0.7 MHz for S-waves) that are piezoelectric crystals in lead-zirconate-titanate (PZT). These crystals are mounted on steel endplates, and a high-viscosity bonding medium (molasses) is used to ensure good coupling between the sample and the endplates.

The pulse transmission technique (Birch, 1960) was used for the measurements of P- and S-wave velocities. The time a wave takes to propagate from the top of the sample to the bottom was measured after digitizing each trace with 1024 points at a time sweep of 5 μs, thus allowing a time resolution of about 5 ns (corresponding to 0.2% error in velocity). The velocities were estimated by the following relation

$$V = \frac{(L_0 - \delta L)}{(\tau_m + \Delta\tau_1 - \Delta\tau_0)} \qquad (1)$$

where L_0 is the initial length of the sample (at atmospheric pressure), δL is the change of length due to pressurization, τ_m is the measured travel time, $\Delta\tau_1$ is the trigger delay time, and $\Delta\tau_0$ is the system delay time. This system delay time was measured by taking the

head-to-head time at 2MPa and confirmed by measuring an aluminum cylinder at different pressures. Error in velocity measurements was estimated to be about 1%, mainly due to operator error in picking first arrival time.

The sample was jacketed with rubber tubing to isolate it from the confining-pressure medium and inserted into the high pressure chamber. For carbonate samples a confining pressure of 1.1 MPa was generated, and a first measurement of P- and S-wave velocities was made. Measurements on sandstone were made under effective stresses representative of the Tuscaloosa formation (Mississippi), where samples originated. (More details on the sandstone measurements are described below.)

A pore fluid inlet in each end plate allowed pore fluid passage through the sample. Fluids were contained in a main reservoir. To promote the dissolution of the carbonate minerals, an acidic solution was prepared by saturation of deionized water with CO_2, at a pH of about 3.3, measured before each injection.

For the carbonates, the injection protocol was designed to simulate conditions that fall between those typical of a closed injection system and those typical of a continuous flow-through experiment. Rates of depletion were set lower than rates of injection, resulting in a flow rate of 4 to 8 mL/min. This allowed the sample to be always fully saturated and the dissolution to be homogeneous. Then, P- and S-wave velocities were acquired under full saturation conditions and pore fluid pressure of 1.0MPa. Before proceeding with the next injection, the sample was dried in the vessel for about 10h, by alternating the injection of warm, dry air and dry helium. P- and S-wave velocities under *in situ* dry conditions were then obtained.

The fluid was regularly sampled at the outlet and collected in a 15mL glass tube, in order to measure calcium content and total hardness (which is the concentration of calcium, magnesium and all the other polyvalent ions which can be substituted in the calcite crystal lattice). Concentrations were determined by a complexometric titration method with a digital titrator (HACH LANGE 16900) and a 0.08M EDTA (Ethylenediaminetetraacetic acid) solution as titrant. Measurements were made both immediately after sampling and then 48 hours later in samples in which two drops of concentrated HNO_3 had been added. The results indicated that the effluent contained minerals dissolved from the rock samples, as well as fines that were flushed from the pore space.

The analytical procedure involves the determination of both total hardness and calcium concentration, using the chelating agent EDTA. First, the titration is conducted under conditions where all the polyvalent ions counting in total hardness react with the EDTA solution. Then by conducting the titration at high pH (about 13), only calcium content is measured.

The digital titrator was equipped with the titrant cartridge and a capillary. 1 mL of the fluid sample was then taken with a high precision micropipette, transferred to a 250 mL Erlenmeyer, then topped with deionized water to about 100 mL.

The procedure for total hardness measurement is then the following: 2mL of Hardness 1 Buffer Solution (to maintain the pH at about 10) and then the content of one ManVer 2 Indicator powder pillow were added, and the solution was swirled. The EDTA titrant was added drop by drop until the color changed from pink to pure blue.

Total hardness (C_{TH}, in mg/L as $CaCO_3$) is given by

$$C_{TH}(mgl.L^{-1} as\ CaCO_3) = Nb_{units} \cdot \frac{100}{V_{ech}(mL)} \cdot \frac{C_{EDTA}(mol.L^{-1})}{0.8}, \tag{2}$$

where Nb_{units} is the number of units read on the apparatus, C_{EDTA}, the concentration of EDTA (in mol/L) and V_{ech} the volume of the sample (in mL).

The procedure for calcium content is similar: 2 mL of 8N Potassium Hydroxide Standard Solution (to raise the pH to about 13) and then the content of one CalVer 2 Indicator powder pillow were added while swirling the solution. It was titrated until the color changed from pink to blue.

Calcium content (C_{Ca}, in $mg.L^{-1}$) is given by

$$C_{Ca}(mg.L^{-1}) = Nb_{units} \cdot \frac{100}{V_{ech}(mL)} \cdot \frac{C_{EDTA}(mol.L^{-1})}{0.8} \cdot 0.4. \tag{3}$$

The maximum experimental uncertainty of the concentrations is given by

$$\frac{\Delta C}{C} = \frac{\Delta N_b}{N} + \frac{\Delta V_{ech}}{V_{ech}} + \frac{\Delta C_{EDTA}}{C_{EDTA}}, \tag{4}$$

where C is either total hardness or calcium concentration.

The EDTA solutions are commercial solutions whose concentration is precise at 0.5 %. Error in sample volume depends on the precision of the micropipette. Error in the number of units depends on both the intrinsic precision of the titrator, which is 1%, and on determining the point at which the color of the solution changes. The maximum relative uncertainty was thus about 4%.

Observations on Carbonates

For the carbonate portion of the study, we selected samples from the Monte Acuto formation, which belongs to the Upper Cretaceous carbonate systems of the Gargano-Murge region, a part of the stable foreland of Southern Italy. The Monte Acuto formation dates to the Late Cretaceous (Martini and Pavan, 1967; Cremonini et al., 1971). Samples consist of white, chalky and cherty lime mudstones alternating with coarse bioclastic calciturbidites, breccias and megabreccias. The mineralogical composition, determined by X-Ray Diffraction (XRD) (Marco Voltolini, Berkeley University, *personal communication*), is nearly 100% calcite.

Microstructure was studied by different and complementary techniques to examine its role on the physical chemical imbalances. Techniques used were Scanning Electron Microscopy (SEM), mercury intrusion porosimetry (MIP) and microtomography.

The scanning electron microscope is a Hitachi 3400N, used in the Variable Pressure (VP-SEM) mode. It allows charge-up-free observation without coating the surface's sample, yet with a good resolution.

Figure 2 shows a microcrystalline calcite matrix (i.e. micrite) composed of anhedral to subhedral rounded grains, whose size is typically 1 to 4 μm. Contacts between crystals are generally punctic, sometimes serrate. Micrite crystals are surrounded by sparry carbonate cement (i.e. sparite). Spar crystals are subhedral to euhedral, and their edges and corners are generally smooth. As qualitatively observed in Figure 2, this chalky matrix is the main component of the pore system. The method developed by Vanorio et al. (2008), using microtomography scans and image-processing techniques, gives a micrite volume fraction of 26 to 48%, depending on the sample.

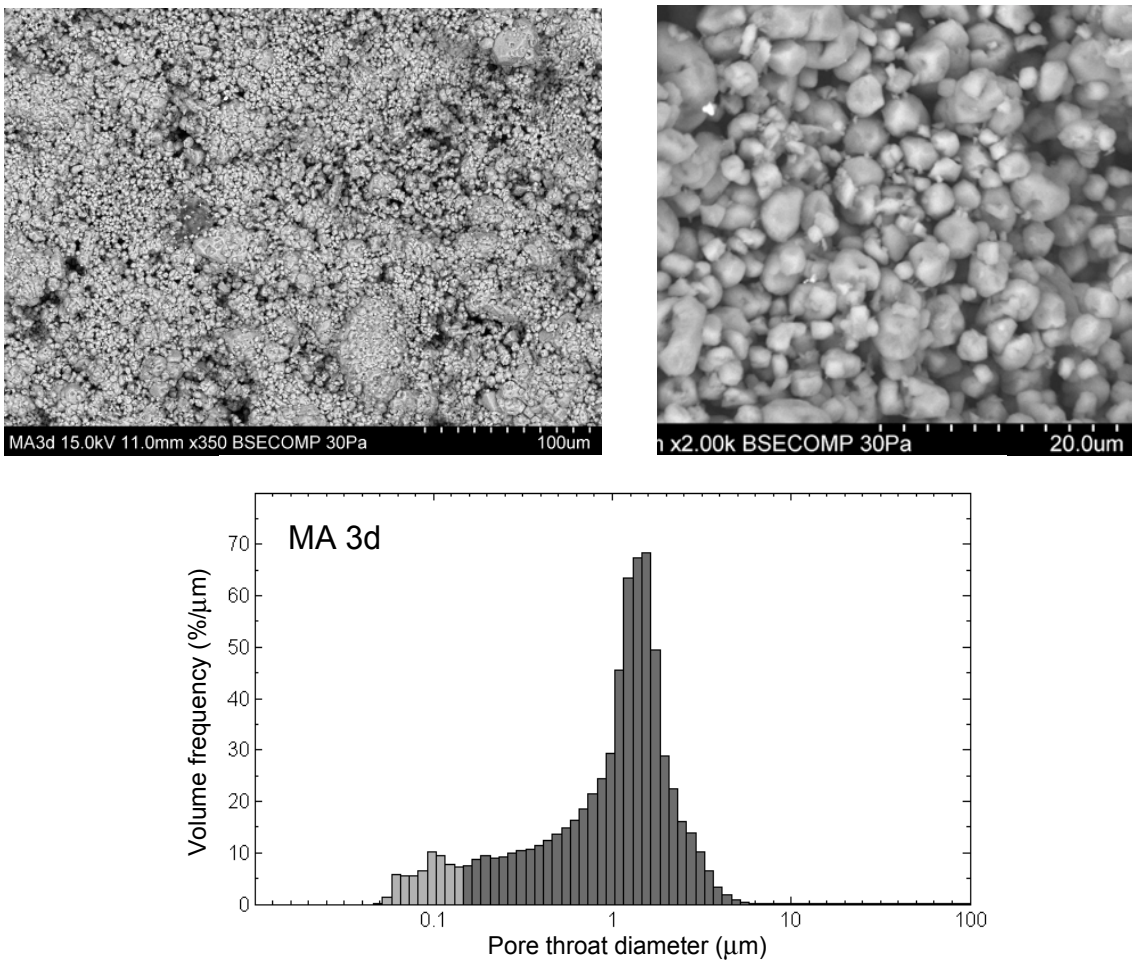

Figure 2: Top: SEM image of the surface of one of the studied sample (left), showing the micrite calcite matrix surrounded by bigger calcite grains (sparry calcite cement); a magnified view of the microporous matrix is shown on the right; Bottom: pore size distribution obtained from mercury capillary pressures.

The pore-size distributions, obtained by mercury intrusion porosimetry (Figure 2), show pore throats (or pore entries) essentially centered on a main peak in the micron-sized range. These distributions are thus quasi-monomodal, yet with a broad range of very small pore throats, as small as 0.048 µm. Microporosity in these samples, defined as pores and pore throats less than 10 µm, is therefore high, accounting for more than 60% of total porosity.

Helium porosity (with an uncertainty of ± 1%) and Klinkerberg-corrected air permeability (with an uncertainty of ± 2%) were measured under room pressure and temperature conditions. The values are respectively 23.6-26.5% and 5-135 mD.

Figure 3 shows results for ultrasonic P- and S-wave velocities vs. volume of injected CO_2-rich brine in a limestone sample. Initial dry-rock measurements are shown by the open symbols along the left vertical axis. The horizontal axis shows the volume of injected fluid, normalized by pore volume. The experiment was made by continuously injecting CO_2-rich brine, stopping occasionally to measure P- and S-wave velocities (indicated by filled symbols), as well as changes in sample length. At injection volumes 520 and 720, the sample was dried while still in the pressure vessel by injecting dry heated air, alternating with dry helium. Measurements of P- and S-wave velocities were made on the dry rocks (open symbols), and then fluid injection was resumed.

The measurements in Figure 3 show decreases of Vp and Vs with continued exposure to the CO_2-rich brine. The decrease is evident for both dry and fluid-saturated samples. These changes represent permanent alteration of the rock, due to chemical dissolution of mineral, as well as flushing of fines from the pore space. Understanding these irreducible changes will be critical for developing an understanding of how CO_2 injection can be monitored with geophysical methods.

Figure 4 shows measured changes to the sample length (shortening) during the experiment. Closed symbols show changes with continued injection while under small effective stress (0.1 MPa). Three open black symbols show drained measurements at effective stress 1.1 MPa. Open red symbols show dry measurements at effective stress 0 MPa. Note how the dry pressure sensitivity is larger after exposure to CO_2-rich brine than before injection. A simple conceptual model is that dissolution occurs at grain contacts, increasing the elastic compliance.

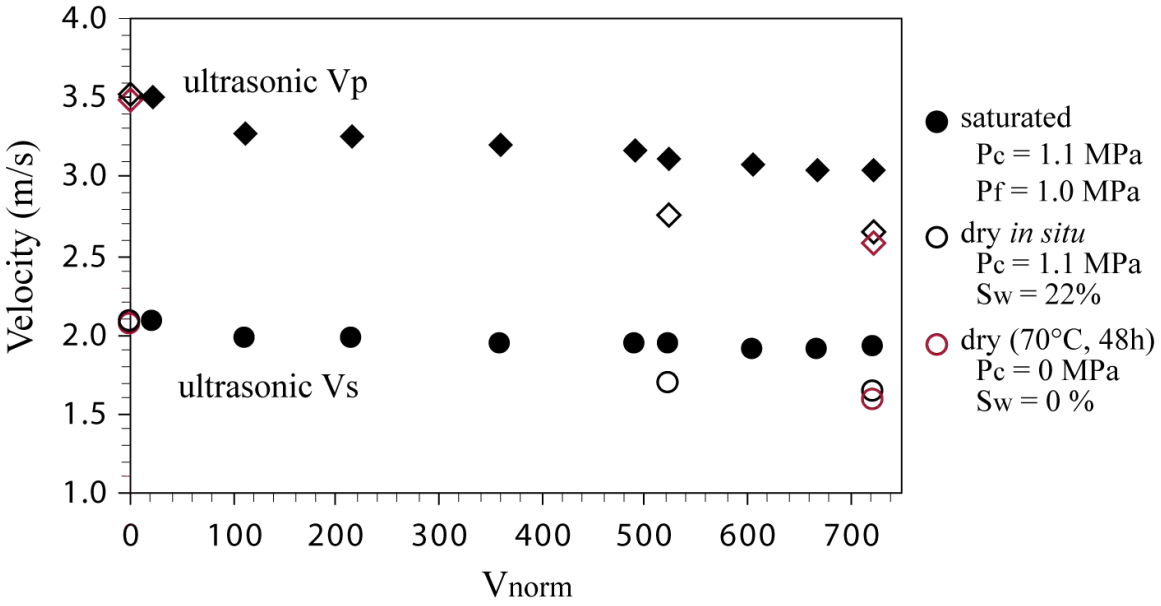

Figure 3. Ultrasonic P- and S-wave velocities vs. volume of injected CO_2-rich brine in a limestone sample. Horizontal axis is the volume of injected fluid, normalized by pore volume. Initial dry-rock measurements are shown by the open symbols along the left vertical axis. Additional open symbols to the right are dry-rock measurements after fluid injection. Closed symbols are observed velocities for saturated samples.

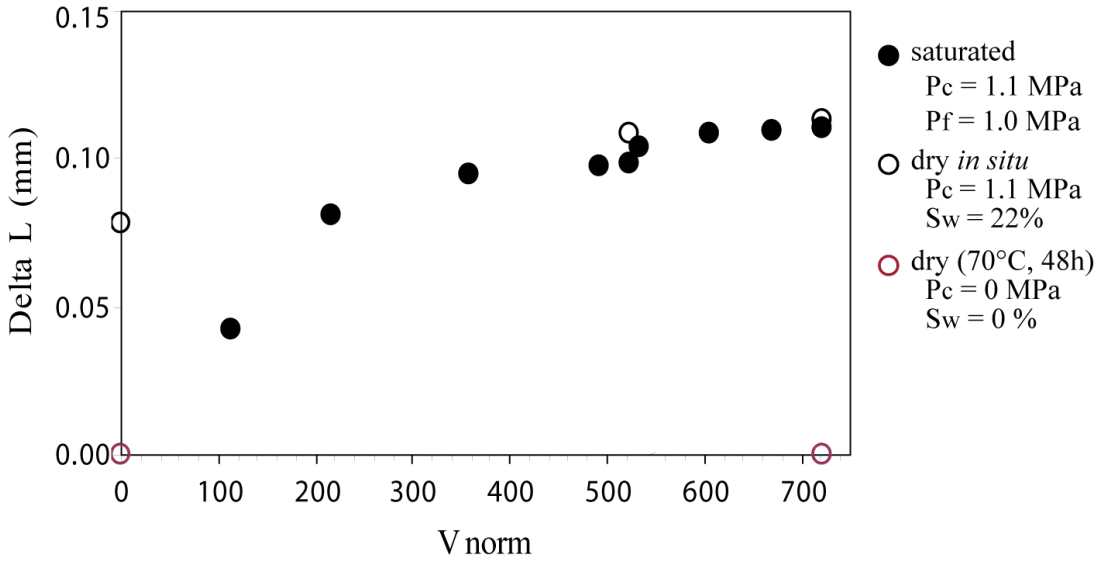

Figure 4. Changes in sample length (shortening) associated with injection of CO_2-rich brine. Point at the original represents the start of the experiment. Closed symbols show changes with continued injection while under small effective stress (0.1 MPa). Three open black symbols show drained measurements at effective stress 1.1 MPa. Open red symbols show dry measurements at effective stress 0 MPa.

The acoustic, hydraulic, and transport properties of the measured samples are summarized in Table 1 and refer to *before* and *after* injection. We also imaged the changes induced in the rock microstructure by using Scanning Electron Microscope (SEM) and CT-scan imaging techniques (Figures 6-8).

Figure 5 shows the variation of the dry and saturated P- and S- wave velocities for six carbonate samples as a function of injected volumes of fluid. Velocity values are normalized with the respect to their pre-injection values. Both P- and S- wave velocities measured under dry (open symbols) and saturated (solid symbols) conditions decrease over time for all measured samples. Although the injection protocol and injected volumes are kept the same, the magnitude of changes differs from one sample to another.

As expected, the different response of the samples to the injection is, as first order, a function of the injected fluid volumes. Nevertheless, for similar injected fluid volumes, the response of the rock seems also be related to its initial microstructure (Figure 6) as well as rock composition. The images reported in Figure 6 refer to samples RU7855A and MA2d, the former showing a tighter microstructure with interlocked calcite grains. These two samples can be seen as two end-members in term of sample microstructure of carbonates.

Changes are interpreted as permanent alteration of the rock as confirmed by SEM imaging. We glued metal wires on the top and bottom of the samples for the purpose of registering the position of samples, thus facilitating the time-lapse comparison of images. Figure 7 compares the SEM images taken before (left panel) and after (right panel) for sample MA2d. Images refer to both the top and bottom of the rock sample (Figure 7a and Figure 7b, respectively). The SEM images have been taken at different magnifications to gain insight into the scale of the observed changes. The images referring to the top of the sample (*i.e.,* injection point) clearly show that changes responsible for the observed variation in the acoustic properties result from a) porosity enhancement, b) different microstructure, and c) removal of finer grain size. Nevertheless, the microstructure of the bottom of the sample (Figure 7b) is clearly less affected by the injection. This observation is consistent with the fact that the pH of the fluid measured both at the inlet

and outlet increases from 3.2 to 6.3 while travelling through the sample being buffered by its reaction with calcite.

Scanning electron microscopy provides a qualitative imaging of the surface of the rock samples. In order to investigate how the whole core volume is modified upon injection we are currently collaborating with Ingrain Inc., Houston, TX to perform a time-lapse (*i.e.,* pre- and post- injection) micro CT-scan imaging of 1" diameter core plugs. In Figure 8 we report one slice of the 3D volume for the sample MA2d that has been imaged before (left panel) and after (right panel) injection. Figure 8 clearly shows the permanent changes to the rock elastic frame mostly due to porosity enhancement.

Table 1: Table summarizing the hydraulic, transport and acoustic properties of six carbonate samples measured before and after injection.

		Before Injection				**After Injection**			
Sample ID	**Injected Volumes***	**Φ (%)**	**k (mD)**	**Vp (m/s)**	**Vs (m/s)**	**Φ (%)**	**k (mD)**	**Vp (m/s)**	**Vs (m/s)**
5139	730	15.4	255	3628	2333	16.4	565	3523	2193
RU7855A	710	25.4	15.3	4095	2383			3917	2111
MA2a	40	28.6	135.3	2745	1488	29.1	140.6	2581	1371
MA2b	25	23.6	4.9	3786	2194	23.7	4.9	3112	1619
MA2d	771	29.8	135.7	3014	1905	33.2	750.5	2403	1397
MA3d	722	26.5	75.3	3528	2088	31.5	448.9	2657	1645

**normalized to the initial pore volume;*

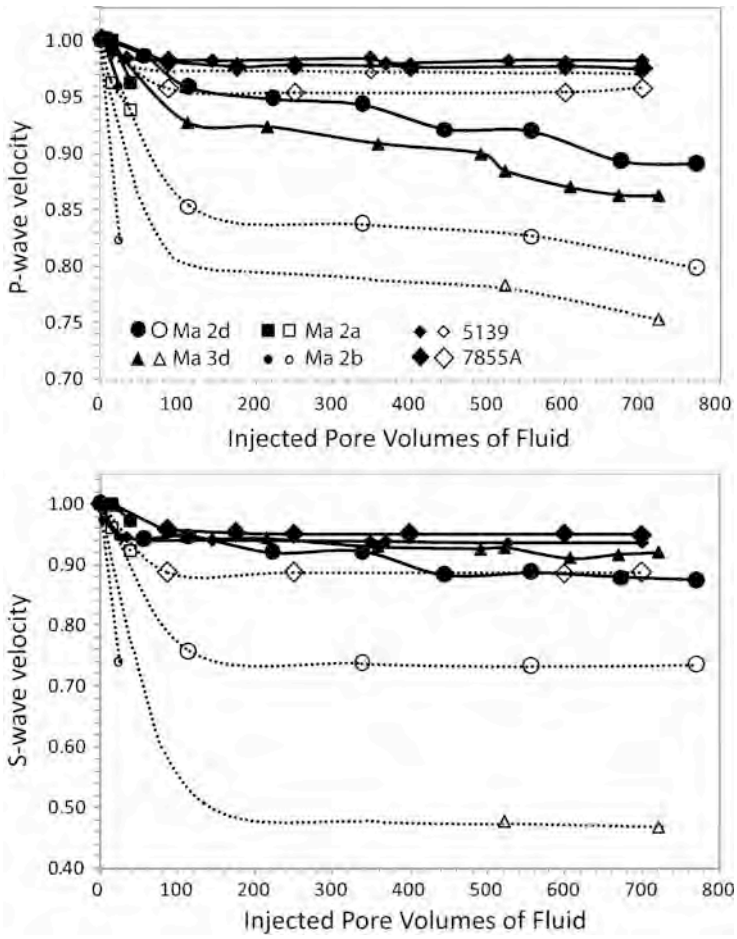

Figure 5. Ultrasonic P- (top panel) and S-wave velocities (bottom panel) vs. volume of injected CO_2-rich brine in carbonate samples. Both P- and S-velocity values are normalized with the respect to their pre-injection values. The horizontal axis is the volume of injected fluid, normalized by pore volume. Open and solid symbols refer to measurements performed under dry and fully saturated conditions.

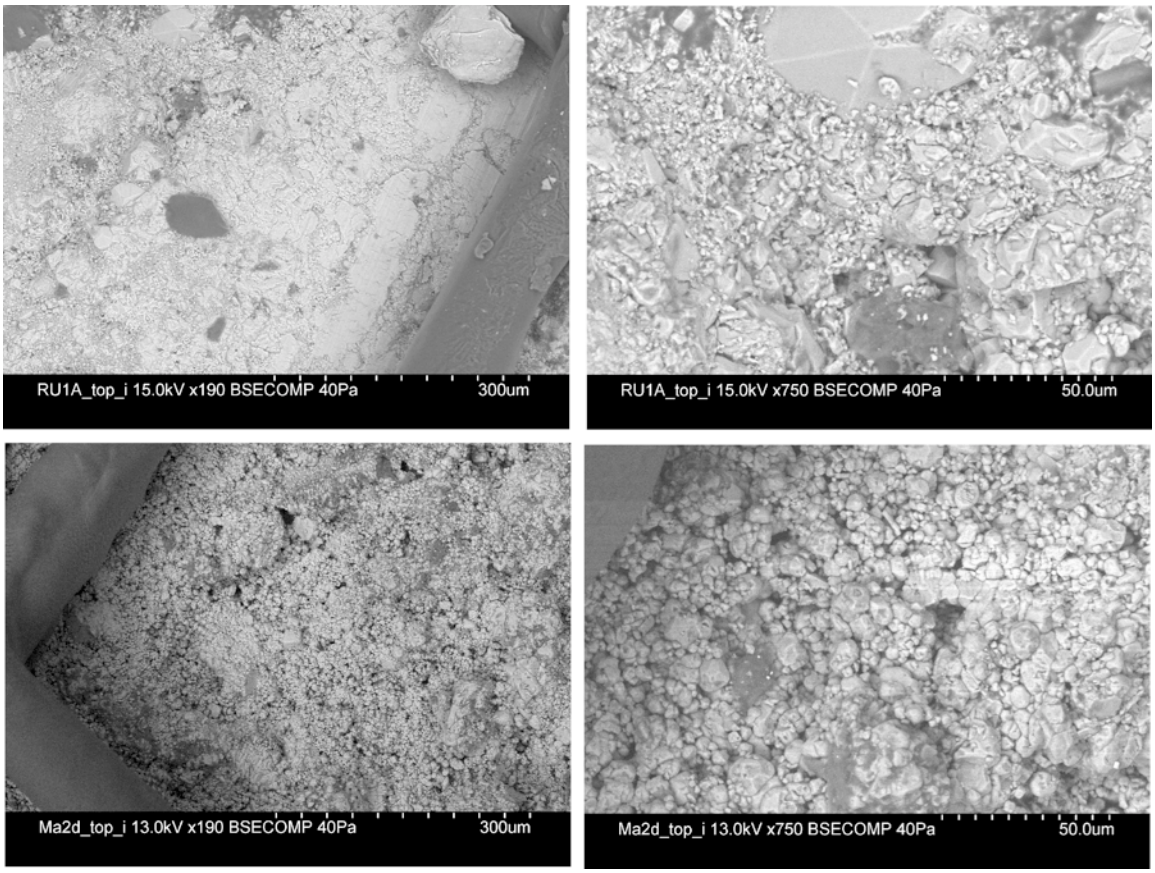

Figure 6. Scanning Electron Microscope images of two rock samples taken before the injection of CO_2-rich water. Optical magnifications are the same for both samples. Samples (RU7855A and MA2d) refer to the two end-members in term of carbonate sample microstructure. This translates into different pre-injection transport properties as well as transport and acoustic response upon injection. The metal wire glued on the sample is for the purpose of registering the position of samples, thus facilitating the time-lapse comparison of images.

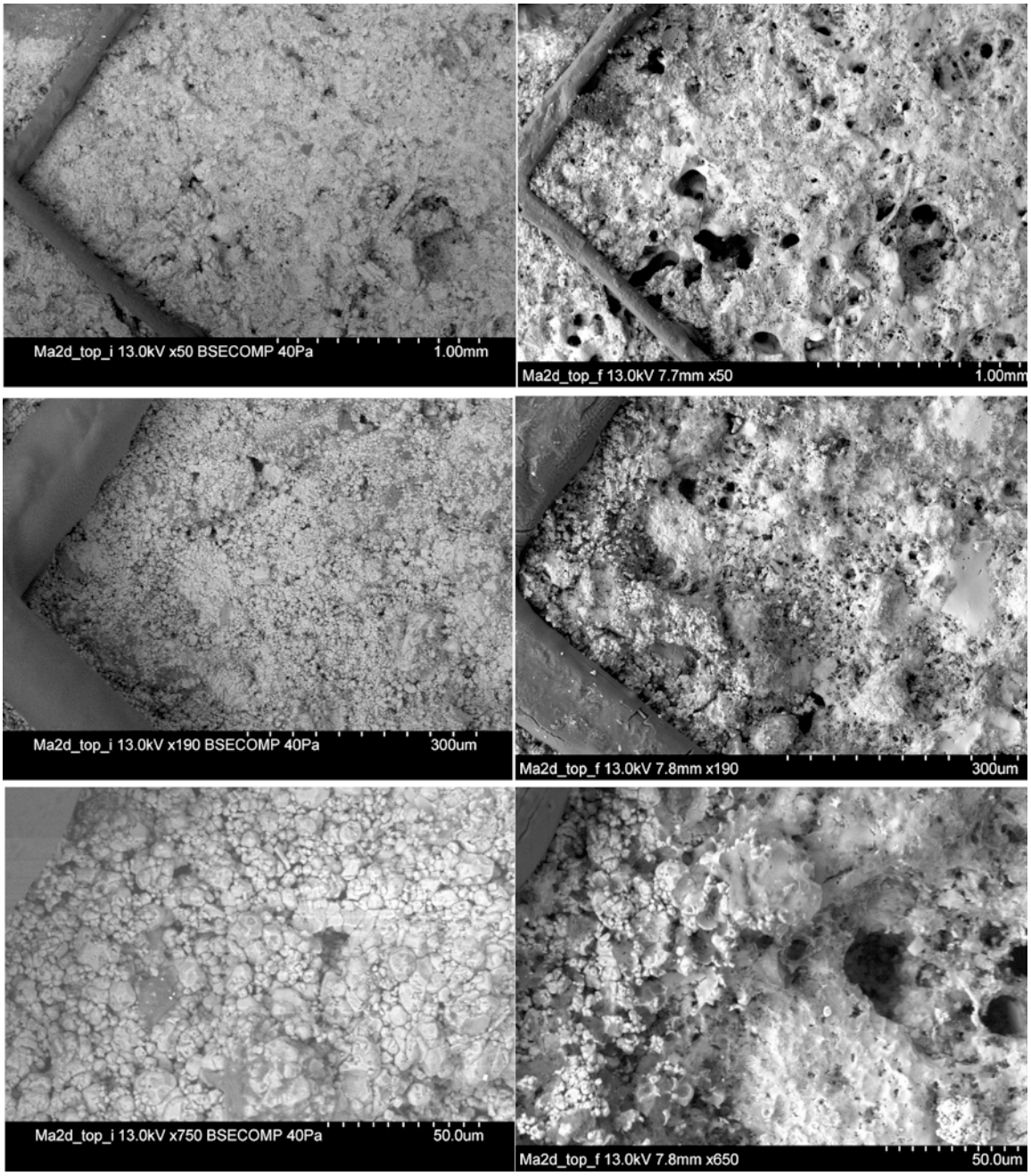

Figure 7a. Time-lapse SEM imaging of the MA2d sample showing the changes in microstructure (before-left panel and after- right panel) resulted from injecting CO_2-rich water. Images refer to the top of the samples (*i.e.,* injection point) and are taken at different optical magnification to gain insight into the scale at which changes occur.

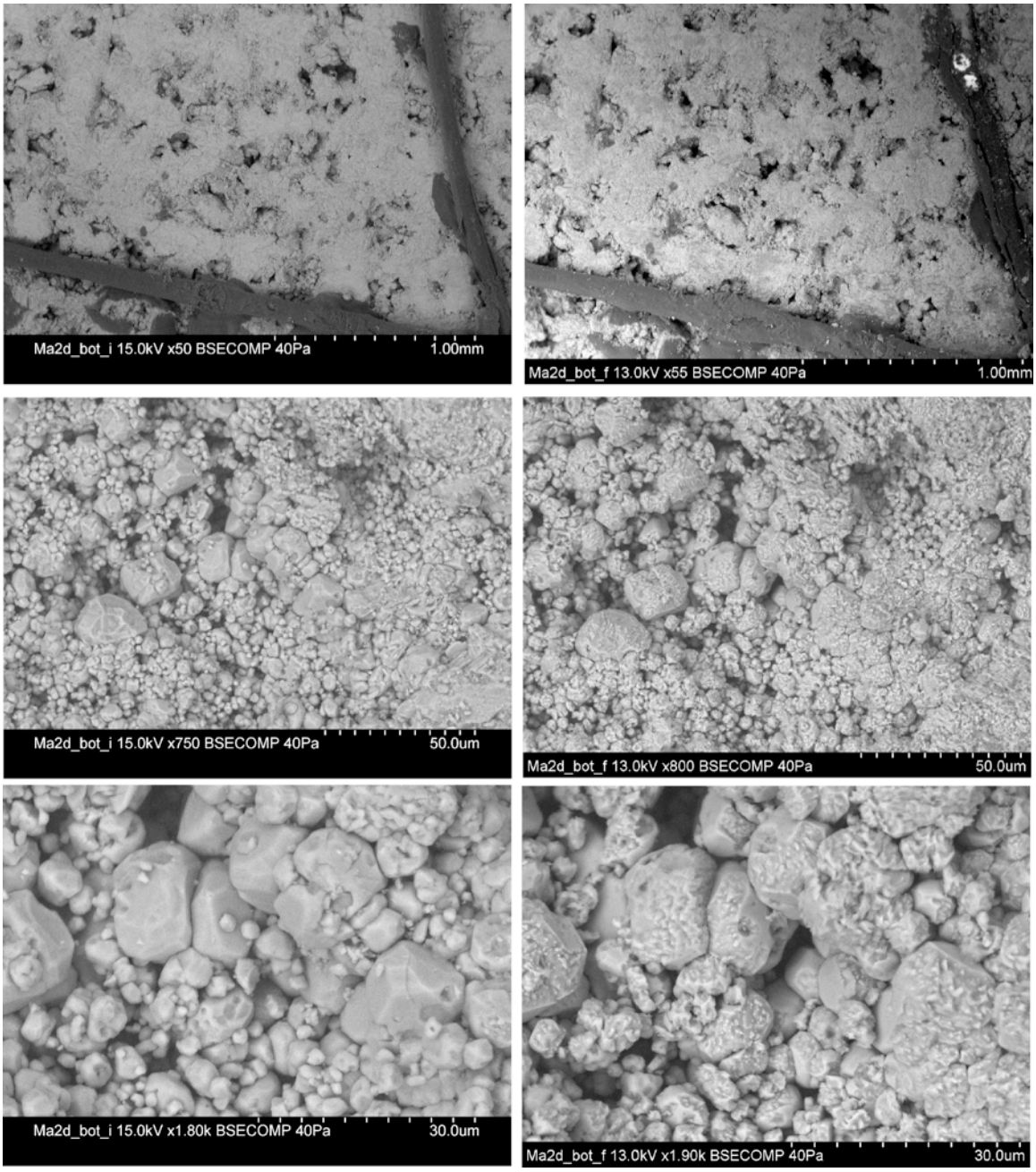

Figure 7b. Time-lapse SEM imaging of the MA2d sample showing the changes in microstructure (before-left panel and after- right panel) resulted from injecting CO_2-rich water. Images refer to the bottom of the samples (*i.e.,* depletion point) and are taken at different optical magnification to gain insight into the scale at which changes occur.

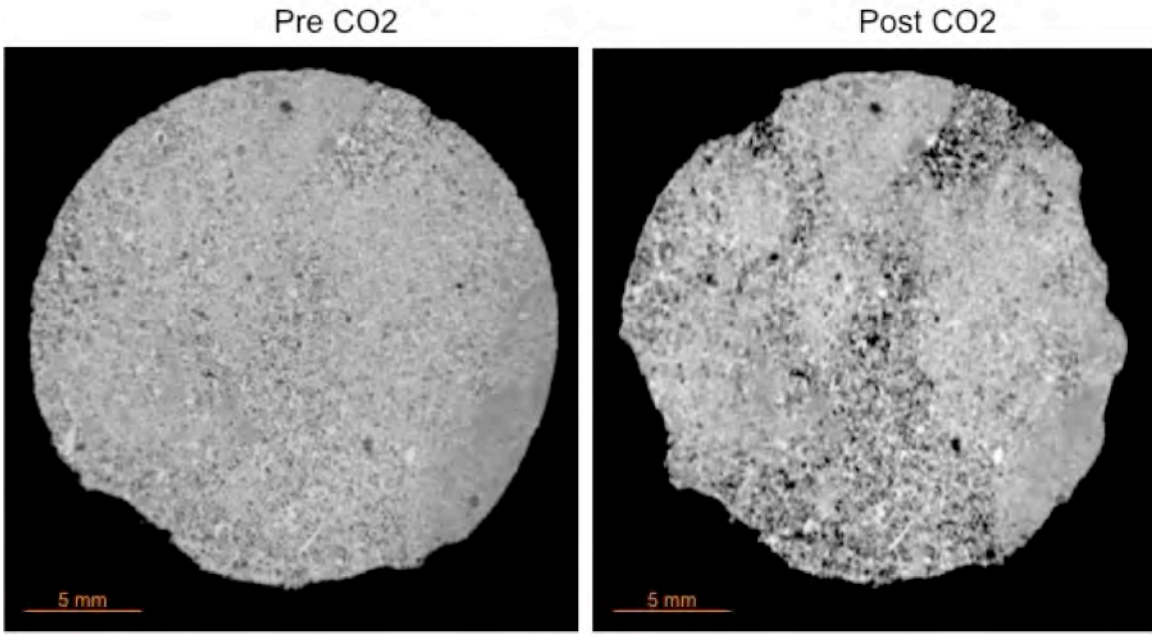

Figure 8. Time-lapse CT-scan images of the MA2d sample showing the changes in microstructure (before-left panel and after- right panel) resulting from the injection of CO_2-rich water. Images refer to one slice of the 3D volume.

The acoustic, hydraulic, and transport properties of the measured samples are reported in Tables 2-5 for various stages of the injection process. The first column in each table refers to the volume of injected pore fluid measured in pore volumes. Note that both dry and saturated rock properties were measured at various intervals during the injection process.

Specific observations are as follows:

1. For sample Ma2d (Table 2), the dry rock Vp and Vs decreased by 20% and 26%, respectively (at 1.1 MPa effective pressure). The saturated rock Vp and Vs decreased by 11% and 7%, respectively (at 0.6 MPa effective pressure). The porosity increased by .03 and the permeability increased by 615 mD.
2. For sample Ma3b (Table 3), the dry rock Vp and Vs decreased by 8% and 10%, respectively (at 8MPa effective pressure). The saturated rock Vp and Vs decreased by 8% and 7%, respectively (at 6 MPa effective pressure). The porosity increased by .05 and the permeability increased by 855 mD.

3. For sample RU_20_7855A (Table 4), the dry rock Vp and Vs decreased by 2% and 30%, respectively (at 1.1 MPa effective pressure). The saturated rock Vp and Vs decreased by 2% and 1%, respectively (at 0.7 MPa effective pressure). The porosity increased by 0.01 and the permeability increased by 4000 mD.
4. For sample RU_20_7855B (Table 5), the dry rock Vp and Vs decreased by 15% and 15%, respectively (at 1.1 MPa effective pressure). The saturated rock Vp and Vs decreased by 3% and 1%, respectively (at 0.6 MPa effective pressure). The porosity increased by 0.02 and the permeability increased by 4000 mD.
5. Figures 9 and 10 show respectively the variation of the P- and S-wave velocities of the rock frame upon injection. Velocity values are normalized with respect to their pre-injection values. Data refer to 3 carbonate samples, characterized by similar micrite content, that have been measured under different conditions of confining pressure. Figures 9 and 10 show that the variation of the velocity of the rock frame upon injection is lower with increasing pressure. Two competing and interdependent processes control the variation of velocity: the chemical dissolution of calcite and the resulting mechanical compaction under pressure.
6. Figure 11 shows the increase of both porosity and permeability of the rock with the proceeding of the injection. Data refer to 3 carbonate samples characterized by similar micrite content. Injections were performed under different conditions of confining pressure.

Table 2: Elastic and transport properties of carbonate sample Ma2d while injection of CO_2-rich brine. Vnorm is the number of pore volumes of pore fluid injected. Ca is the concentration of dissolved calcium in the expelled pore fluid. Vp, Vs are ultrasonic velocities. ρb is bulk density. Phi is porosity (%).

Sample ID: Ma2d												
	Pressures (Mpa)			Dry conditions			Saturated conditions					
Vnorm	Confining	Pore	Effective	Vp (m/s)	Vs (m/s)	ρb dry (gcm3)	Vp(m/s)	Vs (m/s)	ρb sat (g/cm3)	Ca (mg/L)	Phi corr	Permeability (mD)
0.0	0	0	0	2.960	1.739	1.896					29.80	135.70
0.0	1.1	0	1.1	3.014	1.905	1.902					29.06	
9.9	1.1	0.5	0.6				3.075	1.764	2.214	168.00	28.93	
57.6	1.1	0.5	0.6				3.033	1.792	2.212	168.00	29.01	
115.2	1.1	0.5	0.6				2.945	1.803	2.209	168.00	29.19	
115.2	1.1	0	1.1	2.571	1.440	1.893					29.07	
222.9	1.1	0.5	0.6				2.914	1.751	2.201	176.00	29.67	
338.1	1.1	0.5	0.6				2.899	1.754	2.191	168.00	30.23	
338.1	1.1	0	1.1	2.523	1.403	1.862					30.13	
445.8	1.1	0.5	0.6				2.831	1.679	2.184	148.00	30.66	
558.5	1.1	0.5	0.6				2.826	1.688	2.177	148.00	31.05	
558.5	1.1	0	1.1	2.490	1.394	1.838					30.99	
673.7	1.1	0.5	0.6				2.745	1.673	2.171	128.00	31.45	
771.3	1.1	0.5	0.6				2.737	1.663	2.165	136.00	31.	
771.3	1.1	0	1.1	2.40	1.397	1.817					31.	
												750.5

Table 3: Elastic and transport properties of carbonate sample Ma3b while injection of CO_2-rich brine. Vnorm is the number of pore volumes of pore fluid injected. Ca is the concentration of dissolved calcium in the expelled pore fluid. Vp, Vs are ultrasonic velocities. ρb is bulk density. Phi is porosity (%).

Sample ID: Ma3b												
	Pressures (Mpa)			Dry conditions			Saturated conditions					
Vnorm	Confining	Pore	Effective	Vp (m/s)	Vs (m/s)	ρb dry (gcm3)	Vp (m/s)	Vs (m/s)	ρb sat (g/cm3)	Ca (mg/L)	Phi corr	Permeability (mD)
0.0	0	0	0								26.24	136.00
0.0	0.1	0	0.1	3374	1663	2.52					26.19	
0.0	5	0	5	3462	1800	2.57					24.94	
0.0	7	0	7	3607	1856	2.57					24.74	
0.0	8	0	8	3727	1872	2.57					24.74	
33.0	8	2	6				3719	1936	2.27	208	24.80	
98.9	8	2	6				3705	1927	2.26	212	25.12	
98.9	8	0	8	3518	1781	2.56					25.07	
197.7	8	2	6				3694	1913	2.25	220	25.58	
283.7	8	2	6				3694	1904	2.25	208	26.01	
402.7	8	2	6				3674	1887	2.24	204	26.62	
402.7	8	0	8	3475	1757	2.52					26.57	
552.8	8	2	6				3592	1878	2.22	200	27.36	
701.1	8	2	6				3533	1868	2.21	192	28.10	
701.1	8	0	8	3441	1711	2.48					28.06	
895.2	8	2	6				3503	1848	2.19	196	29.07	
931.8	8	0	8	3434	1674	2.45					29.23	
1146.	8	2	6				3439	1809	2.17	176	30.30	
1332.	8	2	6			2.39	3427	1790	2.16	168	31.21	
												991

Table 4: Elastic and transport properties of carbonate sample RU_20_7855A while injection of CO_2-rich brine. Vnorm is the number of pore volumes of pore fluid injected. Ca is the concentration of dissolved calcium in the expelled pore fluid. Vp, Vs are ultrasonic velocities. ρb is bulk density. Phi is porosity (%).

Sample ID: RU_20_7855A

	Pressures (Mpa)			Dry conditions			Saturated conditions					
Vnorm	Confining	Pore	Effective	Vp (m/s)	Vs (m/s)	ρb dry (gcm3)	Vp(m/s)	Vs (m/s)	ρb sat (g/cm3)	Ca (mg/L)	Phi corr	Permeability (mD)
0	0	0	0	4.447	2.460	2.064					25.48	15.30
0	0	0	0	4.421	2.421	2.064					25.48	
0	1.1	0	1.1	4.570	2.409	2.075					24.34	
10	1.1	0.4	0.7				4.552	2.284	2.338	112	24.44	
50	1.1	0.4	0.7				4.530	2.282	2.338	84	24.40	
88	1.1	0.4	0.7				4.500	2.280	2.338	80	24.42	
88	1.1	0	1.1	4.470	2.111	2.073					24.20	
175	1.1	0.4	0.7				4.479	2.267	2.337	48	24.49	
250	1.1	0.4	0.7				4.465	2.264	2.334	48	24.62	
250	1.1	0	1.1	4.464	2.111	2.065					24.48	
400	1.1	0.4	0.7				4.470	2.262	2.329	40	24.92	
600	1.1	0.4	0.7				4.467	2.264	2.318	36	25.53	
600	1.1	0	1.1	4.468	-1.623	2.078					23.98	
												>4000

Table 5: Elastic and transport properties of carbonate sample RU_20_7855B while injection of CO_2-rich brine. Vnorm is the number of pore volumes of pore fluid injected. Ca is the concentration of dissolved calcium in the expelled pore fluid. Vp, Vs are ultrasonic velocities. ρb is bulk density. Phi is porosity (%).

Sample ID: RU_20_7855B												
	Pressures (Mpa)			Dry conditions			Saturated conditions					
Vnorm	Confining	Pore	Effective	Vp (m/s)	Vs (m/s)	ρb dry (gcm3)	Vp(m/s)	Vs (m/s)	ρb sat (g/cm3)	Ca (mg/L)	Phi corr	Permeability (mD)
0.0	0	0	0	4230	2393	2.03					26.31	10.30
0.0	1.1	0	1.1	4148	2248	2.04					26.07	
55.6	1.1	0.5	0.6				4152	2191	2.31	176.00	26.09	
99.5	1.1	0.5	0.6				4093	2191	2.31	128.00	26.13	
99.5	1.1	0	1.1	3706	1962	2.04					26.08	
204.9	1.1	0.5	0.6				4092	2190	2.31	116.00	26.19	
376.1	1.1	0.5	0.6				4092	2172	2.31	112.00	26.35	
376.1	1.1	0	1.1	3654	1936	2.03					26.33	
537.0	1.1	0.5	0.6				4092	2169	2.30	96.00	26.50	
699.5	1.1	0.5	0.6				4073	2169	2.30	104.00	26.66	
699.5	1.1	0	1.1	3614	1930	2.02					26.64	
1401.9	1.1	0.5	0.6				4060	2169	2.29	56.00	27.33	
1401.9	1.1	0	1.1	3555	1907	1.99					27.30	
2077.9	1.1	0.5	0.6				4022	2168	2.28	72.00	27.92	
2077.9	1.1	0	1.1	3521	1908	1.97					27.92	
												>4000

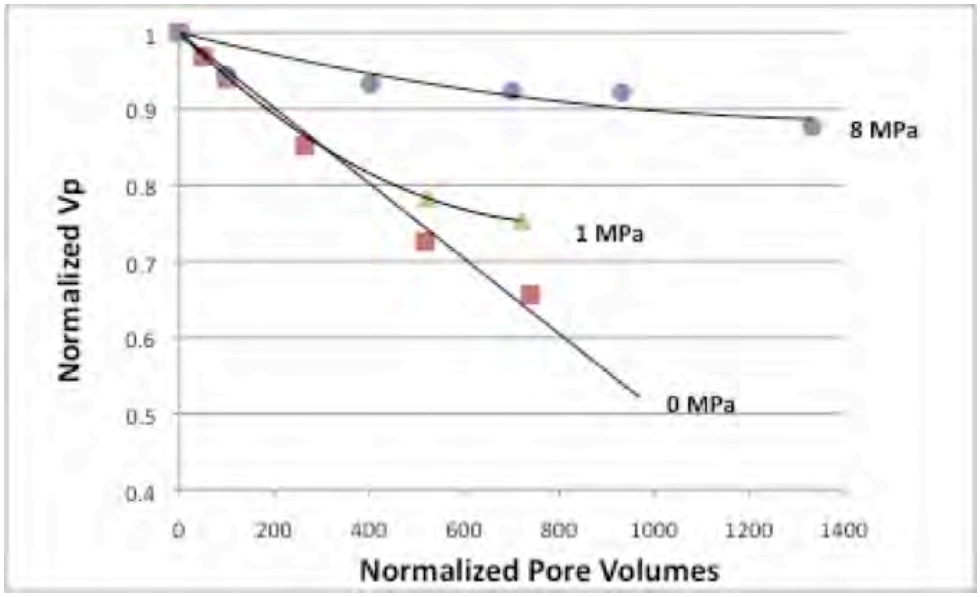

Figure 9: Variation of the P- wave velocity of the rock frame upon injection. Velocity values are normalized with the respect to their pre-injection values. Data are color-coded as a function of the confining pressure.

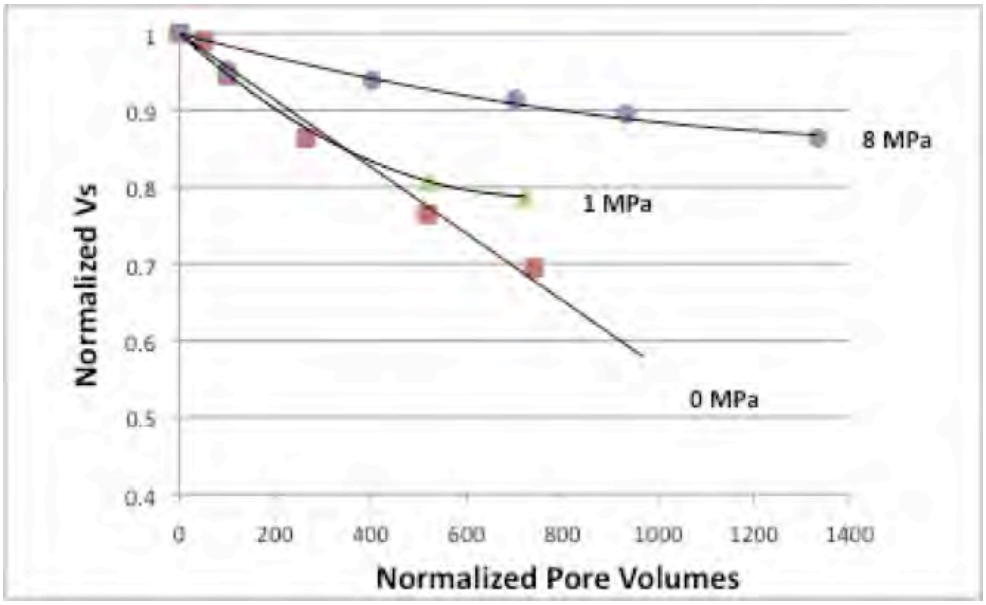

Figure 10: Variation of the S- wave velocity of the rock frame upon injection. Velocity values are normalized with the respect to their pre-injection values. Data are color-coded as a function of the confining pressure.

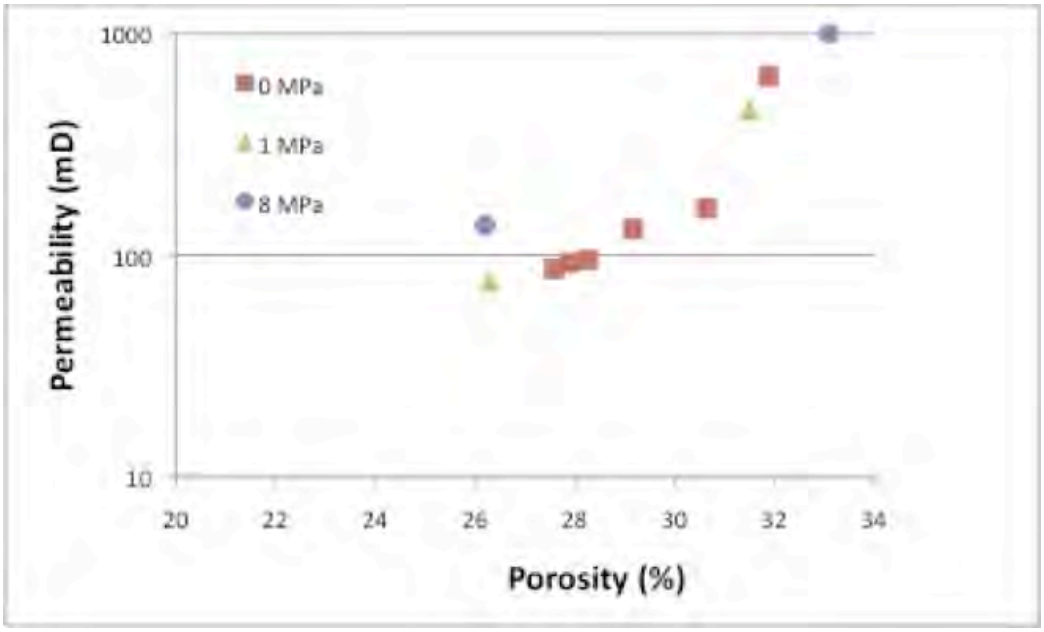

Figure 11: Increase of permeability and porosity of the rock upon injection. Data refer to 3 carbonate samples characterized by similar micrite content. Injections were performed under different conditions of confining pressure.

Observations on Sandstones

A substantial amount of prior work as been reported from Detailed Area Study in the Tuscaloosa formation at Cranfield, Mississipppi, For example, Hovorka (2009) reported that in the sandstone interval, dissolved CO_2 lowered the pH of the brine, dissolving calcite from the matrix and large amounts of iron (Fe) and manganese (Mn). Furthermore, laboratory investigation of CO_2-brine-rock interaction within samples from the Tuscaloosa sandstone formation reported a rapid increase of dissolved iron immediately after injection, caused by the dissolution of iron-bearing carbonate minerals and iron-chlorite (Karamalidis et al., 2010).

In the present project, rock physics experiments were performed to study the effects on the elastic properties due to physical (*i.e.,* pressure) and chemical processes occurring upon injection of carbon dioxide into samples of the Lower Tuscaloosa formation. Rock samples ranged from clean quartz-rich sandstone to sandstone containing iron-rich chlorite (chamosite) and calcite.

At the Cranfield Detailed Area Study, the in-situ brine of the Tuscaloosa formation is Na-Ca-Cl type with about 152,000 milligrams per liter of total dissolved solids (Karamalidis et al., 2010). According to La Chatelier's principle, the presence of high calcium content in the brine may inhibit dissolution of calcite. The pH values of the synthetic Tuscaloosa brine and the CO_2 rich Tuscaloosa brine were 5.8 and 3.4 respectively. The temperature and pressure of the formation also control the chemical reactions.

Confining pressure plays an important role in simulating the chemical reactions. We used a pressure column approach to resolve the confining stress. According to well logs, the average density is roughly 2.1 grams per cubic centimeter (g/cc). The formation under consideration is roughly 3.2 kilometers (km) deep. Therefore, the confining stress is roughly 65 MPa. The pore pressure before injection is approximately 31 MPa; the pore pressure after injection is approximately 38 MPa (Hovorka et al. 2009). However, due to the limitations of the pressure vessel used, both confining and pore pressures are scaled back by 10 MPa in order to maintain in-situ differential pressure. Therefore, the confining pressure, initial pore pressure, and final pore pressure are 55 MPa, 21 MPa, and 28 MPa respectively. Note that the experiments are performed at room temperature in order to hold one variable constant. The characterization of the samples included Helium

porosity, Klinkenberg-corrected nitrogen permeability, and ultrasonic P- and S-wave velocities. The plugs were jacketed with rubber tubing to isolate them from the confining pressure medium. PZT-crystals mounted on steel endplates generated P- and S-waves (1 MHz for P-waves and 0.7 MHz for S-waves). Three linear potentiometers were used to measure length changes of the samples as a function of stress. The length changes were related to changes in porosity by assuming that pore contraction was the main cause of strain. The accuracy in velocity measurements was estimated to be about ±1%. Compressional and shear wave velocities are measured at various confining pressures after multiple injections of carbon dioxide rich brine. The velocities are measured when the sample is dry to minimize dispersion. Measurements of a dry sample also show how the frame changes with each injection.

The first step in the experimental study of the sandstones was to prepare the samples and record a baseline of the mechanical properties. Since the samples contain some clay, the core plugs were dried at 70ºC for 72 hours. The initial geometry and mass of the core plug were recorded to note any change in bulk properties after carbonic acid injection.

After measuring porosity and permeability, the samples were inserted into the pressure vessel where they undergo a series of loadings, reactant injections, and unloadings. Measuring the pressure dependency of P- and S- wave velocities for the dry core plug, before any injection, establishes a baseline for the elastic properties of the rock. Both the compressional and shear velocities of the core plug were measured as a function of confining pressure, in this case ranging from 0 to 55 MPa. Smaller pressure intervals were used at low confining pressures to map the nonlinear portion of the compaction curve.

Measuring velocity at various differential pressures after injection may simulate changing the pore pressure. Knowing the impact of pore pressure on the elastic properties of the core plug can enable one to resolve the change in velocity due to the chemical reaction and the change in velocity due to the change in pore pressure. However, loading and unloading a core plug in this manner may permanently deform the microstructure of the sample. In order to understand if the sample was experiencing any damage revealed by hysteresis, we performed an experimental test in which we loaded and unloaded a “twin” sample with the same stress path. The “twin” core plug comes from the depth as the injected sample and has the same porosity and permeability. SEM images of the top

of the samples (i.e., injection side) were taken before and after the injection experiments to monitor changes in the rock's microstructure. The fluid was regularly sampled at the outlet to measure pH and iron content using the titration method. We used a digital titrator (HACH LANGE 16900) and a commercial TitraVer 0.0716 M solution as titrant.

Four samples, A, E, X, and Y from the Lower Tuscaloosa sandstones of Cranfield, Mississippi were subject to injection of CO_2-rich brine. The in-situ brine of the Tuscaloosa formation was used, which is Na-Ca-Cl type with about 150 parts per million of total dissolved solids (Joy et al., 2011). The measurements on these samples were conducted prior to the injection and also after the injection of about 150 pore volumes of the brine. All samples were dried by injecting dry warm air and He gas after the injection, and their elastic-wave velocities and porosities were measured at varying confining pressure. In addition to these four samples, the porosity and velocity were measured on a reference sample B which was not subjected to brine injection. Figure 12 displays velocity-porosity plots for these samples, where both the velocity and porosity were registered as a function of the hydrostatic confining stress. The velocity-pressure behavior for these samples is shown in Figure 13.

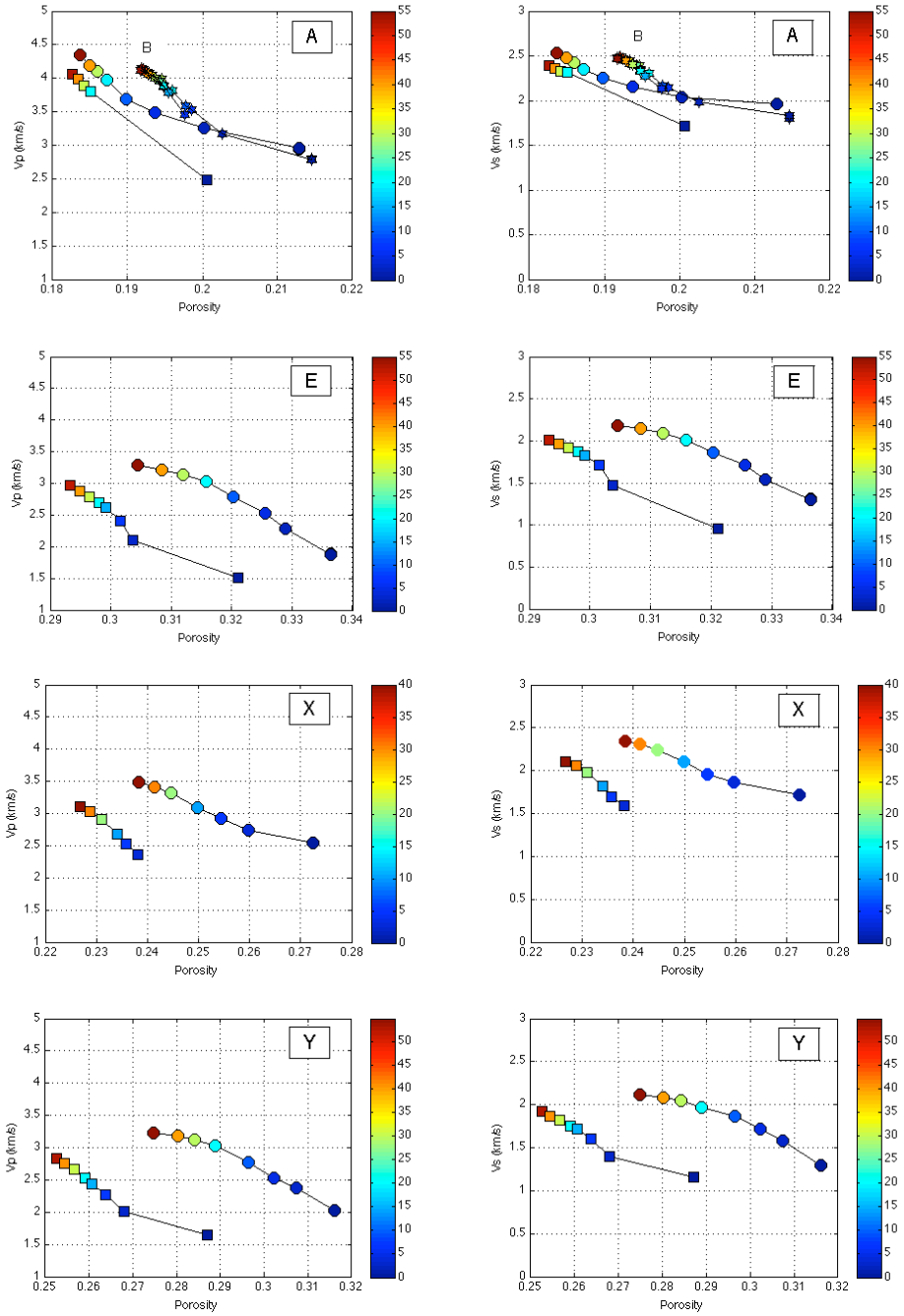

Figure 12. Velocity versus porosity for the samples under examination (from top to bottom, A and B, E, X, and Y) color-coded by the confining stress. Circles are for the pre-injection samples, while squares are for the same samples after the injection.

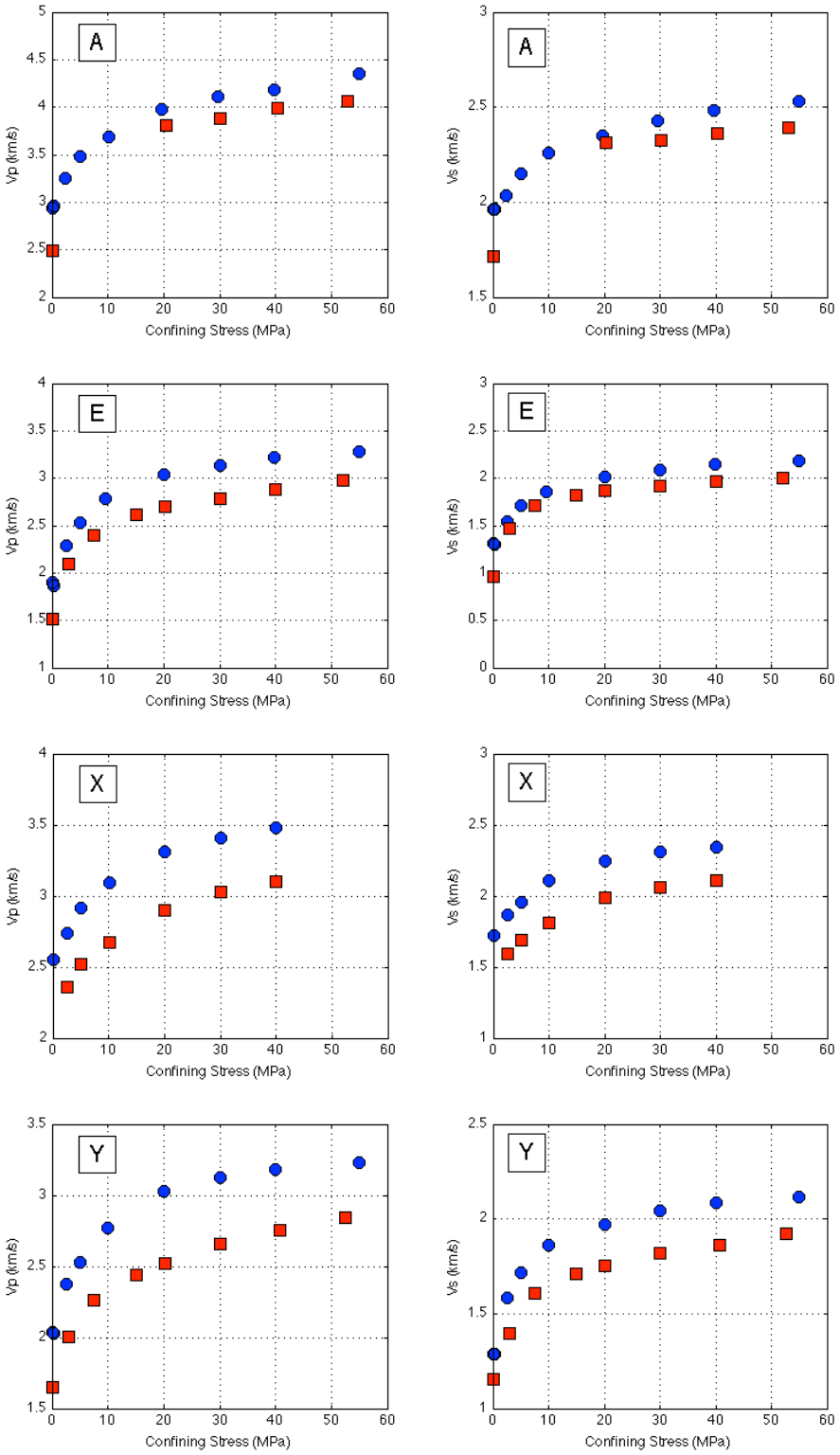

Figure 13. Velocity versus confining stress for samples A, E, X, and Y (top to bottom). The blue circles are for the pre-injection samples, while red squares are for the same samples after the injection.

Figure 14 shows the time-lapse SEM images monitoring the permanent changes induced in the sandstone microstructure by chamosite dissolution upon injection of CO_2-rich brine. After injection, the sandstone shows an overall *cleaner* microstructure. Two main changes are involved: (a) clay dissolution between grains and at the grain contact and (b) rearrangement of grains due to compaction under pressure.

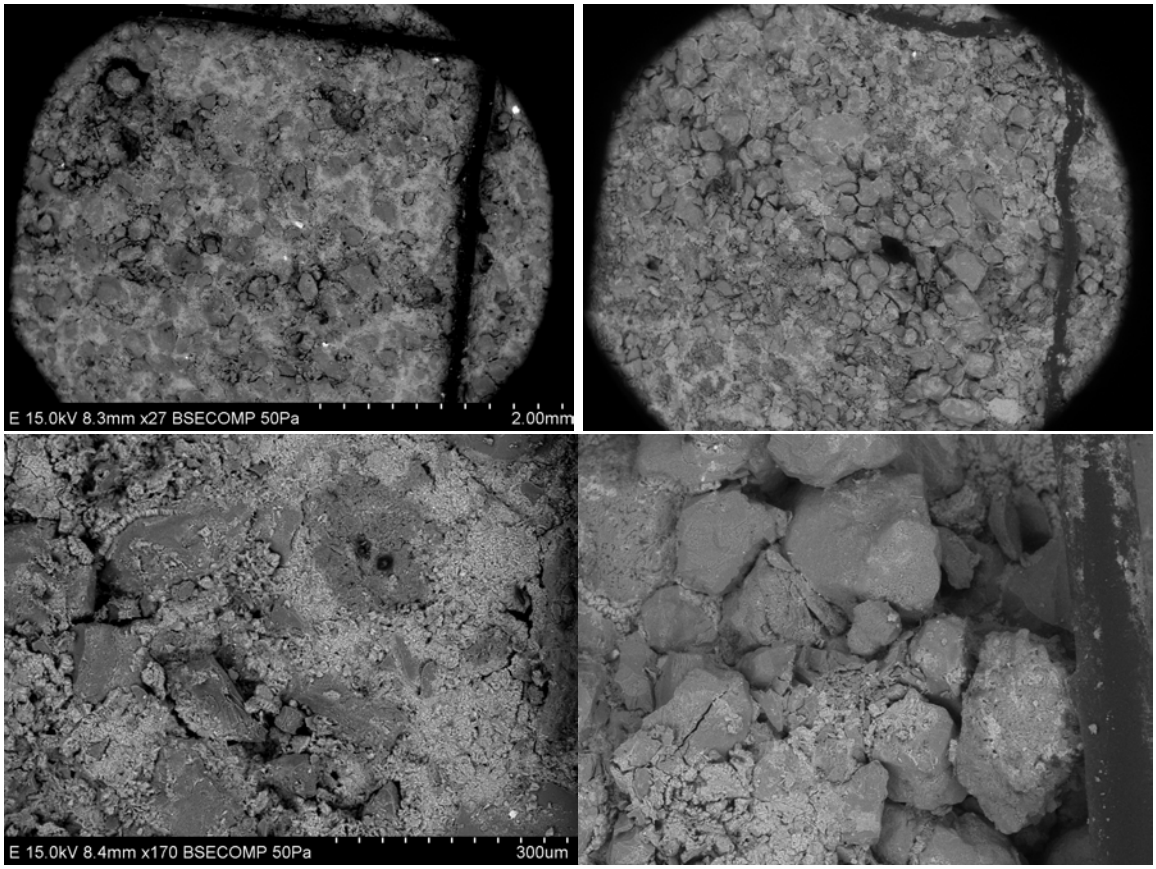

Figure 14. Time-lapse SEM images monitoring the permanent changes induced in the sandstone (sample E) microstructure by chamosite dissolution upon injection of CO_2-rich brine. Two main changes are involved: (a) clay dissolution between grains and at the grain contact and (b) rearrangement of grains due to compaction under pressure.

STUDY OF MICROSTRUCTURE HETEROGENEITY USING MERCURY INJECTION

[*key publication: Vialle et al., 2013*]

We continued our study of heterogeneities of microstructure in several rock types, with the aim to better understand the distributions of flow paths and pore surface area that are important for movement and chemical reactivity of CO_2 in the subsurface.

Four core plugs were selected for this study: two Fontainebleau sandstone samples, *Sand-A* and *Sand-B*, and two carbonate samples, *Carb-A* and *Carb-B*. The core plugs are cylindrical, 1" in diameter and about 1" in length. *Sand-A* and *Sand-B* are very clean sandstones, with fairly homogeneous pore space and predominantly quartz mineralogy (mono-mineralic composition of quartz). The two carbonates come from the Upper Cretaceous carbonate system of the Gargano-Murge region, which belongs to the stable foreland of Southern Italy. *Carb-A* is a wackestone to packstone from the Peschici formation dated Paleocene-Eocene and *Carb-B* is a micritic mudstone from the Monte Acuto formation, dated Late Cretaceous (Martinis and Pavan, 1967; Cremonini et al., 1971). Both carbonates are composed of calcite at nearly 100%.

Results related to CO_2 -injection tests in carbonates discussed in the previous section were obtained on samples from the same formations, showing similar microstructure. Sample G has a microstructure similar to *Carb-A;* all the other carbonates had a similar microstructure as *Carb-B*, but with variable amount of micrite.

The first step was to characterize the whole core plugs: He-porosity and Klinkenberg-corrected air permeability were measured at bench-top conditions. Acoustic P- and S-wave velocities, at 1MHz and 0.7 MHz respectively, were acquired on dry samples under increasing (up to 30MPa) and decreasing hydrostatic effective stress conditions. The results are reported in Tables 6 and 7, and Figures 15-18. Both sandstone and carbonate samples show a strong variation of permeability with porosity. In both rock types, a factor of ~2 increase in porosity was associated with a factor of >15 increase in permeability.

Measured grain densities are, within the experimental error, consistent with the mono-mineralitic composition of the samples, *i.e.* quartz for *Sand-A* and *Sand-B* and calcite for *Carb-A* and *Carb-B*.

Measured P- and S-wave velocities as a function of pressure show that the pressure-dependence varies among the samples. For samples *Sand-A* and *Sand-B*, an increase of confining pressure from 0 to 30MPa causes P-wave velocity values to increase by 52% and 19%, respectively. The measured values at 30 MPa are consistent with the values previously reported in literature. Sample *Carb-A* shows little pressure dependence in the velocities (P-wave velocities increase by 4%) whereas sample *Carb-B* shows a strong pressure dependence (P-wave velocities increase by 28%). This result is consistent with previous measurements performed on samples belonging to the same formations as *Carb-A* and *Carb-B*. Pressure sensitivity of elastic properties is an indicator of microcracks and compliant grain boundaries.

Table 6. Measurements at benchtop conditions, for all four studied samples: porosity, bulk and grain densities (in g/cm^3) and permeability (in mD). Permeability of plug Carb-A is below the sensitivity level of the apparatus used (4 mD).

Sample	Porosity	Bulk Density (g/cm^3)	Grain Density (g/cm^3)	Permeability (mD)
Sand-A	0.097 ±0.001	2.39 ±0.01	2.65 ±0.01	35 ±3
Sand-B	0.153 ±0.002	2.23 ±0.01	2.63 ±0.01	540 ±20
Carb-A	0.167 ±0.002	2.24 ±0.01	2.69 ±0.01	<4
Carb-B	0.294 ±0.003	1.90 ±0.01	2.70 ±0.01	60 ±5

Table 7. Pressure dependence of the elastic-wave velocities for all four studied samples. Pressure is in MPa and P- and S-wave velocity in km/s.

Pressure	Sand A		Sand B		Carb A		Carb B	
	Vp	Vs	Vp	Vs	Vp	Vs	Vp	Vs
0	3.280	2.131	3.943	2.709	5.007	2.835	2.769	1.754
2.5	3.934	2.607	4.302	2.937	5.045	2.838	3.295	2.032
7.5	4.353	2.841	4.516	2.990	5.091	2.835	3.477	2.191
10	4.399	2.932	4.558	3.066	5.100	2.834	3.504	2.226
20	4.804	3.085	4.637	3.132	5.116	2.822	3.551	2.295
30	4.958	3.237	4.696	3.166	5.113	2.821	3.553	2.290
25	4.942	3.211	4.682	3.187	5.114	2.821	3.548	2.284
15	4.780	3.065	4.630	3.133	5.085	2.822	3.527	2.268
5	4.353	2.819	4.480	3.002	5.048	2.840	3.384	2.195
0	3.355	2.280	4.051	2.797	5.033	2.842	2.792	1.785

Figures 15 and 16 show plots of porosity vs. permeability on the core plug scale, superimposed with previously published trends from these rock types. Fontainbleau sandstone (Figure 15) shows an unusually good correlation between porosity and permeability, which is appears to be the result of homogenous pore space and systematic decrease of pore volume with diagenesis. The carbonate samples (Figure 16) show reasonably good correlation of porosity and permeability at larger pore volumes. However, there is tremendous variability of permeability in the lower pore-volume rocks, associated with the variation of micritic grains.

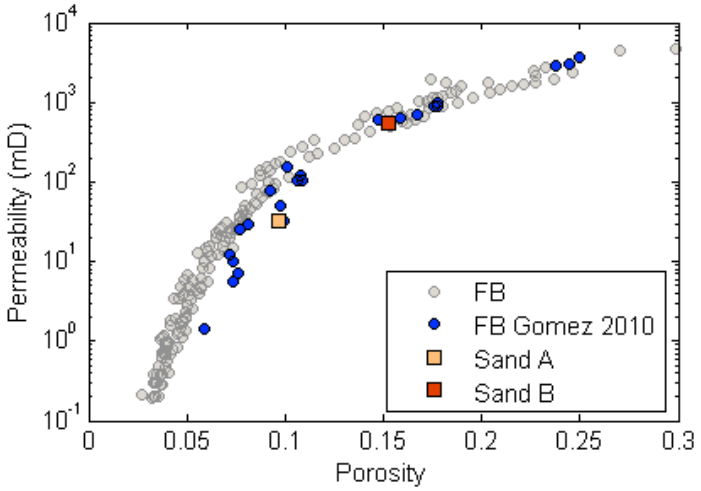

Figure 15. Permeability versus porosity for the two Fontainebleau plugs under examination, Sand A (orange symbol) and Sand B (red symbol). These data are compared to the Gomez et al. (2010) data (blue symbols) and the Bourbié and Zinszner (1985) data (gray dots).

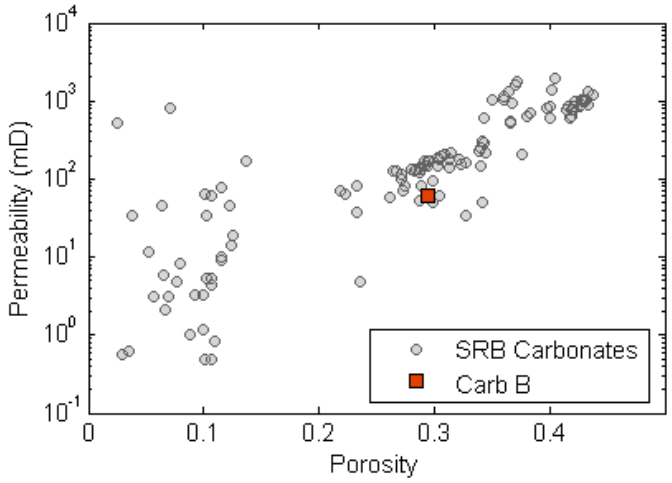

Figure 16. Permeability versus porosity for the carbonate data set (Scotellaro et al., 2008) to which our two carbonate plugs belong (gray dots) and for plug Carb B (red symbol). Permeability of plug Carb A is below the sensitivity level of the apparatus used and, hence, is not plotted.

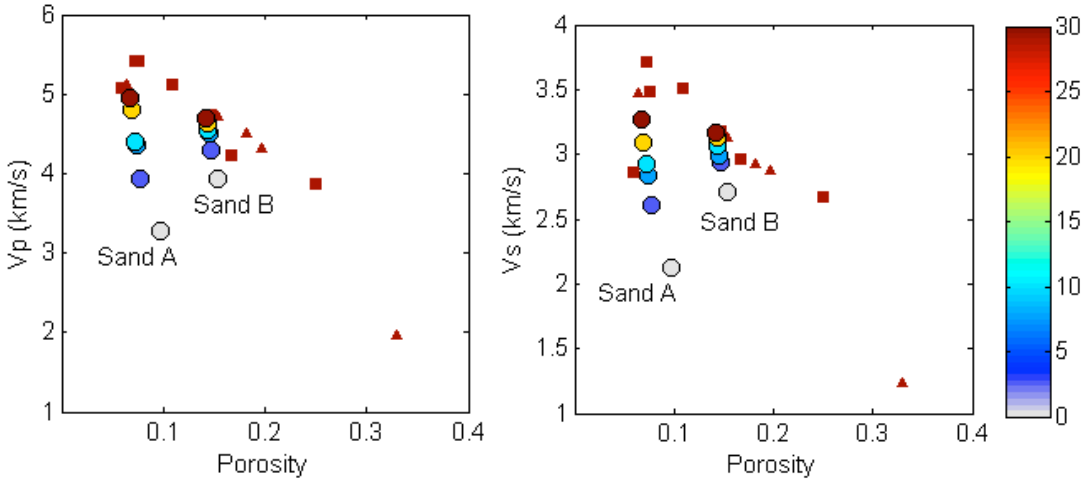

Figure 17. Pressure dependence of dry P- (left panel) and S- (right panel) wave velocity for the two Fontainebleau plugs under examination, Sand A and Sand B. Velocity data are color coded as a function of applied confining pressure (in MPa) under hydrostatic stress conditions. Are also plotted for reference Fontainebleau data from Gomez et al. (2010) (triangles) and Han (1986) (squares), both at 30 MPa.

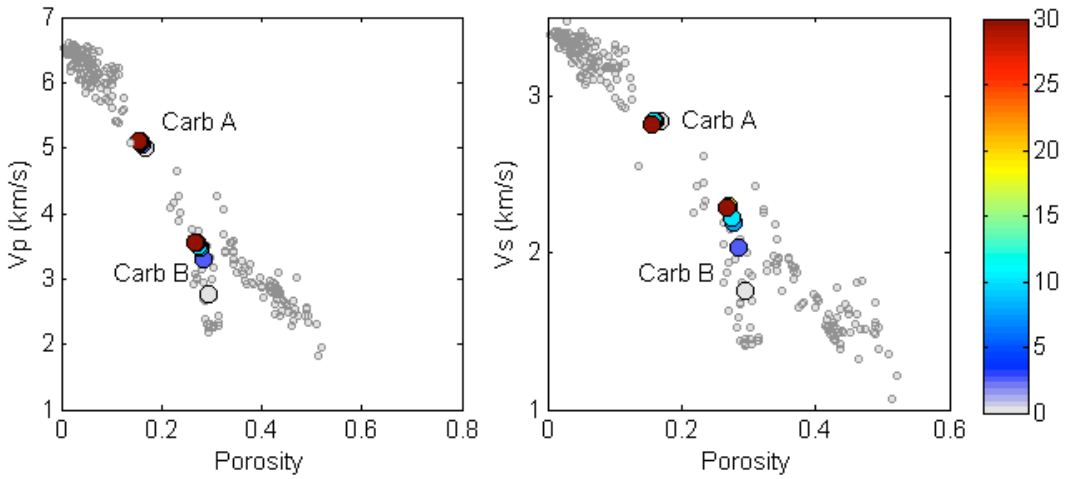

Figure 18. Pressure dependence of dry P- (left panel) and S- (right panel) wave velocities for the two studied carbonate plugs, Carb A and Carb B. Velocity data are color coded as a function of applied confining pressure (in MPa) under hydrostatic stress conditions. Are also plotted benchtop velocity data of the carbonate data set (Scotellaro et al., 2008) to which our two carbonate plugs belong (gray dots).

The new mercury intrusion studies look at the variation of properties within the plugs. To do this we extracted 8 subsamples for each of the four 1" rock plugs. These subsamples are also cylindrical, about 0.9 mm in diameter and 0.5 mm in length. After

coring and sawing, the subsamples were eventually polished with sandpaper or diamond smoothing discs to remove scratches, to ensure smooth and flat surfaces, and to make their faces parallel at ±0.1mm. For each core plus, four of the subsamples were used for MIP analysis (which destroys the samples), and the other four are reserved for investigation of matrix alteration due to reactive transport.

Prior to MIP (mercury injection porosimetry), porosity values were obtained for each of the subsamples, by using grain density from He-pycnometry, as well as mass and volume measured with high precision balance and caliper, respectively.

SEM images of the surface of the subsamples have also been taken to supplement the measurements, and some of them are given in Figures 21 to 23.

The mercury capillary measurements were carried out on the subsamples with an automated mercury porosimeter (AutoPore IV 9500 from Micromeritics) having both low-pressure and high-pressure analysis ports, allowing the development of intrusion pressures between 0.22 psi and 33000 psi. We used the Washburn equation to relate the applied pressures to the corresponding pore entry sizes:

$$P = -4\gamma \frac{\cos\theta}{d} \tag{5}$$

In this formula, P stands for the applied pressure in psi, γ for the surface tension of mercury in dynes/cm, θ for the contact angle, and d is the pore access diameter in μm. With a contact angle of 140° and a surface tension of 485 dynes/cm, pore entry diameters between about 980 μm and about 0.0065 μm can be measured.

During a mercury test, cumulative volumes of mercury intruded into the sample pore space were recorded for each applied pressure. A closure correction was applied to the generated data. This correction consists in subtracting all mercury intrusion volumes recorded up to the entry pressure; these data correspond to the easy invasion of mercury into the supercapillary pores (megapores) at the outer surface of the permeable rock sample under very low pressures. These megapores are considered to be surface features that are not representative of the internal microstructure.

The measured capillary curves are reported Figure 20 for all four subsamples of each rock type. The volume of intruded mercury (in mL) has been normalized to its final value (which is the pore volume of the sample measured by mercury tests) to give the mercury

saturation and is plotted as a function of increasing applied pressure. In Figure 20, the mercury volume has been normalized to the subsample volume, which gives the cumulative *porosity* of the subsample, as a function of intrusion pressure.

For each of the four rock types, the observed capillary curves show little variation among the subsamples, but large variations from one rock type to the next. The similarity of curves suggests that at the scale of the subsamples (about 0.5 cm^3), the two Fontainebleau samples *Sand-A* and *Sand-B* and the micritic mudstone *Carb-B* are homogeneous. For the limestone *Carb-A* however, although total porosity is nearly the same for all four subsamples, the relative distribution of the different pore sizes differ among the subsamples, since the four curves Figure 5 do not overlay for pressures ranging from 10 to 1000 psi (or about 10 and 0.1 um pore diameter).

The four curves relating to sample *Carb-A* indicating a broader distribution of pore diameters than the other three samples, spanning between 10 and 10000 psi (or about 10 and 0.01 um pore diameter) (Figure 19).

The capillary curves of samples *Sand-A* and *Sand-B* are typical of the monomodal pore size distribution of Fontainebleau sandstone, with a sudden and sharp increase in the cumulative volume of intruded mercury. This increase happens for higher pressure values (smaller pore throat size) for the sample having a lower total porosity. For the carbonate samples the increase in the volume of mercury intruded into the sample is more gradual, reflecting the complexity of the porous system in carbonates.

In Figure 20 we can notice that the variations in the final porosity values among the 4 subsamples of each rock type are smaller for samples having low total porosity values. The standard deviation in the porosity values is 0.002, 0.006, 0.002 and 0.009 for samples *Sand-A*, *Sand-B*, *Carb-A* and *Carb-B*, respectively.

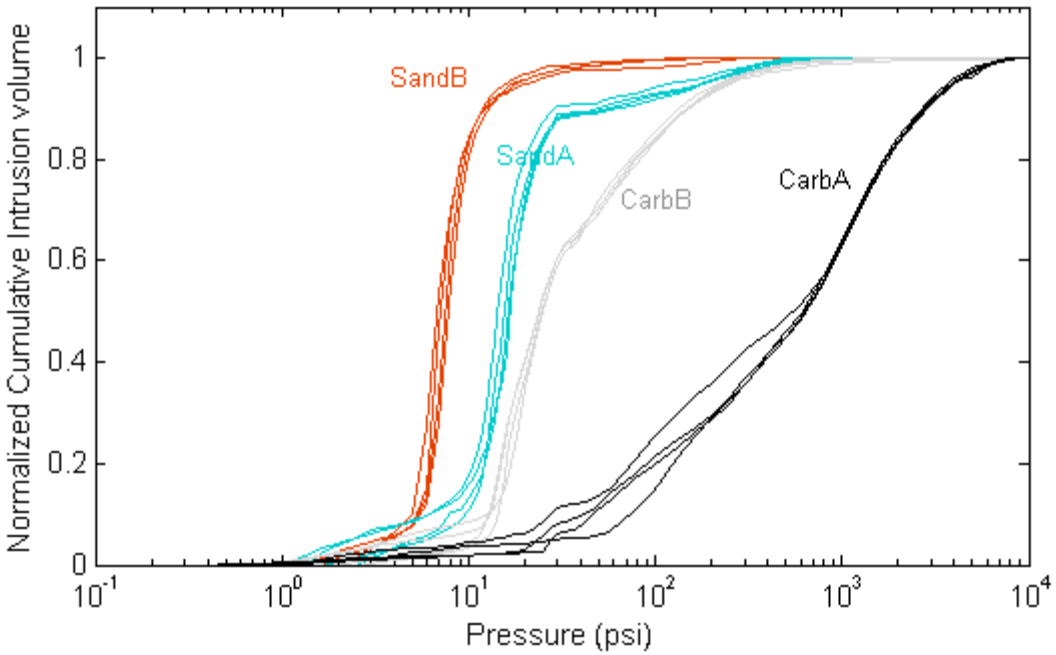

Figure 19: Capillary curves for all studied samples. The saturation of mercury (volume of mercury intruded normalized to its final value) is plotted as a function of increasing applied pressure.

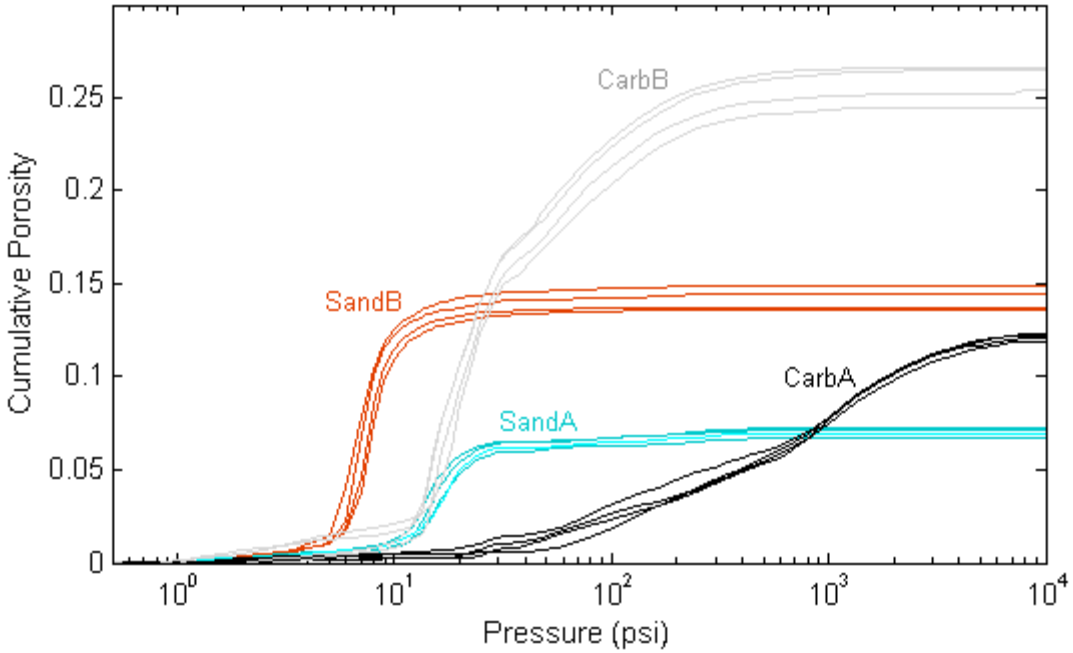

Figure 20: Capillary curves for all studied samples. The cumulative volume of mercury intruded into the sample has been normalized to the sample volume, giving the cumulative porosity of the sample as a function of applied pressure.

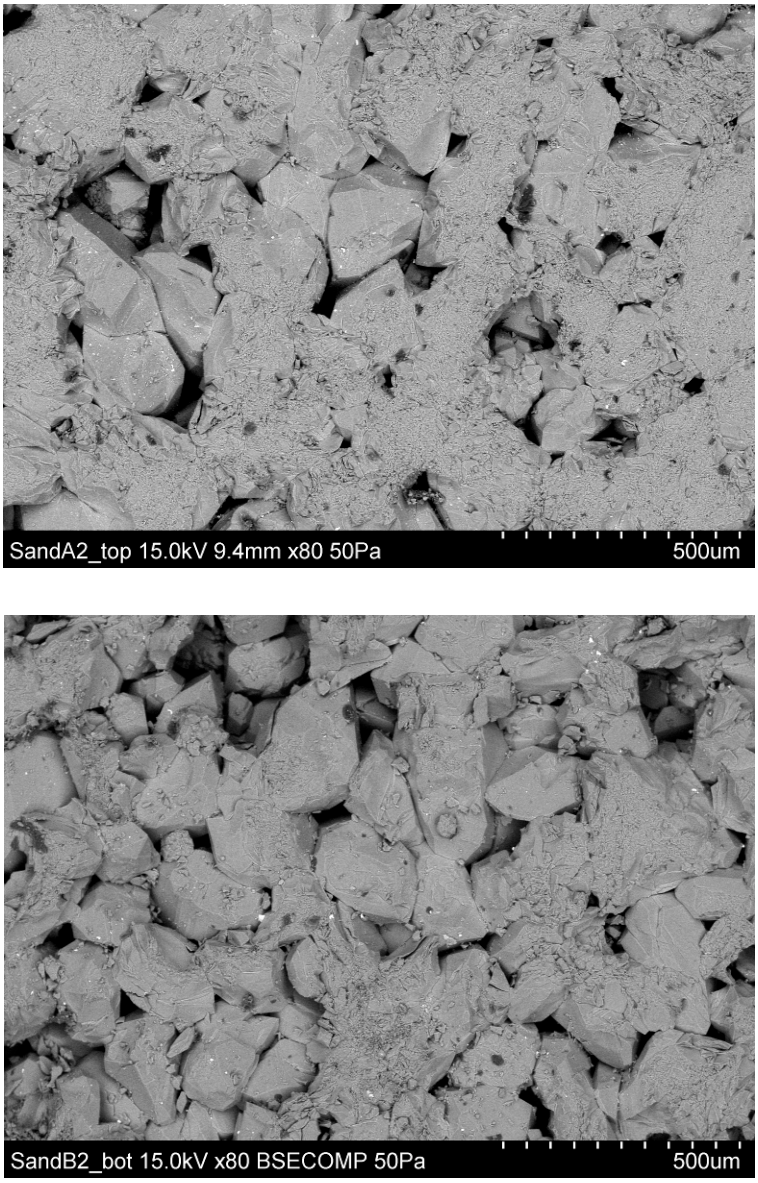

Figure 21: SEM images of a subsample of sample Sand-A (top) and a subsample of Sand-B (bottom).

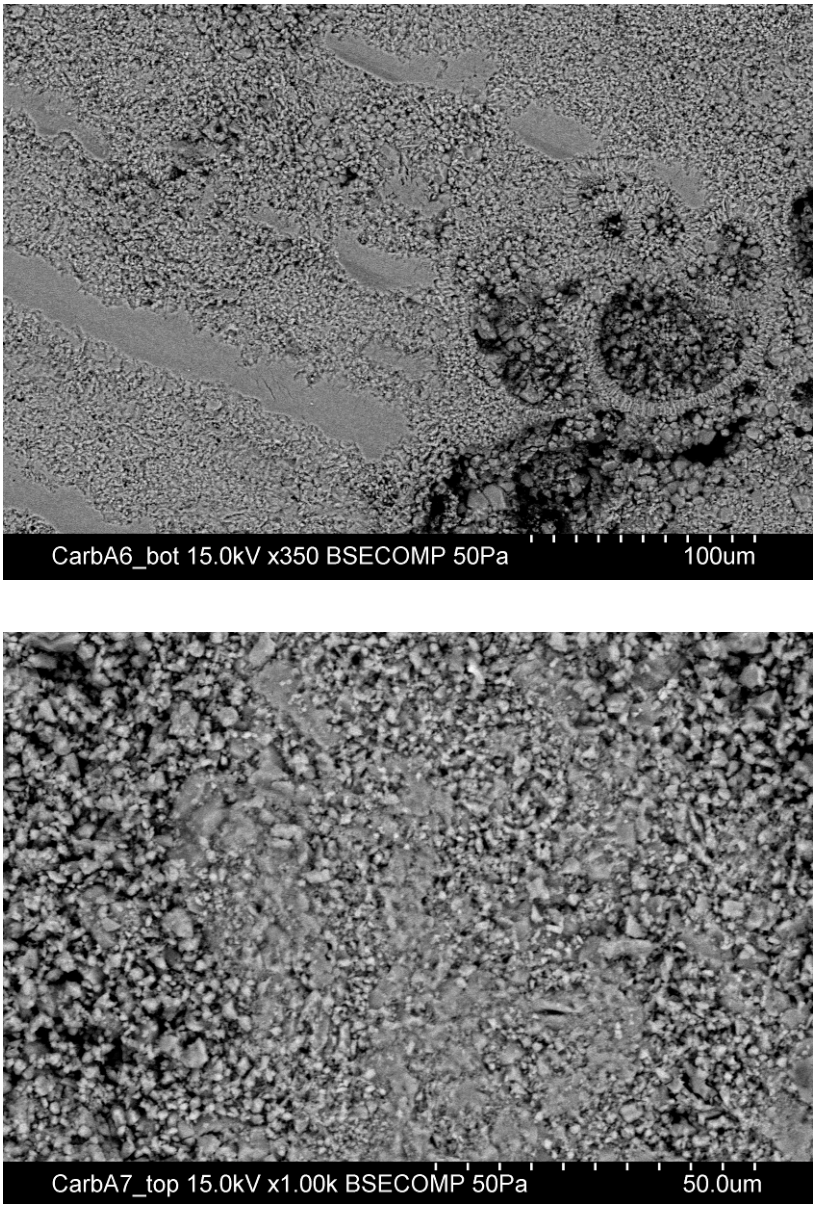

Figure 22: SEM images of two subsamples of sample Carb-A, taken at two different magnifications. The lower magnification (top panel) shows that the microstructure is composed of macropores and a tight microstructure around. A planktic foraminifera is visible on the right side. The higher magnification (bottom panel) shows that the microstruture goes from microporous anhedral micrite to compact anhedral micrite to coalescent micrite. Micritic grains are typically less than 1 μm.

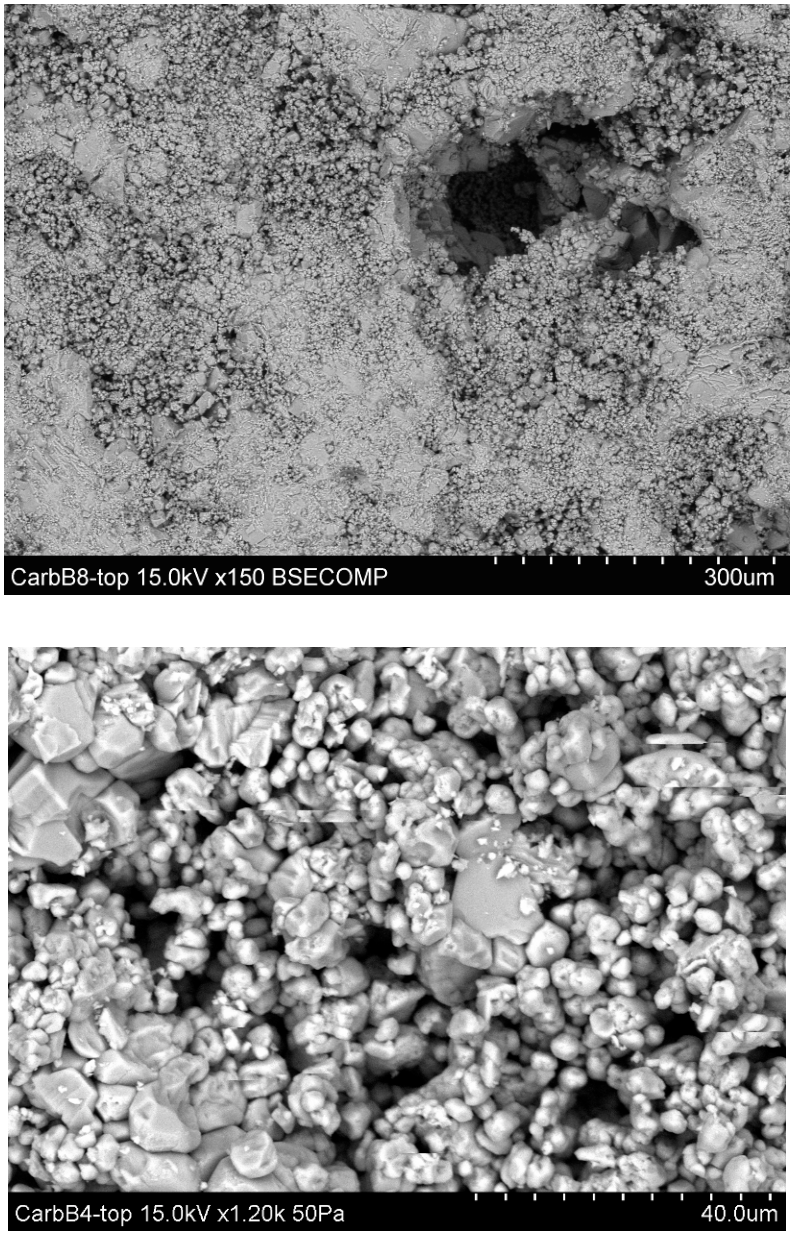

Figure 23: SEM images of two subsamples of sample Carb-B, taken at two different magnifications. The lower magnification (top panel) shows that the microstructure is composed of macropores, a microporous matrix (micrite) and a spar calcite cement (lighter zones). The higher magnifications shows that the matrix is a microporous rounded micrite; contacts between crystals are point contact to serrate contact. Crystals, typically 2 to 4 μm in diameter, are generally subhedral, sometimes anhedral, but all present rounded edges. Numerous pores, up to 10 μm ,can be observed in this microporous matrix. Micritic grains are surrounded by bigger spar crystals.

We considered several published methods relating permeability to various parameters inferred from mercury capillary pressures. The Winland equation (Kolodzie, 1980), the threshold pressure (Katz and Thompson, 1986), the displacement pressure (Schowalter, 1979), the entry pressure (Robinson, 1966) are some of the most commonly used. These methods use a pore-throat size corresponding to an empirically determined X^{th} percentile of the volume of mercury intruded (e.g. Winland equation or displacement pressure). Based on scanning electron microphotographs of rock impregnated with Wood's metal Swanson (1977) empirically established an inflection on the mercury intrusion curve that represents the threshold ("apex" point) to a continuous, well-connected pore network. A similar method by Pittman (1992, 2001), which we used, has been shown to yield more accurate estimates of the critical throat size.

For permeability estimation, we used Swanson/Pittman relationships linking the critical apex radius (r_{apex}, μm), air-permeability (k, mD) and helium-porosity (ϕ). For the sandstone subsamples, we used the multiple regression established by Pittman based on 202 samples of sandstones from 14 formations ranging from Ordovician to Tertiary in age and showing a large variation in texture and composition:

$$\log(r_{apex}) = -0.117 + 0.475\log(k) + 0.099\log(\phi) \tag{6}$$

For the carbonate subsamples, we used a similar equation obtained from 15 carbonate samples belonging to the same geological formation as the samples on this study:

$$\log(r_{apex}) = 0.1233 + 0.3200\log(k) + 0.02397\log(\phi) \tag{7}$$

Calculated values of permeability are reported in Table 8.

In the expressions above the effect of porosity is insignificant, which means that the permeability is mostly controlled by the determination of the pore access at the apex radius, determined from MIP. The variability in the calculated permeability values is largest in sample *Carb-A* (156%), which showed the largest differences in the first part of the capillary curve slope (pressure range 10-800 psi). In general, the variations in

permeability observed at this fine scale is consistent with the variability observed in core plugs.

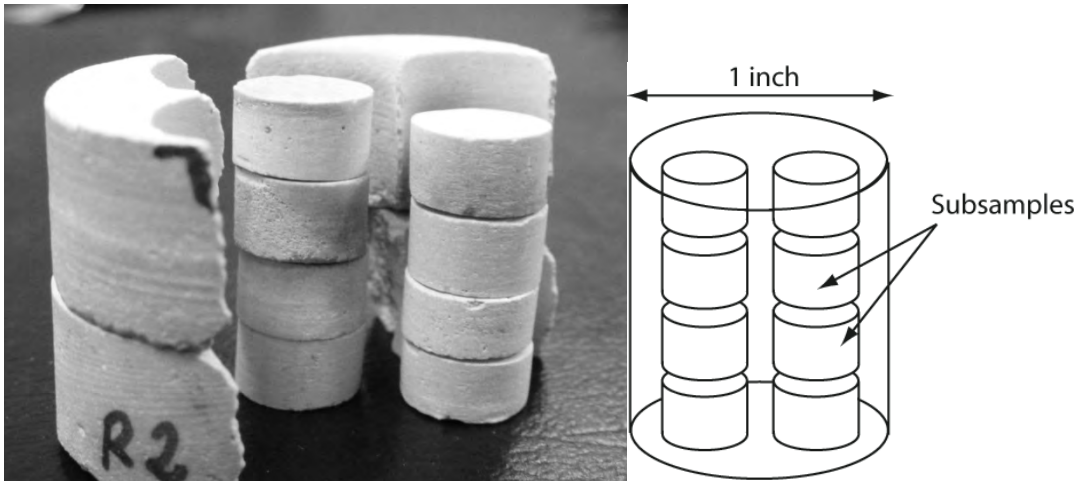

Figure 24: Photograph showing, for sample CarbA, the 8 subsamples extracted from the 1" cylindrical core plug.

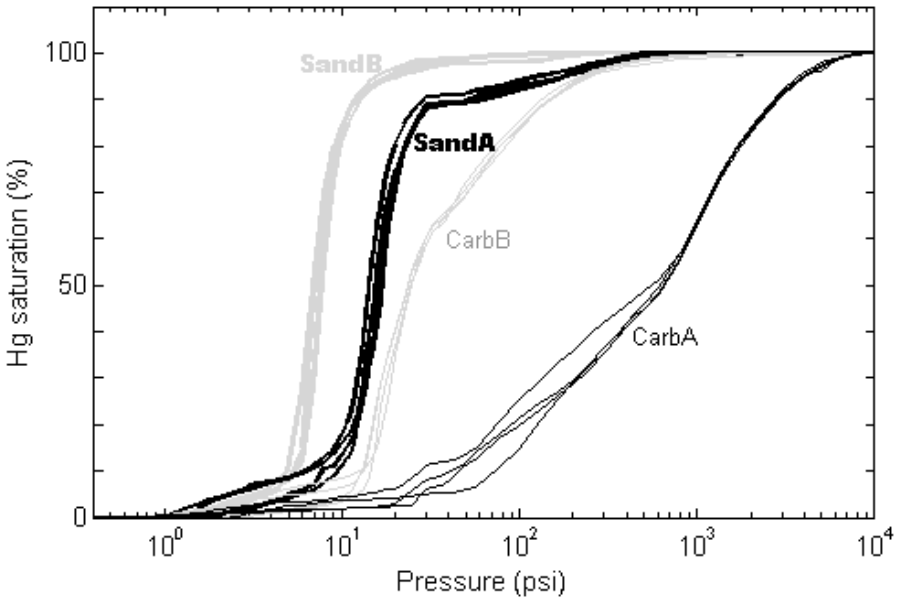

Figure 25: Capillary curves for all studied subsamples. The saturation of mercury (volume of mercury intruded normalized to its final value) is plotted as a function of increasing applied pressure.

Another approach for determining permeability is using the Kozeny-Carman equation, (Carman, 1937) which provides a link between porous medium properties and flow resistance in pore channels:

$$k_{KC} = \frac{1}{2}\frac{\phi^3}{S^2\tau^2} \tag{8}$$

where k_{KC} is the permeability, ϕ is the porosity, S is the specific surface area, and τ is the tortuosity. The Kozeny-Carman estimates are also shown in Table 8.

In order to relate type of microstructure to flow paths, permeability and reactivity, we subdivide the carbonate rock samples in different components, applying definitions in the literature to the qualitative analysis of the SEM images and the MIP tests. Traditionally, the two most commonly used petrographic classifications for carbonate rocks are those of Folk (1959) and Dunham (1962). They both divide carbonate rocks in three main components: (1) a framework of skeletal grains, (2) a matrix of microcrystalline calcite (i.e. micrite), whose grains are typically 1 to 4 μm in diameter (Moshier, 1989), and (3) spar calcite cement, with grains usually more than 10 μm in diameter (Moshier, 1989). Micrite can appear in various textures: from porous micrite with rounded to micro-rhombic crystals, to tight micrite with anhedral compact-to-fused crystals (Lambert et al., 2006; Deville de Periere (2006)). The different textures of micrite, because of the differences in the crystal shapes and type of intercrystalline contacts, will thus display different petrophysical properties, from poor to excellent porosity and permeability (Deville de Periere (2006)). Since we are here interested in relating microstructure to flow paths, instead of subdividing carbonates rocks in term of grains types, we divide them in term of pore throat type: (1) “macropores” with pore throats diameters > 20 μm, (2) intermediate pore throats diameters, between 0.5 and 20 μm and (3) small pore throats, less than 0.5 μm in diameter. The values of the pore throats delineating the three rocks components were chosen by analyzing the SEM images so that the components we defined ((2) and (3)) can also be related to the components in the Folk and Dunham classifications. The component (2) is a porous micrite with rounded to subrounded crystals and the component (3) is either a tight micrite, for sample CarbA, or a spar cement, for sample CarbB.

Table 8: Parameters obtained from mercury intrusion data and used to infer permeability values of each subsample. Parameter r_{apex} is the radius at the apex, used to determine permeability, k, from the Swanson/Pittman method. For the Kozeny-Carman calculation of permeability, k_{KC}, S is the specific surface area, and r is the effective pore throat size obtained by using the mixed pore size equation of Rumpf and Gupte (1971) and Dullien (1992).

	Swanson/Pittman		Kozeny-Carman		
	r_{apex} microns	k mD	r microns	S 1/microns	k_{KC} mD
SandA1	5.4	92	2.67	50634	60
SandA5	5.9	112	3.14	45628	88
SandA7	5.9	112	2.66	54931	64
SandA8	5.4	92	2.88	48628	72
SandB4	12.0	570	11.75	25144	2500
SandB5	12.0	568	10.74	26407	2046
SandB6	12.7	653	11.03	26926	2260
SandB8	12.7	649	8.66	34614	1406
CarbA1	0.8	2	0.093	263017	0.113
CarbA5	4.3	146	0.092	2715013	0.134
CarbA6	2.2	24	0.097	2723043	0.114
CarbA8	2.1	4	0.090	3226137	0.147
CarbB2	3.4	76	1.49	327877	70
CarbB4	4.5	156	1.60	328742	84
CarbB6	4.5	156	1.42	363091	65
CarbB7	3.9	110	1.43	345994	63

We then characterized each component in term of porosity, pore surface area and permeability by using the MIP data, combined with one of the Kozeny-Carman (Carman, 1961) expressions for permeability, as follow:

$$\phi_i = V_{Hg,i} / V_S \tag{9}$$

$$S_i = 2\sum_j \phi_i / r_j \tag{10}$$

$$k_i = \phi_i^3 / 2\tau^2 S_i^2 \tag{11}$$

where i refers to one the three components, ϕ_i is porosity, $V_{Hg,i}$ is the volume of mercury intruded, V_s is sample volume, and r_j is the pore throat radius. Values of porosity, specific surface area and permeability are given in Table 9 for each component (macropores, rounded micrite and tight micrite/spar cement) of each of the two rock types, CarbA and CarbB.

In order to know which mechanism (i.e., diffusion, advection or kinetic) is the controlling mass transport and reactivity in each of the three rock components, under given certain experimental conditions, we estimate the Dämkholer, Da, and Péclet, Pe, numbers, defined as:

$$Da = \frac{r_c L_c}{u} \tag{12}$$

$$Pe = \frac{u L_c}{D_f} \tag{13}$$

where r_c is the reaction rate, u the pore fluid velocity, L_c is a characteristic length relevant to the considered problem, and D_f the diffusion coefficient.

The effective pore fluid velocity, for each of the rock microstructure components i, can be expressed as a function of the experimental conditions and (effective) rock properties, in the formalism of Kozeny-Carman (flow through a circular pipe of an (effective) radius r), as follow:

$$u_i = \frac{4\pi \Delta P_i \, k_i}{\eta V_{s,i} \, S_i^2} \tag{14}$$

where ΔP_i is the pressure drop, η the fluid viscosity and V_{si} the volume of the rock component.

Using also the classical relation for the reaction rate,

$$r = \frac{S_r\, k_c\, (1-\Omega)}{C_{eq}} \tag{15}$$

where S_r is the reactive surface area, k_c the kinetic constant, $1-\Omega$ is the distance from equilibrium, and C_{eq} the concentration of considered species at the thermodynamical equilibrium (between the injected fluid and the calcite composing the rock). The Dämkholer and Péclet numbers can be rewritten as:

$$Da_i = \frac{S_{r,i} K_c (1-\Omega) \eta V_{s,i}}{C_{eq} 4\pi D_f} L_{c,i} \frac{S_i^2}{k_i} \tag{16}$$

$$Pe = \frac{4\pi \Delta P_i}{\eta V_{s,i} D_f} L_{c,i} \frac{k_i}{S_i^2} \tag{17}$$

These two numbers depend thus on the chosen conditions (fluid viscosity, pressure drop), system size and system intrinsic properties.

In table 9, we give order of magnitude estimates for the Péclet numbers of each rock component, by taking similar conditions as in the experiments of Vialle & Vanorio (2011), which consisted in injecting CO_2-rich water (pH=3.2) in core plugs, 1 inch in length and diameter, with a flow rate of ~10mL/min. Lc_i, the characteristic length, is taken here equal to $Ls.(f_i)^{1/3}$, where Ls is the core sample length and f_i the volume fraction of each rock component.

Given the limited amount of geochemical information available, it is difficult to precisely evaluate the Dämkholer number for each of the rock components. However a lower bound can be easily provided: indeed the Dämkholer number will be the smallest for the 'macropores' component (lower specific surface area and higher permeability). For this rock component, it is reasonable to assume that the system will be far from thermodynamical equilibrium, considering the high fluid velocities (high Péclet number), thus $\Omega \ll 1$. It leads to a lower bound of ~10 for Da, which means that, with experimental conditions similar as the one described by Vialle & Vanorio (2011), the regime is a transport limited regime for all rock components.

In Table 9, we can notice that, for both types of rocks CarbA and CarbB, the Péclet number is lower than 1 for the tight micrite/spar cement (*i.e.* advection rate smaller than diffusion rate), and greater than 1 for the rounded micrite and macropores (*i.e*. diffusion rate smaller than advection rate). In the tight micrite/spar cement component, dissolution is thus controlled by diffusion: the mass transfer of products and reactants is thus slow and the fluid is expected to be close to thermodynamical equilibrium with the calcite, leading to very little dissolution, if not all or even precipitation. In the microporous rounded micrite and macropores, dissolution is controlled by advection: because of an efficient mass transfer of reactants and products, the fluid remains acidic, far from thermodynamical equilibrium and the dissolution of calcite is important. These conclusions are consistent with the work of Vanorio at al. (2011) who observed, in samples from the same formation as sample CarbB, preferential dissolution of the microporous micrite, enlargement of the biggest pores and grain welding in the spar cement.

Table 9: Results of the semi-quantitative analysis relative to reactive transport in sample CarbB. For each of the three rock components (macropores, microporous rounded micrite and spar cement), fi is the corresponding pore volume fraction, phi the porosity, reff the effective radius (see text for calculation), S the specific surface area, k_{KC} the derived Kozeny-Carman permeability and Pe the Peclet number (see text for the details of the calculations).

	Macropores	**Microporous, rounded micrite**	**Spar Cement**
CarbB2			
fi	0.35	0.63	0.12
Phi	0.09	0.15	0.01
reff	21	1	6
S	$2\ 10^4$	$2\ 10^6$	$8\ 10^4$
k_{KC}	600	35	0.02
Pe	$5\ 10^3$	7	$9\ 10^{-3}$
CarbB4			
fi	0.40	0.58	0.02
Phi	0.11	0.15	0.01
reff	18	2	7
S	$3\ 10^4$	$2\ 10^6$	$8\ 10^4$
k_{KC}	700	35	0.01
Pe	$4\ 10^3$	7	$6\ 10^{-3}$
CarbB6			
fi	0.44	0.54	0.02
Phi	0.11	0.15	0.01
reff	18	2	5
S	$3\ 10^4$	$2\ 10^6$	$11\ 10^4$
k_{KC}	700	32	0.01
Pe	$5\ 10^3$	7	$2\ 10^{-3}$
CarbB7			
fi	0.44	0.54	0.02
Phi	0.09	0.15	0.01
reff	18	2	5
S	$3\ 10^4$	$2\ 10^6$	$10\ 10^4$
k_{KC}	500	35	0.03
Pe	$4\ 10^3$	8	$8\ 10^{-3}$

LABORATORY STUDY OF FLUID PROPERTIES

To better understand the behavior of CO_2-rich water under in-situ conditions of pressure and temperature, we have built a system designed to monitor the variation of the acoustic properties of fluids and gas-rich fluids under pressure and temperature variation. The apparatus (Figure 26) consists of a measurement cell, two PZT crystals that generate P waves, and a gas cell of known volume used as a reference to compute the amount of CO_2 injected at each experimental step. The measurement and the reference cells are connected to a fluid pump and a gas booster, respectively, and are both equipped with a compact transducer monitoring pressure (up to 40 MPa) and temperature (up to 125°C). The measurement cell can be heated by using a 120 VAC heater jacket and a controller system with adjustable set-point temperature ranging from 0 °C to 185 °C.

The entire system is connected to a PC with GPIB standard I/O, running a Labview^{TM}-based software environment, which controls a multichannel switch for real-time acquisition of pressure, temperature, and waveform data. The software allows setting the acquisition time interval (DT= 60 seconds for this experiment), performs an adaptive, automatic phase-picking of first arrival times based on waveform cross-correlation, and computes the mutual solubility of CO_2 and H_2O.

The results of the experimental test are reported in Figure 27 and refer to the acoustic measurements in CO_2-rich water performed under subcritical conditions (temperature equal to 23.75 °C; pressure up to 5.2 MPa). The experiment starts by injecting water into the measurement cell. The cell is previously evacuated to avoid air bubbles gathering inside the vessel, which could reduce the recorded acoustic signal. Once a pressure of 0.1 MPa is reached, velocity, pressure, and temperature data of the pure fluid are acquired as baseline. Then, the CO_2 stored in the reference cell is injected through 4 inlet points into the measurement cell, while velocity, pressure, and temperature are continuously monitored. We performed four injections which raised the pressure within the measurement cell by 1.27, 2.81, 4.82, and 5.2 MPa. After each injection, pressure decayed exponentially over time (Figure 27a) to a constant value representing the thermodynamic equilibrium of $CO_2 - H_2O$ mixture at that pressure and temperature.

To compute the bulk modulus of the CO_2-rich water from velocity data, we used the density data reported by Hebach et al., 2004 (Figure 27b). Figure 27b shows that the density of CO_2-rich water increases with pressure (red diamonds) and decreases with temperature (green diamonds). For comparison, we report the densities of pure phases of water and CO_2: for a given pressure and temperature, the density of CO_2-rich water (red diamonds- solid symbols) is higher than that of either pure water (red diamonds- open symbols) or pure CO_2 (blue diamonds). Figure 27c shows the variation of the bulk modulus as a function of pressure. The figure reports both the data collected in this study (blue symbols) and those measured by Liu (1998) (red symbols).

The results of Figure 27c show that the bulk modulus of CO_2-rich water increases with pressure (and by proxy CO_2 concentration) at a rate higher than that of pure water. Furthermore, the increase with pressure follows one of two distinct trends, depending on whether the measurement is taken at the injection or equilibrium point. This result highlights that the acoustic properties of CO_2-rich water evolve over time as the bulk modulus K increases from the time of injection (K_{inj}) until reaching the equilibrium (K_{eql}). When CO_2 dissolves into water, it forms the solvated molecule of CO_2 (aq) and the carbonic acid H_2CO_3. This latter partly dissociates to bicarbonate HCO^-_3 and carbonate CO^{2-}_3 ions shifting pH towards lower values. Although pressure decreases while dissolution proceeds (Figure 2a – *e.g.* from point D to D'), velocity slightly increases along with density, which leads the bulk modulus to increase (Figure 27c— *e.g.* from point D to D').

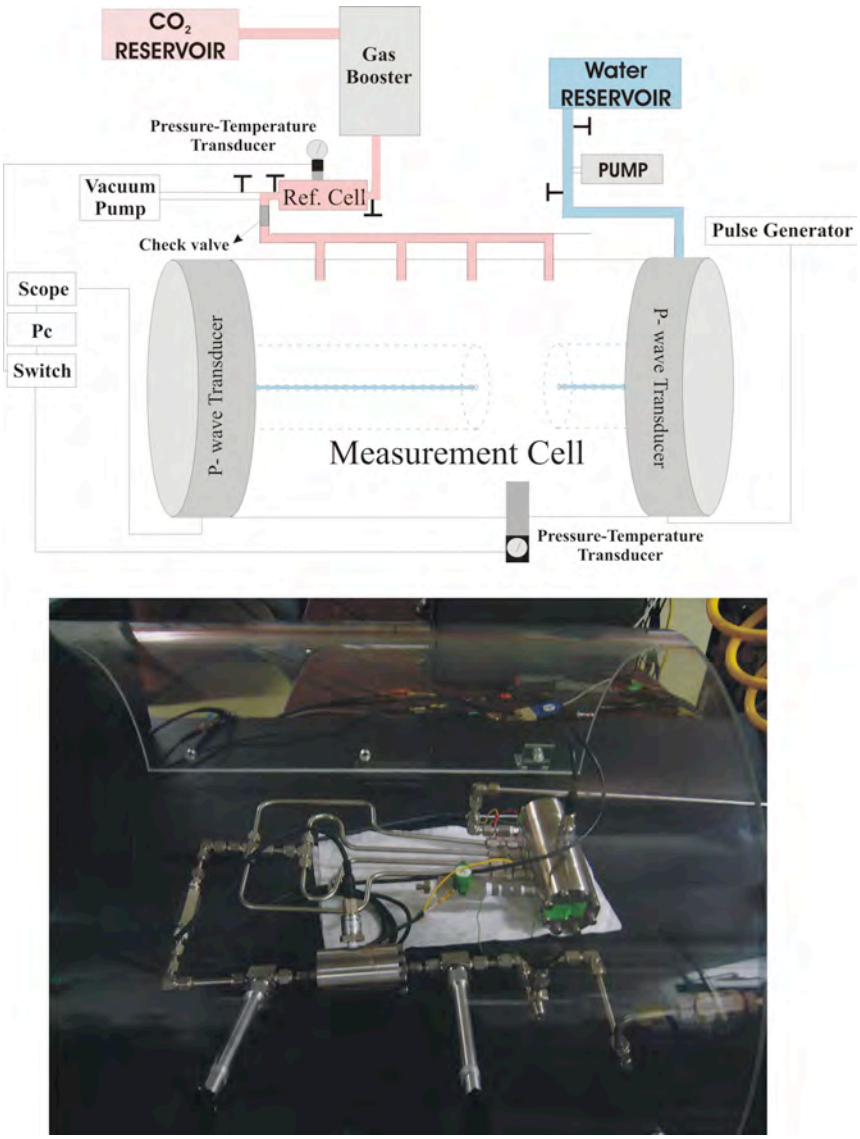

Figure 26. Experimental apparatus used in this study. The system is connected to a PC with GPIB standard I/O, running a Labview-based software for continuous, real-time acquisition of pressure, temperature, and waveform data.

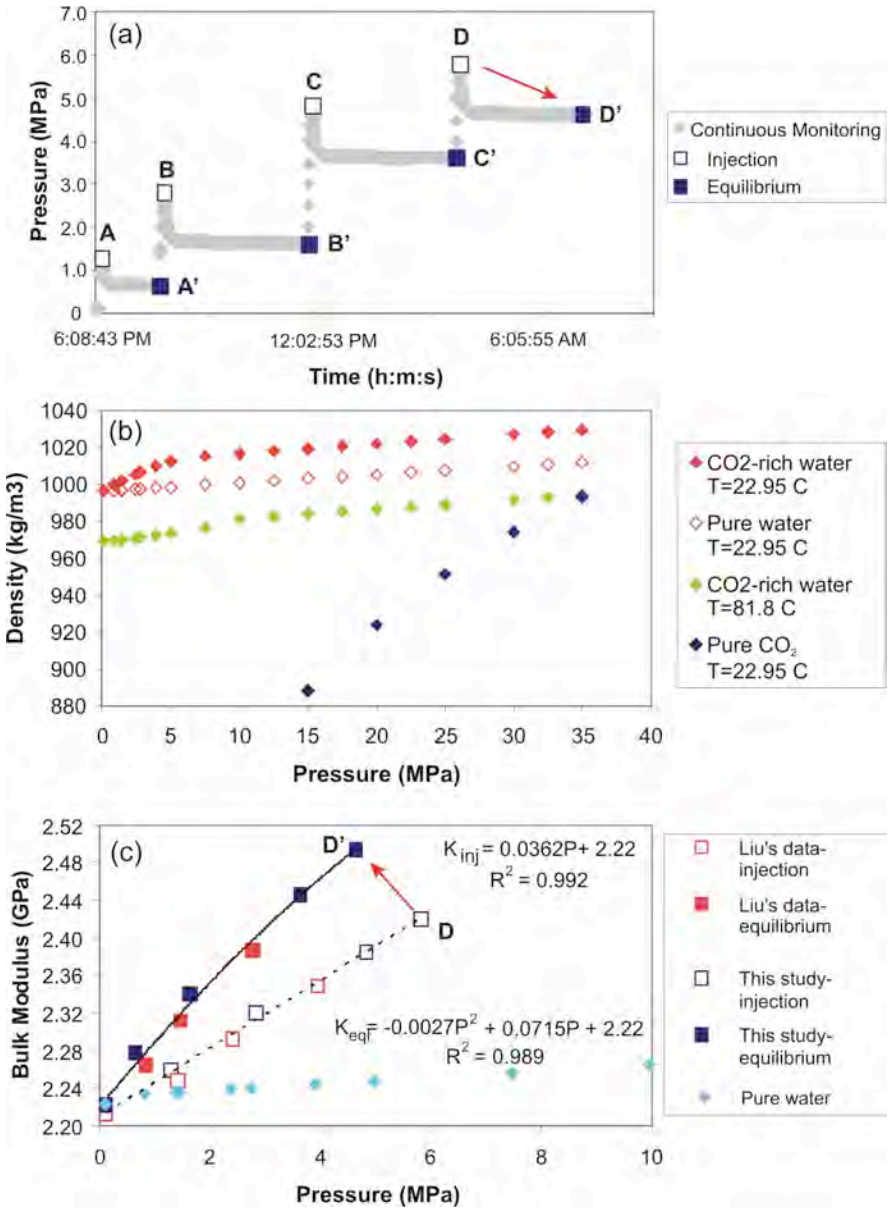

Figure 27. Properties of a CO_2-water solution as a function of pressure and temperature. (a) Real-time variation of pressure upon CO_2 injection and dissolution into water (1 bar deducted); (b) variation of density as a function of temperature and pressure for CO_2-rich water (T= 22.95 °C, solid red symbols; T= 81.8 °C, green symbols), pure CO_2 (blue symbols), and pure water (open red symbols); (c) variation of the bulk modulus of CO_2-rich water as a function of pressure and CO2 concentration (injection, open symbols; equilibrium, solid symbols). Data from Liu (1998) are reported for comparison. Preliminary results show that brine density and bulk modulus increase with increasing dissolved CO_2.

SIMULATION OF MIXED CO2-BRINE MIXTURES IN ROCK

We continued numerical simulations of frequency-dependent seismic velocities of mixed saturations of CO_2 and brine, which was introduced in our last report. We use the finite-element method (FEM) to solve quasi-static Biot equations with heterogeneous saturations of water and CO_2 phases. Moduli are determined by applying strain boundary conditions; then stress and strain components of the solid phase are averaged over the sample volume at every time step. Resulting time functions of stress and strain are then Fourier transformed to the frequency domain to calculate the frequency-dependent, complex bulk modulus, K, and attenuation, 1/Q, using the following relations:

$$K(\omega) = \frac{1}{3}\frac{\hat{\sigma}_{xx} + \hat{\sigma}_{yy} + \hat{\sigma}_{zz}}{\hat{\varepsilon}_{xx} + \hat{\varepsilon}_{yy} + \hat{\varepsilon}_{zz}}, \tag{18}$$

and

$$Q^{-1}(\omega) = \frac{\mathrm{Im}\{K\}}{\mathrm{Re}\{K\}}, \tag{19}$$

where σ_{jj} and ε_{jj} are the volume-averaged normal stress and strain components parallel to the j-axis, and a hat denotes the frequency transform of each quantity. An example heterogeneous saturation model is shown in Figure 28.

\

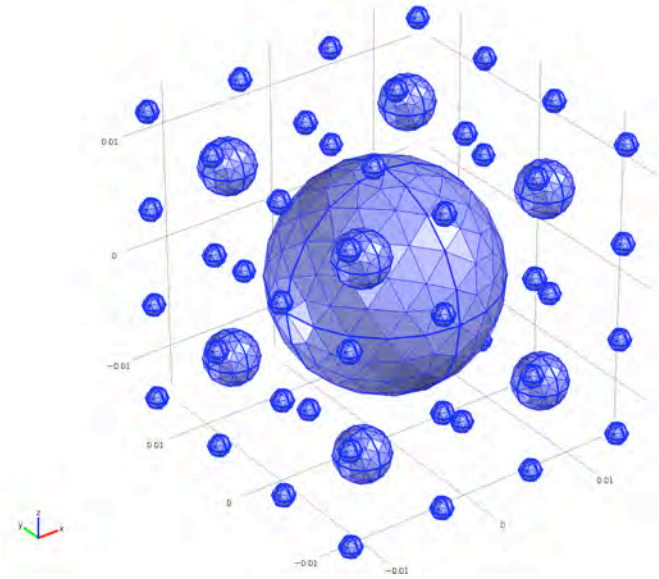

Figure 28. An example of representative elementary volume (REV) of periodic gas pockets in an otherwise brine-saturated rock.

We used the model to interpret published laboratory data of homogeneous limestone (Cadoret, 1993). Elastic velocities for three different wave frequencies (1, 50, and 500 kHz) were measured at various water saturations during both imbibition and drainage processes. The measurement in the drainage process, where the coarse-scale fluid mixture is observed in CT images, shows significantly larger velocities than in the imbibition process, particularly at high water saturation. We compared White's analytic solution and the numerical simulation with the data from the drainage process, where patchy saturation is expected. Rock and fluid properties used for the computation are listed in Table 10.

Patchy-saturation models comprising uniformly arranged, single-size spherical gas pockets are first investigated using White's (1975) solution. Figure 29 shows P-wave velocity (Vp) calculated on four such models for which the characteristic length (distance between gas pockets) lies between 0.8 and 3.2 cm. At high frequencies or with large gas pockets, Vp becomes rather linear, connecting the end members at zero and 100 percent water saturation; this implies an unrelaxed state or patchy saturation. In contrast, at low frequencies or with small-scale gas saturation, Vp takes a significantly lower value; the saturation state is regarded as homogeneous, where the effective fluid model is valid.

Table 10 Properties of the core sample by Cadoret (1993) and fluids

Solid phase:	
Rock type	limestone
Mineral bulk modulus (GPa)	76.8
Mineral density (kg/m^3)	2700
Dry frame bulk modulus (GPa)	8.632
Dry frame shear modulus (GPa)	6.375
Porosity	0.295
Permeability (m^2)	2.31×10^{-13}
Water:	
Bulk modulus (GPa)	2.25
Density (kg/m^3)	1000
Viscosity (Pa*s)	1.0×10^{-3}
Gas (air):	
Bulk modulus (MPa)	0.1
Density (kg/m^3)	100
Viscosity (Pa*s)	1.0×10^{-5}

Figure 29 implies that the dominant patch size (L) for these data falls between 0.8 and 1.6 cm (Figure 29c, d). It follows that we can estimate the dominant size of gas pockets by searching for the best fitting curve to the laboratory data. Applying a non-linear curve-fitting technique to the 50 and 500 kHz data simultaneously, we find that a gas pocket of L = 1.16 cm gives the best-fitting Vp curves. Figure 30a shows the best-fitting White's curve along with the laboratory data. Although the general trend of the best-fitting curve agrees with the laboratory measurement, there are discrepancies at low saturations for 500 kHz data and at high saturations for 50 kHz data. Figure 30b shows a Vp curve computed by numerical simulation with the same gas spacing (L=1.16 cm). The curves are similar to the ones obtained with White's formula, but better follow the overall trend

of laboratory data, particularly at low water saturations for 500 kHz. This comparison suggests the water saturation forms compact patches rather than eggshell-thin shells in the real rocks when water saturation is low.

In natural rocks, the fluid distribution is inherently complex. Due to the heterogeneity of the pore space, patches of various scales occur during fluid replacement. We numerically simulated combinations of two different scales of gas pocket to determine how the bulk properties deviate from those for the single patch models. Two contrasting variations for the combination of patch scale are investigated; introducing coarser gas pockets to fixed arrangements of finer gas pockets, and vice versa.

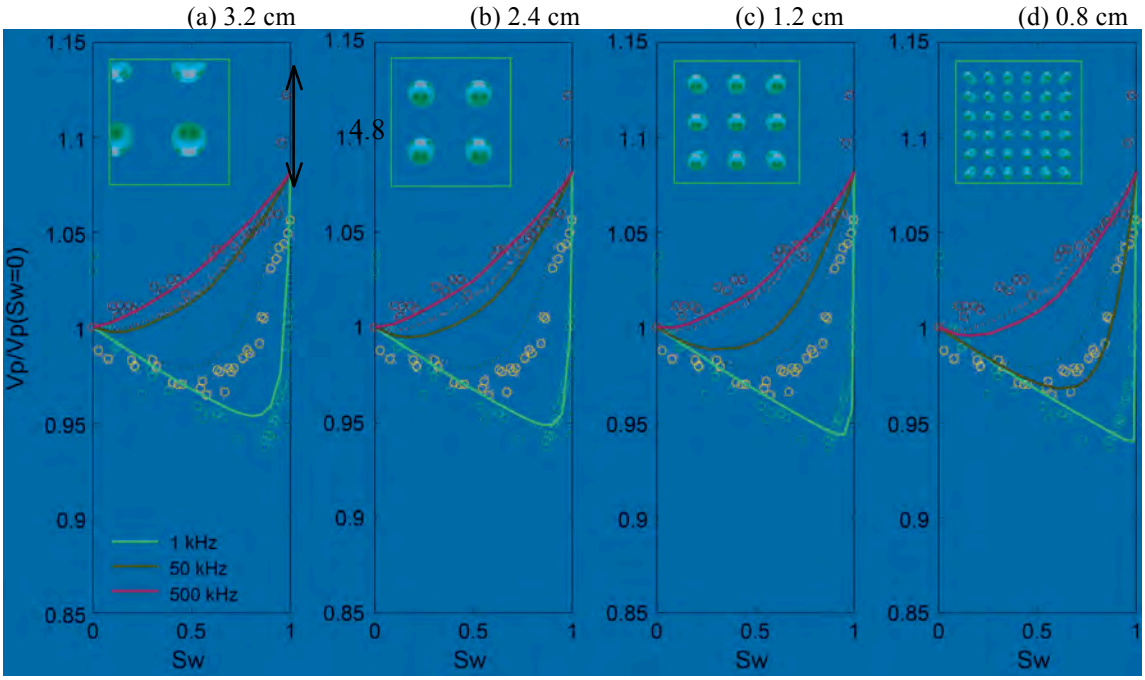

Figure 29. Comparison of P-wave velocity with White equation (curves) with the laboratory measurement by Cadoret (1993) (circles). The caption indicates the spacing between gas pockets.

First, three different spacings (L) of gas pocket, 1.2, 2.4, and 4.8 cm, are added to a finer-scale background gas distribution of 0.8 cm. Finer and coarser gas pockets each occupy one half of the total gas saturation in each model. Figure 31 shows numerically computed Vp-Sw curves. All the models (a) through (d), which share L = 0.8 cm for background gas pockets, show quite similar behavior. This is because the overall characteristics of the curves, including the slopes at high values of Sw, are not

significantly affected by the larger gas patches but are primarily governed by the finer gas saturation. Nonetheless, there is systematic change between these models, where Vp curves shift toward the "patchy limit" as the larger gas pockets expand.

The second variation for the saturation model is made by introducing the finer gas pockets (0.4, 0.8, 1.2, 1.6 cm) into the fixed background of coarser gas pockets with L = 2.4 cm. Vp increases to the patchy limit with increasing scale of the finer gas saturation. The variation in Vp here is more significant than in Figure 29, because the finer gas saturation is changing in size, which largely affects the transition frequency of dispersion and therefore the Vp-Sw relationship.

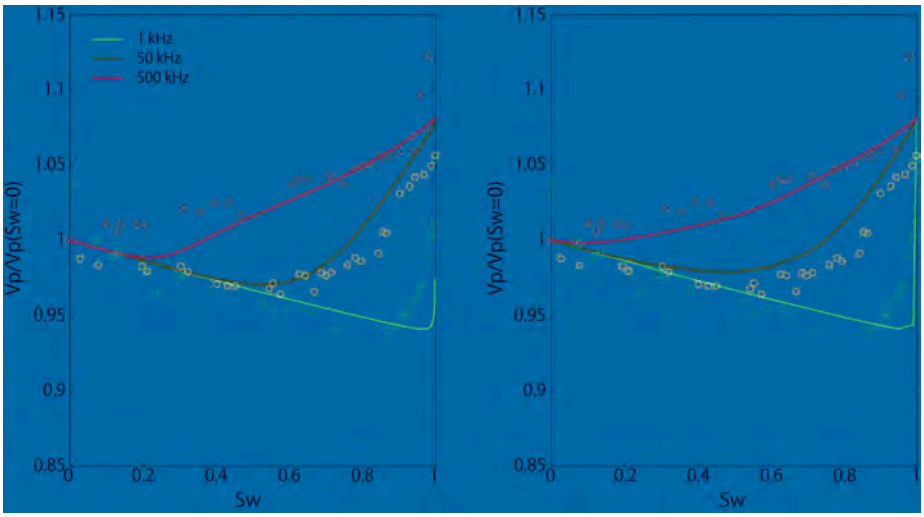

Figure 30 Comparison of White's solution (left) and FEM result (right) with the laboratory data by Cadoret (1993) (circles). The equivalent sphere radius to L = 1.16 cm is used for White's solution.

Figures 31 and 32 show that the combination of 2.4 and 0.8 cm (Figure 31b and Figure 32c) is most consistent with the laboratory data. Further comparison with the best fitting single-scale saturation curves (dashed curves) reveals that the mixed-scale gas saturation model improves the fit with the laboratory data.

In summary, we numerically simulated diffusion-induced seismic dispersion by solving the quasi-static approximation of Biot's field equations. Simulation results on single-scale gas pockets show good agreement with White's analytical solution at high water saturation. However, deviations occur at low water saturation due to the different boundary conditions of the two schemes. Mixed-scale gas pocket models reveal that the transition frequency is primarily governed by the gas pocket of the finest scale. In the

two-scale cases, if the gas is very stiff and the total saturation of the finer gas pocket is sufficiently small compared to that of the coarser gas pocket, the resulting dispersion curve may have a two-step feature. The composition of White's analytical curves for each single-size gas patch with modified solid and fluid properties is found to closely match the dispersion curve for two-scale gas pockets.

Comparison of numerical results with published laboratory measurements on P-wave velocity demonstrates the possibility of estimating the dominant scale of gas pockets. Computations on mixed-scale gas distributions show that the laboratory data are better reproduced with mixed-scale gas saturations than with single-scale models. Estimation of saturation scale delivers a more reliable modulus-saturation relationship, given a wave frequency and other field parameters, which may improve seismic interpretation and fluid monitoring.

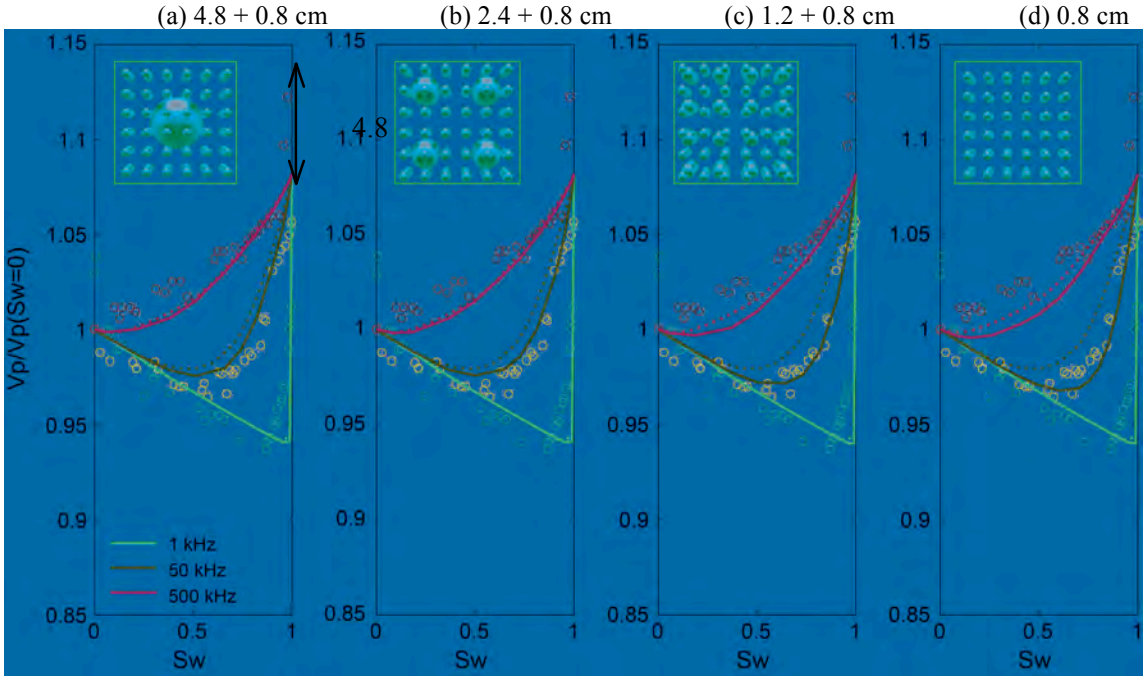

Figure 31 Comparison of numerically derived P-wave velocity (curves) with the laboratory measurement by Cadoret (1993) (circles). The caption indicates the spacing of gas pockets. The dashed curves are numerically derived with a single-size (L=1.16 cm) patch model.

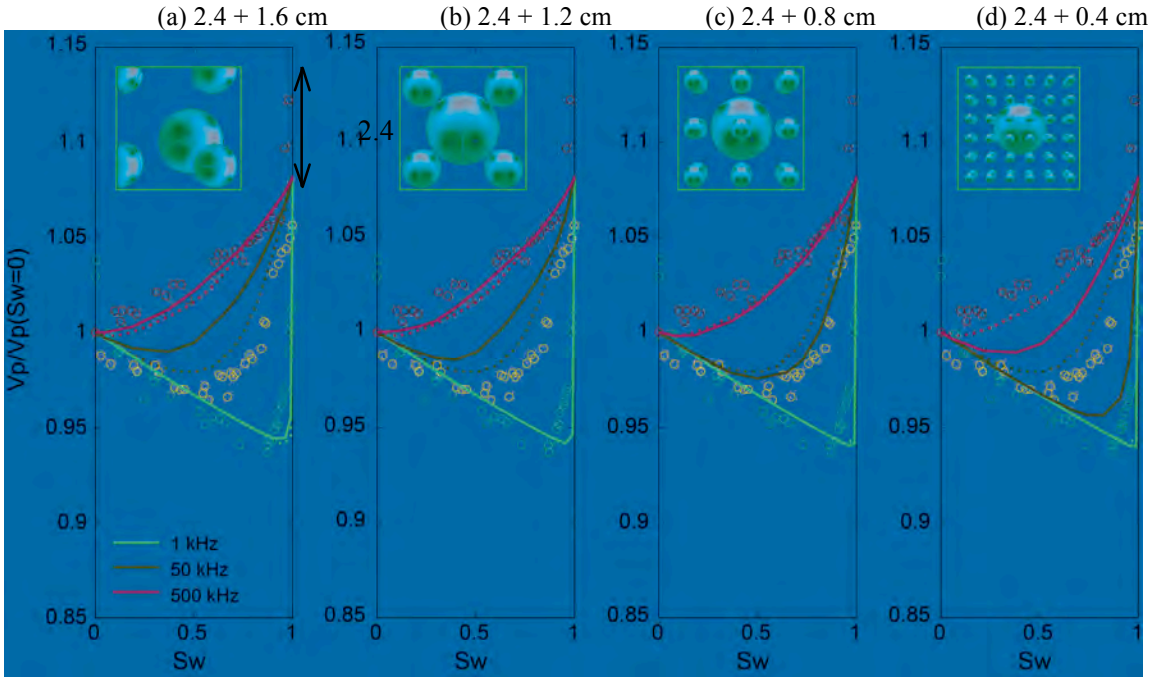

Figure 32. Comparison of numerically derived P-wave velocity (curves) with the laboratory measurement by Cadoret (1993) (circles). The caption indicates the spacing of gas pockets. The dashed curves are numerically derived with a single-size (L=1.16 cm) patch model.

EXACT EQUATIONS FOR SUBSTITUTION OF FLUID, GRAIN AND POROSITY

[*Key publication: Saxena and Mavko, 2014*]

Rock-physics aims to link seismic attributes (Vp/Vs, acoustic impedance, rock stiffness, etc) to properties of the subsurface (pore-fluid, mineralogy, pore geometry, etc). Rock-physics models can also be used to address *what if* scenarios which are of interest in hydrocarbon exploration. One of the most successful rock physics models is Gassmann's fluid substitution theory (Gassmann, 1951), which predicts the change in low-frequency seismic velocities or rock stiffness upon change in pore-fluid. In part, the success of Gassmann's theory is due to the fact that all required inputs are either usually known or directly measured, with no adjustable parameters; these relations can be written as

$$\frac{\left(\frac{1}{K_{dry}}-\frac{1}{K_{ud}}\right)}{\left(\frac{1}{K_{ud}}-\frac{1}{K^B}\right)\left(\frac{1}{K_{dry}}-\frac{1}{K^B}\right)}=\frac{1}{\varphi\left(\frac{1}{K^f}-\frac{1}{K^B}\right)}\quad , \tag{20}$$

and

$$\mu_{ud}=\mu_{dry}\quad , \tag{21}$$

where K_{ud} and K_{dry} are un-drained (fluid saturated) and dry rock bulk moduli, respectively; μ_{ud} and μ_{dry} are the corresponding shear moduli; K^f and K^B are bulk moduli of the pore-fluid and the mineral in rock frame; ϕ is the volume fraction of pores (porosity). Equations 20 and 21 are exact if

i. rock frame is monomineralic (i.e., single mineral)
ii. initial and final pores are fully saturated with ideal elastic fluids
iii. load-induced pore-pressure under quasi-static deformation is homogeneous
iv. upon substitution there is no change to rock microstructure
v. only the pore phase is substituted.

Brown and Korringa (1975) extended Gassmann's equations to the case of multimineralic rock frame (of mixed mineralogy) thus relaxing assumption (i). Ciz and Shapiro (2007) further generalized Brown and Korringa's results to rocks with solid-filled pores, thus further relaxing assumptions (ii) and (iii). Still, these extensions are fundamentally limited to situations where only *one* phase is substituted and there is *no* change in the pore geometry. There are many problems for which we need to further relax assumptions (iv) and (v). Pore geometry can change due to a variety of geological processes: digenesis, sorting, partial melting/freezing, mineral precipitation, etc. For such problems, inclusion based effective medium models (Wu, 1966; O'Connell and Budiansky, 1974; Kuster and Toksöz, 1974; Berryman, 1980; Cleary et al., 1995), can provide insightful approximate predictions since these loosely relax assumptions (i)-(v), however, these models idealize rock microstructure with ellipsoids and require adjustable parameters such as aspect ratios, which are also poorly determined.

In this section, we further relax assumptions (i)-(v) and obtain *exact* solutions for arbitrary pore shape and mixed mineralogy, such that pore geometry can change and more than one phase can be substituted simultaneously.

Digenetic trends are usually modeled (Avseth et al., 2010; Dvorkin and Nur, 1996) by mixing the high-porosity cemented sand-point with the mineral-point using the upper Hashin-Shtrikman (HS) bound (Hashin and Shtrkiman, 1963). Similarly, sorting trends are modeled with the lower HS bound. Although such heuristic approaches have been fairly successful (Avseth et al., 2005) we note that if assumptions (i)-(v) are relaxed, change in rock stiffness due to digenesis, sorting and other geologic processes, can be rigorously modeled and predicted.

Change in pore geometry can also occur due to dissolution/precipitation which typically leads to partial replacement of existing and/or formation of new phases (Hoefiner and Fogler, 1988; Guen et al., 2007; Vanorio et al., 2011; Vialle and Vanorio, 2011; Bemer et al., 2013). In such situations, since modeling fluid or solid substitution is also accompanied by changes in pore geometry, traditional fluid or solid substitution approaches cannot be employed. For example, assumption (iv) in Gassmann's fluid substitution theory will be violated when modeling time-lapse seismic signatures of subsurface movement of chemically reactive CO_2 due to possible changes in the rock frame (Lumley, 2010).

Additionally, there are also situations where more than one phase in a multimineralic rock needs to be substituted; fundamentally this is equivalent to the problem of predicting rock stiffness change due to changing pore geometry. Examples of such problems include only partially substituting a pore-fill phase in a multimineralic rock - a situation encountered while modeling effects of steam injection in heavy oil reservoirs (Schmitt, 1999; Bianco et al., 2008; Chopra et al., 2010). Similar situations occur when modeling rock stiffness change due to partial melting (Duputel et al., 2009) or due to partial pore-fluid freezing in permafrost (Timur, 1968; Kurfurst, 1976; King, 1977; Zimmerman and King, 1986; King et al., 1988; Jacoby et al., 1996; Sondergeld and Rai, 2007).

Exact substitution equations

Consider an isotropic composite (rock) with N elastic phases, such that each phase q ($q \in N$) has volume fraction ϕ_q with its bulk and shear moduli given by K^{q1} and μ^{q1}, respectively. Upon substitution, moduli of all but one of these phases change to K^{q2} and μ^{q2}; for convenience, we name the un-changing phase as B ($B \in N$). Then, the exact bulk modulus equation for substitution of N-1 phases in a N phase composite is:

$$\frac{\left(\frac{1}{K_{ud}^{(1)}}-\frac{1}{K_{ud}^{(2)}}\right)}{\left(\frac{1}{K_{ud}^{(1)}}-\frac{1}{K^{B}}\right)\left(\frac{1}{K_{ud}^{(2)}}-\frac{1}{K^{B}}\right)}=\sum_{\substack{q=1\\ q\neq B}}^{N}\frac{\left(\frac{1}{K^{q1}}-\frac{1}{K^{q2}}\right)\alpha_1^q+\left(\frac{1}{\mu^{q1}}-\frac{1}{\mu^{q2}}\right)\alpha_2^q}{\varphi_q\left(\sum_{\substack{r=1\\ r\neq B}}^{N}\left(\frac{1}{K^{r1}}-\frac{1}{K^{B}}\right)\frac{\varphi_r\overline{P^{r1}}}{\varphi_q\overline{P^{q1}}}\right)\left(\sum_{\substack{r=1\\ r\neq B}}^{N}\left(\frac{1}{K^{r2}}-\frac{1}{K^{B}}\right)\frac{\varphi_r\overline{P^{r2}}}{\varphi_q\overline{P^{q2}}}\right)} \quad . \tag{22}$$

where $K_{ud}^{(1)}$ and $K_{ud}^{(2)}$ are initial and substituted effective bulk moduli, respectively. In equation 22, r is a dummy index which sums over all phases except for phase B. In equation 22, P^q is the bulk compression-induced pressure (mean-stress) in any phase q, related to the induced Cauchy stress tensor σ_{ij}^q as

$$\sigma_{ij}^q = -P^q\delta_{ij} + \tau_{ij}^q \ , \tag{23}$$

where τ_{ij}^{q} are the bulk compression-induced deviatoric stresses in any phase *q*. For each phase stresses are related to strains by Hooke's law

$$P^{q} = -K^{q} e^{q} \quad , \tag{24}$$

$$\tau_{ij}^{q} = 2\mu^{q} \gamma_{ij}^{q} \quad . \tag{25}$$

In equations 24 and 25, e^{q} and γ_{ij}^{q} are the mean and deviatoric parts of strain induced in any phase *q*, respectively. Here we use standard summation convention over repeated indices and symbol δ_{ij} is the Kronecker delta function. Symbol $\overline{\Omega^{q}}$ denotes the volume average of any quantity Ω^{q} (over the volume of phase *q*). The parameters α_1^{q} and α_2^{q} for each substituted phase *q* are defined as

$$\alpha_1^{q} = \frac{\overline{P^{q1} P^{q2}}}{\overline{P^{q1}}\,\overline{P^{q2}}} = \frac{\overline{e^{q1} e^{q2}}}{\overline{e^{q1}}\,\overline{e^{q2}}}; \quad \alpha_2^{q} = \frac{1}{2}\frac{\overline{\tau_{ij}^{q1} \tau_{ij}^{q2}}}{\overline{P^{q1}}\,\overline{P^{q2}}} = 2\frac{\mu^{q1}\mu^{q2}}{K^{q1}K^{q2}}\frac{\overline{\gamma_{ij}^{q1}\gamma_{ij}^{q2}}}{\overline{e^{q1}}\,\overline{e^{q2}}} \quad . \tag{26}$$

Similarly, the exact substitution equation for shear modulus is

$$\frac{\left(\frac{1}{\mu_{ud}^{(1)}} - \frac{1}{\mu_{ud}^{(2)}}\right)}{\left(\frac{1}{\mu_{ud}^{(1)}} - \frac{1}{\mu^{B}}\right)\left(\frac{1}{\mu_{ud}^{(2)}} - \frac{1}{\mu^{B}}\right)} = \sum_{\substack{q=1 \\ q\neq B}}^{N} \frac{\left(\frac{1}{\mu^{q1}} - \frac{1}{\mu^{q2}}\right)\beta_1^{q} + \left(\frac{1}{K^{q1}} - \frac{1}{K^{q2}}\right)\beta_2^{q}}{\phi_q \left(\sum_{\substack{r=1 \\ r\neq B}}^{N}\left(\frac{1}{\mu^{r1}} - \frac{1}{\mu^{B}}\right)\frac{\phi_r \overline{\tau_{12}^{r1}}}{\phi_q \overline{\tau_{12}^{q1}}}\right)\left(\sum_{\substack{r=1 \\ r\neq B}}^{N}\left(\frac{1}{\mu^{r2}} - \frac{1}{\mu^{B}}\right)\frac{\phi_r \overline{\tau_{12}^{r2}}}{\phi_q \overline{\tau_{12}^{q2}}}\right)} \quad , \tag{27}$$

where $\mu_{ud}^{(1)}$ and $\mu_{ud}^{(2)}$ are initial and substituted effective shear moduli; P^{q} and τ_{ij}^{q} are shear field-induced pressure and deviatoric stresses. The parameters β_1^{q} and β_2^{q} for each phase *q* are defined as

$$\beta_1^{q} = \frac{1}{2}\frac{\overline{\tau_{ij}^{q1}\tau_{ij}^{q2}}}{\overline{\tau_{12}^{q1}}\,\overline{\tau_{12}^{q2}}} = \frac{1}{2}\frac{\overline{\gamma_{ij}^{q1}\gamma_{ij}^{q2}}}{\overline{\gamma_{12}^{q1}}\,\overline{\gamma_{12}^{q2}}}; \quad \beta_2^{q} = \frac{\overline{P^{q1}P^{q2}}}{\overline{\tau_{12}^{q1}}\,\overline{\tau_{12}^{q2}}} = \frac{1}{4}\frac{K^{q1}K^{q2}}{\mu^{q1}\mu^{q2}}\frac{\overline{e^{q1}e^{q2}}}{\overline{\gamma_{12}^{q1}}\,\overline{\gamma_{12}^{q2}}} \quad . \tag{28}$$

Parameter α_1^q describes the heterogeneity of compression-induced pressure in any phase q; whereas parameter α_2^q describes the contribution of compression-induced deviatoric stresses in any phase q. Similarly, parameter β_1^q describes the heterogeneity of shear field-induced deviatoric stresses and the parameter β_2^q describes the contribution of shear field-induced pressure.

Under the assumptions (i)-(v), equations 22 and 27 reduce to Gassmann's equations (20 and 21) which can be easily checked. Relaxing only the first assumption (i) but still assuming (ii)-(v), for shear modulus we recover Gassmann's result in equation 21, and for bulk modulus we obtain an algebraically *different* but fundamentally *identical* equation than that previously derived by Brown and Korringa. This new result is

$$\frac{\left(\frac{1}{K_{dry}}-\frac{1}{K_{ud}}\right)}{\left(\frac{1}{K_{ud}}-\frac{1}{K^B}\right)\left(\frac{1}{K_{dry}}-\frac{1}{K^B}\right)}=\frac{1}{\varphi\left(\frac{1}{K^f}-\frac{1}{K^M}\right)\left(\frac{K^{M-dry}K^M}{K^BK^B}\right)}\ . \tag{29}$$

Equation 29 features two additional stiffnesses given by

$$K^M=K^B+\sum_{\substack{r=1\\ r\neq B,f}}^{N}\frac{\phi_r\overline{e^r}}{\phi e^f}\left(K^B-K^r\right)\ \ ;K^{M-dry}=K^B+\sum_{\substack{r=1\\ r\neq B,f}}^{N}\frac{\phi_r\overline{e^{r-dry}}}{\phi e^{f-dry}}\left(K^B-K^r\right), \tag{30}$$

where, e^f and e^{f-dry} are compression induced fluid-saturated and dry pore volumetric strains, respectively; $\overline{e^r}$ and $\overline{e^{r-dry}}$ are the induced volumetric strains (volume averaged) in phase r ($r \in N$), when pores are fluid-saturated and dry, respectively. Note that K^{M-dry} is a "dry" rock property, thus is independent of fluid modulus, whereas K^M depends on the fluid modulus. Further relaxing assumptions (ii) and (iii) we can obtain the solid substitution solutions discussed in Saxena and Mavko (2014).

Equations 22 and 27, also relax assumptions (iv) and (v). This is so since these relations allow for substitution of all but one phase in an isotropic multimineralic rock, which also allows for modeling change in rock microstructure. For example, consider a two-phase monomineralic dry rock; we can divide, albeit virtually, this two-phase

composite into a three-phase system: two phases of the (same) mineral in the frame (of identical elastic stiffness) and one phase of dry pores; therefore one of the mineral phases can be substituted thus changing the rock pore geometry.

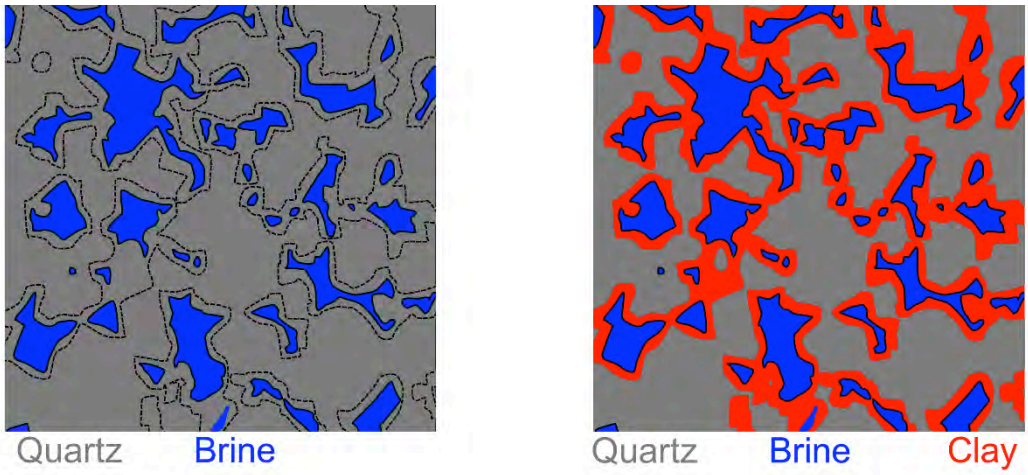

(a) (b)

Figure 33: (a) 2D slide of a digital 3D Fontainebleau sandstone sample (Andrä et al., 2013), composed of quartz grains (in gray) and brine saturated pores (in blue), dashed black lines show imaginary cuts. (b) Digitally altered sandstone sample with the region between pore boundaries and imaginary cuts (in Figure 33a) replaced with clay (in red).

As an illustration of the exact solution in equations 22 and 27, we now consider a 3D digital Fontainebleau sandstone sample (porosity 0.15; Andrä et al., 2013). Mineral frame of a Fontainebleau sandstone is typically composed of quartz grains (bulk modulus 36 GPa and shear modulus 45 GPa), but in this exercise we digitally alter a part of quartz grains and replace them with a pore-lining clay phase (bulk modulus 21 GPa and shear modulus 15 GPa). Such that the total volume fraction of clay is 0.27. 2D slices of the original 3D and the digitally altered samples are shown in Figures 33a and 33b, respectively. We assume that the pores are occupied (for both cases) with brine (bulk modulus 3 GPa and shear modulus 0 GPa). Using the FEM, we calculate the effective bulk moduli of the original and clay sandstone to be 25.6 GPa and 21.7 GPa, respectively. For the FEM calculation we apply bulk strain of magnitude 0.003; Figure 34 shows the induced pressure (negative of mean stress) in each phase.

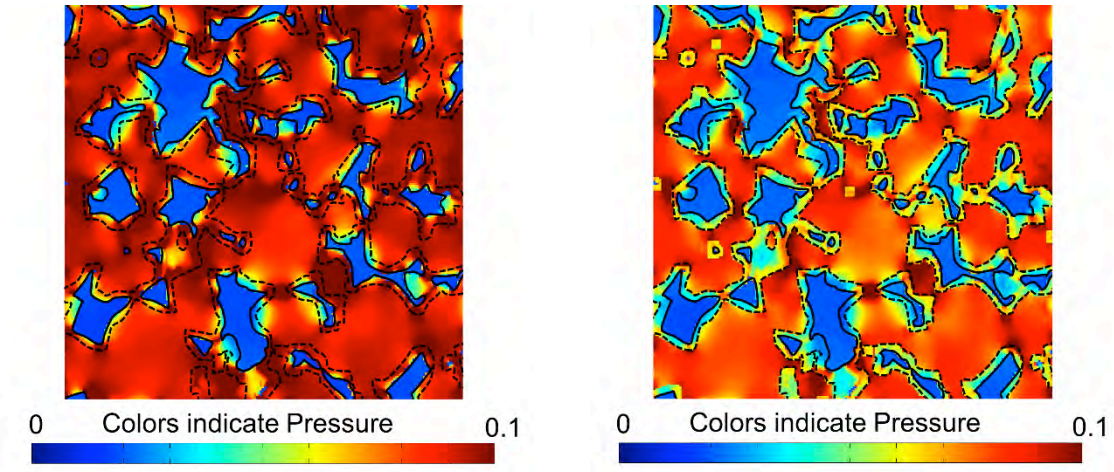

(a) (b)

Figure 34: (a) induced pressure upon compression in the original sandstone. (b) Induced pressure in clay sandstone. Color scale is normalized with the same maximum value for both (a) and (b) for direct comparison.

Now we will compare the FEM computed effective bulk modulus of the original rock (with all quartz grains), with that predicted by equation 22 starting with the FEM computed bulk modulus of the clay sandstone. The required parameters are: the ratio of volume averaged pressure induced in brine and clay phases in the clay sandstone which is equal to 0.4 (from the FEM), and the ratio of volume averaged pressure induced in brine and quartz (for only the part which has replaced clay) which is equal to 0.22. Also needed are parameters α_1 and α_2 corresponding to the substituted phase (clay to quartz); for these parameters the FEM computed values are $\alpha_1 = 1.13 \text{and} \alpha_2 = 0.16$. Using these inputs, equation 22 predicts the bulk modulus of the original sandstone to be 25.6 GPa, which matches the FEM computed value. In the next sections, we discuss how equations 22 and 27 can be used in practice.

Substitution of two phases in a three phase composite: Exact solutions

For the limiting case of substitution of two phases in a three phase multimineralic isotropic rock, such that fluid/solid phases $f1$ and $m1$ (volume fractions ϕ_f and ϕ_m) are to be replaced with new phases $f2$ and $m2$, respectively, our exact results in equations 22 and 27 reduce to

$$\frac{\left(\frac{1}{K_{ud}^{(1)}}-\frac{1}{K_{ud}^{(2)}}\right)}{\left(\frac{1}{K_{ud}^{(1)}}-\frac{1}{K^{B}}\right)\left(\frac{1}{K_{ud}^{(2)}}-\frac{1}{K^{B}}\right)}= \frac{\left(\frac{1}{K^{f1}}-\frac{1}{K^{f2}}\right)\alpha_1^f+\left(\frac{1}{\mu^{f1}}-\frac{1}{\mu^{f2}}\right)\alpha_2^f+\frac{\phi_m}{\phi_f}\frac{\overline{P^{m1}}\,\overline{P^{m2}}}{\overline{P^{f1}}\,\overline{P^{f2}}}\left(\left(\frac{1}{K^{m1}}-\frac{1}{K^{m2}}\right)\alpha_1^m+\left(\frac{1}{\mu^{m1}}-\frac{1}{\mu^{m2}}\right)\alpha_2^m\right)}{\phi_f\left(\frac{1}{K^{f1}}-\frac{1}{K^{B}}+\left(\frac{1}{K^{m1}}-\frac{1}{K^{B}}\right)\frac{\phi_m}{\phi_f}\frac{\overline{P^{m1}}}{\overline{P^{f1}}}\right)\left(\frac{1}{K^{f2}}-\frac{1}{K^{B}}+\left(\frac{1}{K^{m2}}-\frac{1}{K^{B}}\right)\frac{\phi_m}{\phi_f}\frac{\overline{P^{m2}}}{\overline{P^{f2}}}\right)} \tag{31}$$

,

and

$$\frac{\left(\frac{1}{\mu_{ud}^{(1)}}-\frac{1}{\mu_{ud}^{(2)}}\right)}{\left(\frac{1}{\mu_{ud}^{(1)}}-\frac{1}{\mu^{B}}\right)\left(\frac{1}{\mu_{ud}^{(2)}}-\frac{1}{\mu^{B}}\right)}= \frac{\left(\frac{1}{\mu^{f1}}-\frac{1}{\mu^{f2}}\right)\beta_1^f+\left(\frac{1}{K^{f1}}-\frac{1}{K^{f2}}\right)\beta_2^f+\frac{\phi_m}{\phi_f}\frac{\overline{\tau_{12}^{m1}}\,\overline{\tau_{12}^{m2}}}{\overline{\tau_{12}^{f1}}\,\overline{\tau_{12}^{f2}}}\left(\left(\frac{1}{\mu^{m1}}-\frac{1}{\mu^{m2}}\right)\beta_1^m+\left(\frac{1}{K^{m1}}-\frac{1}{K^{m2}}\right)\beta_2^m\right)}{\phi_f\left(\frac{1}{\mu^{f1}}-\frac{1}{\mu^{B}}+\left(\frac{1}{\mu^{m1}}-\frac{1}{\mu^{B}}\right)\frac{\phi_m}{\phi_f}\frac{\overline{\tau_{12}^{m1}}}{\overline{\tau_{12}^{f1}}}\right)\left(\frac{1}{\mu^{f2}}-\frac{1}{\mu^{B}}+\left(\frac{1}{\mu^{m2}}-\frac{1}{\mu^{B}}\right)\frac{\phi_m}{\phi_f}\frac{\overline{\tau_{12}^{m2}}}{\overline{\tau_{12}^{f2}}}\right)} \tag{32}$$

.

Approximate bounds for weak contrast in substituted phases

Assuming relatively homogeneous load induced stresses yields: $\alpha_1^{f,m}\approx 1$ and $\beta_1^{f,m}\approx 1$. For composites with homogeneous induced stresses, we (Saxena and Mavko, 2014) have shown that $\alpha_1 >> \alpha_2$ and $\beta_1 >> \beta_2$, thus if $K^{f1}\approx K^{f2}$ and $\mu^{f1}\approx\mu^{f2}$ we can neglect the terms corresponding to parameters $\alpha_2^{f,m}$ and $\beta_2^{f,m}$ in equations 31 and 32, which is equivalent to assuming $\alpha_2^{f,m}\approx 0$ and $\beta_2^{f,m}\approx 0$. Under these assumptions, both equations 31 and 32 can be compactly written as

$$\frac{\left(\frac{1}{M_{ud}^{(1)}}-\frac{1}{M_{ud}^{(2)}}\right)}{\left(\frac{1}{M_{ud}^{(1)}}-\frac{1}{M^{B}}\right)\left(\frac{1}{M_{ud}^{(2)}}-\frac{1}{M^{B}}\right)}\approx \frac{\left(\frac{1}{M^{f1}}-\frac{1}{M^{f2}}\right)+\frac{\phi_f}{\phi_m}\xi^{m1f1}\xi^{m2f2}\left(\frac{1}{M^{m1}}-\frac{1}{M^{m2}}\right)}{\phi_f\left(\frac{1}{M^{f1}}-\frac{1}{M^{B}}+\left(\frac{1}{M^{m1}}-\frac{1}{M^{B}}\right)\xi^{m1f1}\right)\left(\frac{1}{M^{f2}}-\frac{1}{M^{B}}+\left(\frac{1}{M^{m2}}-\frac{1}{M^{B}}\right)\xi^{m2f2}\right)} \tag{33}$$

,

In equation 33, if we replace M with K and ξ^{mf} with $\left(\phi_m\overline{P^m}\right)/\left(\phi_f\overline{P^f}\right)$ we obtain the equation for bulk modulus, whereas if we replace M with μ and ξ^{mf} and $\left(\phi_m\overline{\tau_{12}^m}\right)/\left(\phi_f\overline{\tau_{12}^f}\right)$ we obtain the equation for shear modulus. Parameters ξ^{mf} describe the averaged stress ratio in phases *f* and *m*. We will now explore the limiting values for parameters ξ^{mf} and put approximate bounds on the problem. Approximating a mix of phases *m* and *f* as a two-phase composite we can write the effective stiffness (Hashin, 1962) as

$$\left(\frac{1}{M^m}-\frac{1}{M_{fm-mix}}\right)\left(1+\xi^{mf}\right)=\left(\frac{1}{M^m}-\frac{1}{M^f}\right), \tag{34}$$

where M_{fm-mix} is the effective stiffness of the two-phase composite. Using the Hashin-Shtrikman (HS) bounds (Hashin and Shtrikman, 1963) on the effective stiffness M_{fm-mix} we obtain the following inequalities:

$$\frac{M^m\left(M_{fm-mix}^{HS+}-M^f\right)}{M^f\left(M^m-M_{fm-mix}^{HS+}\right)}\geq\xi^{mf}\geq\frac{M^m\left(M_{fm-mix}^{HS-}-M^f\right)}{M^f\left(M^m-M_{fm-mix}^{HS-}\right)}, \tag{35}$$

where, M_{fm-mix}^{HS+} and M_{fm-mix}^{HS-} are upper and lower HS bounds on effective modulus for a mix of phases *m* and *f*, respectively. Equations 33 and 35 together describe approximate bounds on change in bulk and shear moduli upon substitution. We refer to these as the

HS- and *HS*+ approximations corresponding to M_{fm-mix}^{HS-} and M_{fm-mix}^{HS+} moduli, respectively. These can be easily extended to model substitution of more than two phases in an *N* phase multimineralic isotropic rock.

FEM example of a heavy-oil rock

As an example of substitution of two phases in a three phase multimineralic rock using equations 33 and 35, we now discuss a numerical example of substitution in a digital bituminous sand sample. This digital sample was imaged, processed and later segmented using a commercially available software. This 3D sample is shown in Figure 35.

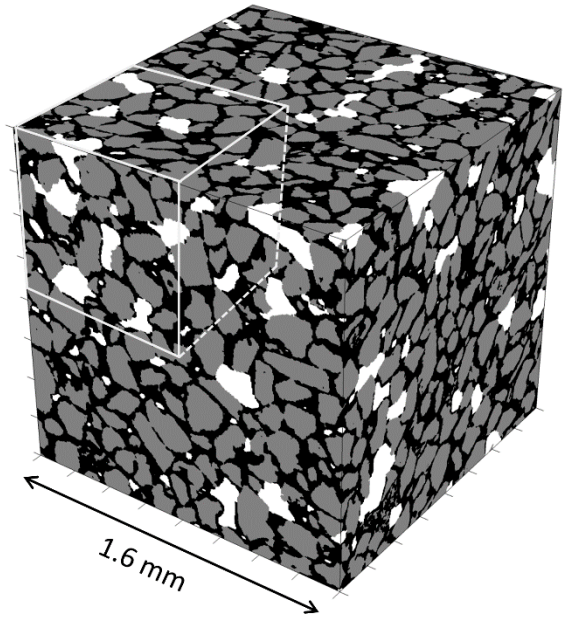

Figure 35: Original bituminous sand sample digital cube of size 1.6 mm; sub-cube of size 0.8 mm is also shown.

Imaging revealed grain size roughly between 0.1 mm-0.25 mm (assumed to be quartz; volume fraction 0.56) and some air-saturated pores (volume fraction of about 0.07) in addition to bitumen-filled pores (volume fraction 0.37). The spatial resolution of this segmented digital rock is 0.004 mm (in x, y and z) and the cube length is 1.6 mm. We populate the digital sample with the following elastic properties: quartz grains of 36 GPa bulk modulus and 45 GPa shear modulus, air as an ideal fluid of bulk modulus 0.005 GPa and bitumen as a soft elastic solid of 4 GPa bulk modulus and 0.5 GPa shear modulus. Next, we numerically compute the effective moduli of subsamples of the digital rock

using the finite element method (FEM). We also re-calculate the effective moduli after digitally replacing both the air-saturated and bitumen-saturated pores with cold bitumen (bulk modulus: 4 GPa; shear modulus 1 GPa). Using the *HS*+ and *HS*- approximations (equations 33 and 35) we predict the change in effective moduli upon substitution of both air-saturated and bitumen-saturated pores with cold bitumen, starting with the initial FEM computed moduli. These predictions are shown in Figures 36a and 36b for bulk and shear moduli, respectively. Comparing these predictions with the FEM computations, we note that most FEM computations, for both bulk and shear, are closer to predictions of the *HS*+ approximation which, in this example, predicts the least change. The range predicted by the *HS*+ and *HS*- approximations is fairly narrow and contains the FEM computations.

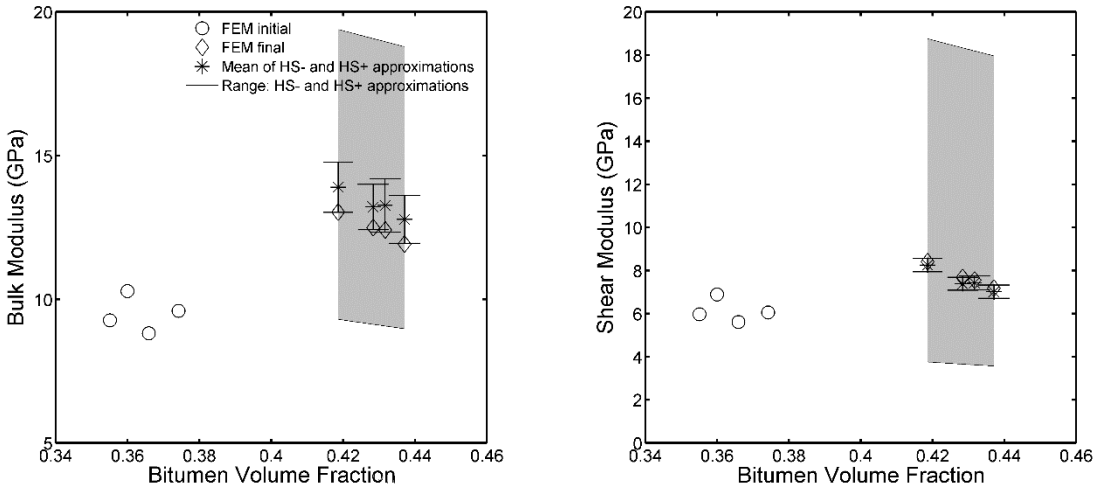

(a) (b)

Figure 36: Predicted bulk (a) and shear (b) moduli of bituminous sand with cold bitumen, starting with the FEM computed moduli of bituminous sand with air and bitumen saturated pores. The range predicted by the Hashin-Shtrikman bounds are shown in gray region.

Laboratory example of permafrost

Figures 37a and 37b show laboratory measured ultrasonic velocities of unconsolidated sand (of porosity around 0.4) as reported by Zimmerman and King (1986). The measured velocities are plotted as a function of ice filled porosity (bulk: 4 GPa; shear: 3.7 GPa), such that the remaining pores are saturated with water (bulk: 2.2 GPa). Assuming quartz (bulk: 36 GPa; shear: 45 GPa) as the predominant mineral in the rock frame, starting with the fully frozen sand sample velocities (i.e., all pores filled with

ice), we predict the velocities corresponding to the partially frozen sand samples, using the approximate bounds in equations 33 and 35. We note that the approximate bounds contain these measured velocities. The *HS*+ approximation predicts the least change upon substitution, and the measurements are relatively closer to the *HS*+ approximation when compared to *HS*- approximation. The range predicted by *HS*+ and *HS*- approximations describes the uncertainty of not knowing in which part of the pore space, ice was being replaced with water. Note that for this problem since the contrast between the elastic properties of quartz and ice is quite large our assumption of $\alpha_1^{f,m} \approx 1$, $\beta_1^{f,m} \approx 1$. $\alpha_2^{f,m} \approx 0$ and $\beta_2^{f,m} \approx 0$ may not be justified.

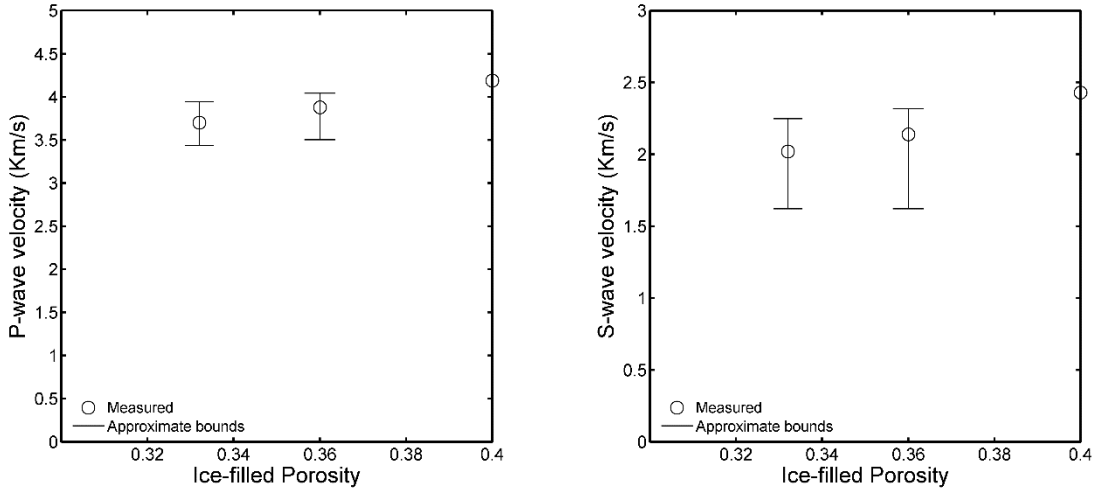

(a) (b)

Figure 37: Predicted P-wave (a) and S-wave (b) velocities of sand samples with partially ice-filled pores, starting with the measured velocities of a sand sample fully filled with ice.

MODELING EFFECTS OF DISSOLUTION OR PRECIPITATION

Exact solutions

Consider a rock of porosity ϕ_f such that the pores are fully filled with a fluid or solid (denoted by superscript f, of bulk modulus K^f and shear modulus μ^f), and the frame is composed of a single mineral/solid (denoted by superscript B, of bulk modulus K^B and shear modulus μ^B). For this rock, let's say that the measured/known bulk and shear moduli are given by $K_{ud}^{(1)}$ and $\mu_{ud}^{(1)}$. Next, suppose we dissolve away a part of the frame mineral such that the newly created pores are also now occupied by the original pore material f; the modified porosity is given by $\phi_f + \phi_m$, where ϕ_m is the volume fraction of the rock mineral now replaced by the pore material. Also, let's assume that the modified (and as yet unknown) bulk and shear moduli are given by $K_{ud}^{(2)}$ and $\mu_{ud}^{(2)}$. A conceptual diagram is shown in Figure 38.

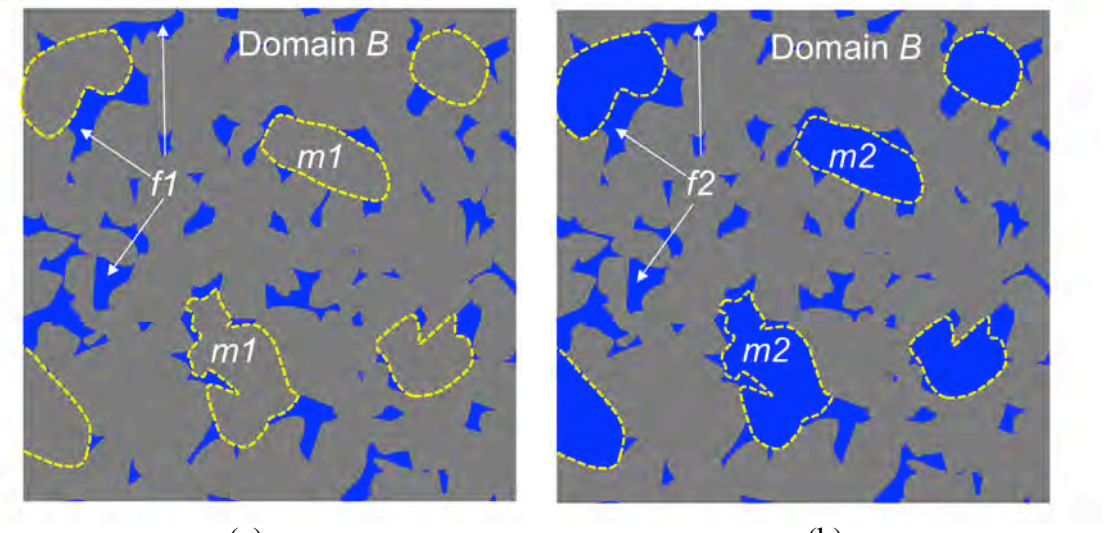

(a) (b)

Figure 38: Conceptual diagram of before (a) and after dissolution (b). Frame solid is shown in gray and pore solid is shown in white. Solid curves represent pore boundaries whereas dashed curves represent imaginary cuts.

For this situation, equations 22 and 27 reduce to the following exact relations

$$\frac{\left(K_{ud}^{(2)}-K_{ud}^{(1)}\right)}{\left(K^B-K_{ud}^{(1)}\right)\left(K^B-K_{ud}^{(2)}\right)}=\frac{\phi_m\left(K^f-K^B\right)\alpha_1^m+\phi_m\left(\mu^f-\mu^B\right)\alpha_2'^m}{\phi_f\left(K^f-K^B\right)^2\left(\dfrac{\overline{e^{f1}}}{\overline{e^{m1}}}\right)\left(\phi_f\dfrac{\overline{e^{f2}}}{\overline{e^{m2}}}+\phi_m\right)}, \tag{36}$$

and

$$\frac{\left(\mu_{ud}^{(2)}-\mu_{ud}^{(1)}\right)}{\left(\mu^B-\mu_{ud}^{(1)}\right)\left(\mu^B-\mu_{ud}^{(2)}\right)}=\frac{\phi_m\left(K^f-K^B\right)\beta_2'^m+\phi_m\left(\mu^f-\mu^B\right)\beta_1^m}{\phi_f\left(\mu^f-\mu^B\right)^2\left(\dfrac{\overline{\gamma_{12}^{f1}}}{\overline{\gamma_{12}^{m1}}}\right)\left(\phi_f\dfrac{\overline{\gamma_{12}^{f2}}}{\overline{\gamma_{12}^{m2}}}+\phi_m\right)}. \tag{37}$$

In equations 36 and 37, parameters $\alpha_1^m, \alpha_2'^m, \beta_1^m$ and $\beta_2'^m$ are given by

$$\alpha_1^m=\frac{\overline{P^{m1}P^{m2}}}{\overline{P^{m1}}\,\overline{P^{m2}}}=\frac{\overline{e^{m1}e^{m2}}}{\overline{e^{m1}}\,\overline{e^{m2}}};\quad \alpha_2'^m=2\frac{\overline{\gamma_{ij}^{m1}\gamma_{ij}^{m2}}}{\overline{e^{m1}}\,\overline{e^{m2}}}, \tag{38}$$

$$\beta_1^m=\frac{1}{2}\frac{\overline{\tau_{ij}^{q1}\tau_{ij}^{q2}}}{\overline{\tau_{12}^{q1}}\,\overline{\tau_{12}^{q2}}}=\frac{1}{2}\frac{\overline{\gamma_{ij}^{m1}\gamma_{ij}^{m2}}}{\overline{\gamma_{12}^{m1}}\,\overline{\gamma_{12}^{m2}}};\quad \beta_2'^m=\frac{1}{4}\frac{\overline{e^{m1}e^{m2}}}{\overline{\gamma_{12}^{m1}}\,\overline{\gamma_{12}^{m2}}}, \tag{39}$$

Note that parameters α_2' and β_2' in equations 38 and 39 are modified versions of parameters α_2 and β_2 (in equations 26 and 28) expressed in terms of induced strains instead of stresses. In the above equations, the original pores before dissolution are denoted as phase *f*1, whereas phase *m*1 denotes the part of the frame mineral (before dissolution) which is to be replaced by the pore material. Phase *f*2 denotes the original pores but after dissolution and phase *m*2 denotes the newly formed pores post dissolution (initially a part of the frame mineral). Thus, $K^{f1}=K^{f2}=K^f, K^{m1}=K^B, K^{m2}=K^f$, and similarly for the shear modulus, $\mu^{f1}=\mu^{f2}=\mu^f$, $\mu^{m1}=\mu^B$, $\mu^{m2}=\mu^f$.

Approximate bounds for weak contrast in substituted phases

To predict the modified effective bulk and shear moduli, we need to know parameters α_1^m, $\alpha_2'^m$, β_1^m, $\beta_2'^m$, and strain ratio parameters $\overline{e^f}/\overline{e^m}$ and $\overline{\gamma_{12}^f}/\overline{\gamma_{12}^m}$. These parameters depend on the detail of initial and final rock microstructure. Parameters $\overline{e^f}/\overline{e^m}$ and $\overline{\gamma_{12}^f}/\overline{\gamma_{12}^m}$ denote the ratio of volume averaged strains in the initial pores and material

occupying the newly made pores. Similar to our discussion in the previous section, we explore the limiting values for these parameters and put approximate bounds on the problem.

Approximating a mix of phases *m1* and *f1* as a two-phase composite, using HS bounds we obtain the following *approximate* inequalities:

$$\frac{\left(K^B - K^{HS+}_{fm-mix}\right)}{\left(K^{HS+}_{fm-mix} - K^f\right)} \le \frac{\phi_f K^B \overline{P^{f1}}}{\phi_m K^f \overline{P^{m1}}} = \frac{\phi_f \overline{e^{f1}}}{\phi_m \overline{e^{m1}}} \le \frac{\left(K^B - K^{HS-}_{fm-mix}\right)}{\left(K^{HS-}_{fm-mix} - K^f\right)}, \tag{40}$$

$$\frac{\left(\mu^B - \mu^{HS+}_{fm-mix}\right)}{\left(\mu^{HS+}_{fm-mix} - \mu^f\right)} \le \frac{\phi_f \mu^B \overline{\tau^{f1}_{12}}}{\phi_m \mu^f \overline{\tau^{m1}_{12}}} = \frac{\phi_f \overline{\gamma^{f1}_{12}}}{\phi_m \overline{\gamma^{m1}_{12}}} \le \frac{\left(\mu^B - \mu^{HS-}_{fm-mix}\right)}{\left(\mu^{HS-}_{fm-mix} - \mu^f\right)}. \tag{41}$$

where, K^{HS+-}_{fm-mix} and μ^{HS+-}_{fm-mix} are upper/lower HS bounds for bulk and shear moduli for a mix of phases *m1* and *f1*, respectively. Approximate inequalities in equations 40 and 41 are conceptually identical to those discussed in equation 35.

Assuming *homogenous* induced stress/strains along with a *weak* elastic contrast between materials *f* and *B*, we can approximate $\alpha_1^m \approx 1$, $\alpha_2'^m \approx 0$, $\beta_1^m \approx 1$ and $\beta_2'^m \approx 0$. For the above case, both phases *f2* and *m2* are occupied by material *f*, thus we can approximate $\overline{e^{f2}} \approx \overline{e^{m2}}$ and $\overline{\gamma_{12}^{f2}} \approx \overline{\gamma_{12}^{m2}}$. Under these assumptions, using the upper HS bound we obtain the *HS+* approximations

$$\frac{\left(K^{(2)}_{ud} - K^{(1)}_{ud}\right)}{\left(K^B - K^{(1)}_{ud}\right)\left(K^B - K^{(2)}_{ud}\right)} = \frac{\phi_m\left(4\mu^B + 3K^f\right)}{\phi_f\left(K^f - K^B\right)\left(4\mu^B + 3K^B\right)\left(\phi_f + \phi_m\right)}, \tag{42}$$

and

$$\frac{\left(\mu^{(2)}_{ud} - \mu^{(1)}_{ud}\right)}{\left(\mu^B - \mu^{(1)}_{ud}\right)\left(\mu^B - \mu^{(2)}_{ud}\right)} = \frac{\phi_m\left(9K^B + 8\mu^B\right)}{\phi_f\left(\mu^f - \mu^B\right)\left(15K^B + 20\mu^B\right)\left(\phi_f + \phi_m\right)}. \tag{43}$$

Similarly, using the lower HS bound, we obtain the *HS-* approximations

$$\frac{\left(K^{(2)}_{ud} - K^{(1)}_{ud}\right)}{\left(K^B - K^{(1)}_{ud}\right)\left(K^B - K^{(2)}_{ud}\right)} = \frac{\phi_m K^f}{\phi_f\left(K^f - K^B\right)K^B\left(\phi_f + \phi_m\right)}, \tag{44}$$

and

$$\mu_{ud}^{(2)} = \mu_{ud}^{(1)} \quad . \tag{45}$$

The *HS*+ (equations 42 and 43) and *HS*- (equations 44 and 45) approximations are approximate bounds which predict the largest and smallest change in rock stiffness upon dissolution, respectively. After calculating change in rock moduli upon change in rock microstructure, pore-fluid can also be replaced using Gassmann's equations 20 and 21.

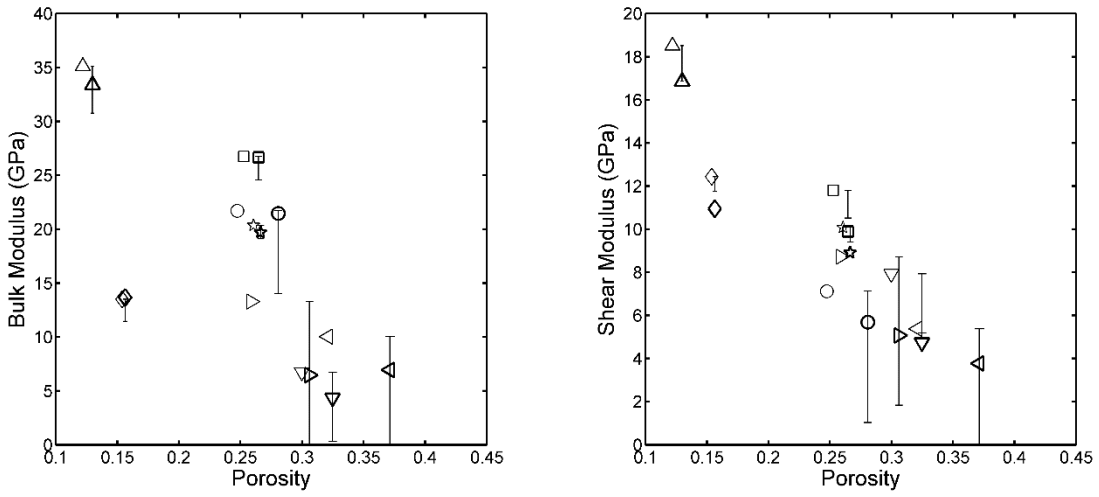

(a) (b)

Figure 39: Predictions of change in elastic moduli upon dissolution for dry carbonate samples from Vialle and Vanorio (2011). Open and filled symbols show measurements before and after dissolutions, respectively. Different symbols show different samples.

Figures 39a and 39b show laboratory measured change in dry rock elastic stiffness of carbonate core samples induced due to dissolution upon injection of carbonated water, reported by Vialle and Vanorio (2011). Since change in volume fraction or porosity was also reported, all inputs needed for the approximate bounds (in equations 42-45) are available. We compare the range predicted by these approximate bounds with the post-dissolution stiffness measurements. These predictions are also shown in Figure 39a and 39b. For all samples, we note that approximate bounds in equations 42-45 fairly contain the laboratory measured change; even though elastic contrast between dry pores and

quartz is quite large for which our assumption of $\alpha_1^m \approx 1$, $\alpha_2'^m \approx 0$, $\beta_1^m \approx 1$ and $\beta_2'^m \approx 0$ may not be justified. Figures 40a and 40b show the same results as in Figures 39a and 39b but for water-saturated samples, also for these samples the effect of change in rock microstructure on stiffness is well contained by the approximate bounds.

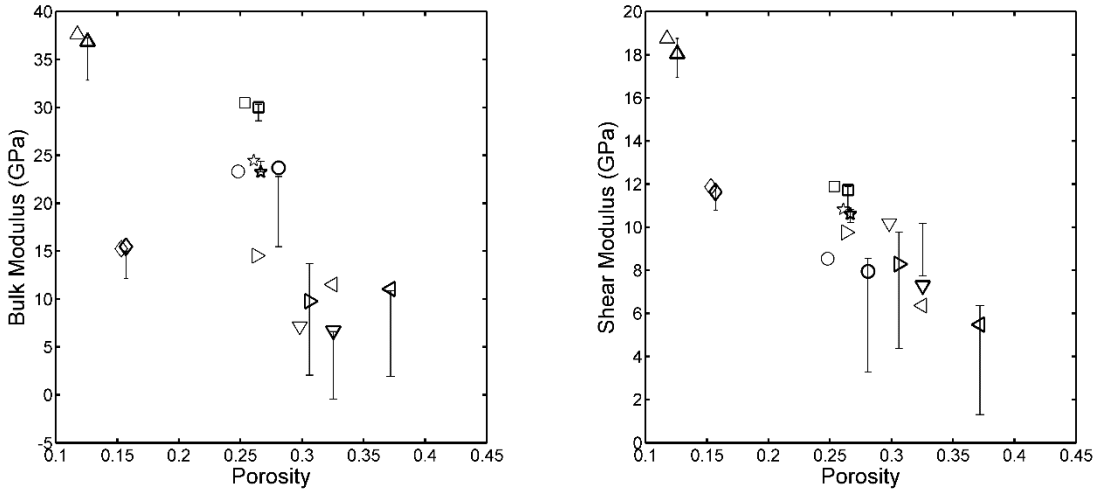

(a) (b)

Figure 40: Predictions of change in elastic moduli upon dissolution for water-saturated carbonate samples from Vialle and Vanorio (2011). Open and filled symbols show measurements before and after dissolutions, respectively. Different symbols show different samples.

We note that for most samples, measured change in elastic stiffness is closer to the *HS*- approximation when compared to the *HS*+ approximation. However, to predict the true change more information on the change in pore geometry is needed, in addition to a measure of change in porosity. We also note that the measured stiffness change of these carbonate core samples, give only an average change in stiffness at the core-scale, but the local changes in stiffness in the core plug can be lower or higher, depending on the local pore geometry, the local flow velocities, the reactive surface area and the local chemistry of the circulating fluid.

Also such dissolution experiments are quite poorly constrained since the final pore structure depends on both local pore fluid velocities and chemical kinetics (Guen et al., 2007, Smith et al., 2013 and Vialle et al., 2014). Dissolution can affect all kind of pores equally or can occur preferentially in the main flow paths; moreover even precipitation can occur in the surrounding "stagnant zones" (Vialle et al., 2013). Therefore, the

measured macroscopic change emerges from complex local processes and thus due to heterogeneities between the rock samples, the changes at the pore scale may not be the same from one rock to another. The approximate bounds (in equations 23-26) only describe a plausible range, and also highlight the uncertainty in estimating the true change in elastic stiffness of a rock upon dissolution.

Equations 22 and 27 are the main results of this section; these are the exact fluid/solid substitution relations for substitution of one or more phases in a $N\ (\geq 1)$ phase isotropic multimineralic rocks (but substitution of no more than N - 1 phases). Since these exact equations allow for replacing one or more phases, the rock microstructure does not have to remain invariant upon substitution, as assumed by Brown and Korringa. In addition to the usually known parameters, like volume fractions, properties of rock constituents, etc., these equations depend on parameters which are usually not known unless detailed information on rock microstructure is available; however these parameters have a clear physical interpretation and are directly linked to the ratios of volume averaged stresses/strains induced in rock constituents. Due to a number of required parameters, modeling the change in rock stiffness upon substitution or mineral dissolution is inherently non-unique unless detailed information on pore geometry is available. Therefore, the required parameters must be approximated on the case by case basis.

In equations 33 and 35, we discuss approximate bounds for substitution of one or more phases simultaneously; these predictions are in good agreement with the examples discussed in this section. Similarly, approximate bounds are also developed for predicting change in rock stiffness upon dissolution in equations 42-45. These predictions fairly contain laboratory measured change in rock stiffness. The range predicted by these approximate bounds highlights the uncertainty associated with not knowing the details of the rock microstructure.

REFERENCES

Andrä, H., N. Combaret, J. Dvorkin, E. Glatt, J. Han, M. Kabel, Y. Keehm, F. Krzkilla, M. Lee, C. Madonna, M. Marsh, T. Mukerji, E. H. Saenger, R. Sain, N. Saxena, S. Ricker, A. Wiegmann and X. Zhan, 2013, Digital rock physics benchmarks - Part I: Imaging and segmentation: Computers & Geosciences, 50, 25-32.

Arts, R., Brevik, I. Eiken, O. Sollie, R. Causse, E. & van der Meer, L. 2000, Geophysical methods for monitoring marine aquifer CO_2 storage — Sleipner experiences. In: Williams, D. J., Durie, R. A., McMullan, P., Paulson, C. A. J. & Smith, A. Y. (eds) Greenhouse Gas Control Technologies, CSIRO Publishing Collingwood, Australia, 366–371.

Arts, R., Eiken, O., Chadwick, R.A., Zweigel, P., Van Der Meer, L., and Kirby, G.A., 2004, Seismic monitoring at the Sleipner underground CO_2 storage site (North Sea). in: Geological Storage for CO2 emissions reduction, S. Baines, J. Gale and R.J. Worden, ed., Special Publication of the Geological Society, London, 233, pp. 181–191.

Avseth, P., T. Mukerji, and G. Mavko, 2005, Quantitative seismic interpretation: Applying rock physics tools to reduce interpretation risk: Cambridge University Press.

Avseth, P., T. Mukerji, G. Mavko, and J. Dvorkin, 2010, Rock physics diagnostics of depositional texture, diagenetic alterations and reservoir heterogeneity in high porosity siliciclastic sediments and rocks — A review of selected models and suggested workflows: Geophysics, 75, 5, 75A31–75A47.

Bemer, E., J. Dautriat, M. Fleury and M. Adelinet, 2013, Experimental characterization of chemical alteration effects on carbonate rock dynamic poroelastic properties: Poromechanics V, 1644-1653.

Berryman, J. G., 1980, Long-wavelength propagation in composite elastic media: Journal of the Acoustical Society of America, 68, 1809–1831.

Berryman, J. G. , 1999, Origin of Gassmann's equations: Geophysics, 64, 1627–1629.

Bianco, E., S. Kaplan, and D. Schmitt, 2008, Seismic rock physics of steam injection in bituminous oil reservoirs: The Leading Edge, 27(9), 1132-1137.

Birch, F., 1960, The velocity of compressional waves in rocks to 10 kilobars, Part1: Journal of Geophysical Research, 65, 1083-1102.

Bourbié, T. and B. Zinszner, 1985, Hydraulic and acoustic properties as a function of porosity in Fontainebleau Sandstone:Journal of Geophysical Research, v. 90, n. B13, p.11,524-11,532.

Brown, R., and J. Korringa, 1975, On the dependence of the elastic properties of a porous rock on the compressibility of the pore fluid: Geophysics, 40, 608–616.

Cadoret, T., 1993. Effet de la Saturation Eau/Gaz sur les Proprie´te´s Acoustiques des Roches. Ph.D. dissertation, University of Paris, VII.

Carman, P. C., 1961, L'écoulement des gaz á travers les milieux, 1961, Bibliothèque des Sciences et Techniques Nucléaires, Presses Universitaires de France, Paris.

Chadwick, R.A., Arts, R., and Eiken, O., 2005, 4D seismic quantification of a growing CO_2 plume at Sleipner, North Sea, in: Petroleum Geology: North West Europe and Global Perspectives-Proceedings of the 6th Petroleum Geology Conference. A.G. Dore and B. Vining, eds, Published by the Geological Society, London, pp. 1385–1399.

Chopra, S., L. Lines, D. Schmitt, and M. Batzle, 2010, 1. Heavy-Oil Reservoirs: Their Characterization and Production: Heavy Oils, 1-69.

Ciz, R., and S. A. Shapiro, 2007, Generalization of Gassmann equations for porous media saturated with a solid material: Geophysics, 72, A75–A79.

Cleary, M. P., I. W. Chen and S. M. Lee, 1980, Self-consistent techniques for heterogeneous media: ASCE Journal of Engineering Mechanics, 106, 861-887.

Cremonini, G., C. Elmi and R. Selli, 1971, Note illustrative della carta geologica d'Italia, Foglio 156 "S. Marco in Lamis": Servizio Geologico d'Italia, Roma, 66p.

Daley TM, Myer LR, Peterson JE, Majer EL, Hoversten GM (2007) Time-lapse crosswell seismic and VSP monitoring of injected CO_2 in a brine aquifer. Environ Geol, 2007.

Deville de Periere, M., C. Durlet, E. Vennin, L. Lambert, R. Bourillot, B. Caline, and E. Poli, 2011, Morphometry of micrite particles in cretaceous microporous limestones of the Middle East: Influence on reservoir properties, Marine and Petroleum Geology, 28(9), 1727-1750, ISSN 0264-8172, 10.1016/j.marpetgeo.2011.05.002.

de Marsily, G., 1986, Quantitative Hydrogeology – Groundwater Hydrology for Engineers. Academic Press. New York.

Dunham, R. J., 1962, Classification of carbonate rocks according to depositional texture, in W. E. Ham, ed., Classification of carbonate rocks: AAPG Memoir, 108–121.

Dullien, F. A. L., 1992. Porous Media: Fluid Transport and Pore Structure. San Diego, CA: Academic Press.

Duputel, Z., V. Ferrazzini, F. Brenguier, N. Shapiro, M. Campillo, and A. Nercessian, Real time monitoring of relative velocity changes using ambient seismic noise at the Piton de la Fournaise volcano (La Reunion) from January 2006 to June 2007, Journal of Volcanology and Geothermal Research, 184, 164-173.

Dvorkin, J., and A. Nur, 1996, Elasticity of high-porosity sandstones: Theory for two North Sea data sets: Geophysics, 61, 1363–1370.

Folk, R. L., 1959, Practical petrographic classification of limestones: The AAPG Bulletin, 43, 1–38.

Gassmann, F., 1951, Über die Elastizität poröser Medien: Vierteljahrschrift der Naturforschenden Gessellschaft in Zürich, 96, 1-23.

Gomez, T. C., J. Dvorkin, and T. Vanorio, 2010, Laboratory measurements of porosity, permeability, resistivity, and velocity on Fontainebleau sandstones, Geophysics 75, E191 (2010); doi:10.1190/1.3493633.

Han, G, 1986, Effects of porosity and clay content on acoustic properties of sandstones and unconsolidated sediments, PhD dissertation, Stanford University.

Han, G., and M. Batzle, 2004, Gassmann's equation and fluid-saturation effects on seismic velocities: Geophysics, 69, 2, 398-405.

Hashin, Z., 1962, The elastic moduli of heterogeneous materials, Journal of Applied Mechanics, 29, 143-150.

Hashin, Z., and S. Shtrikman, 1963, A variational approach to the elastic behavior of multiphase materials: Journal of the Mechanics and Physics of Solids, 11, 127–140.

Hebach, A., Oberhof A. and Dahmen N., 2004, Density of Water + Carbon Dioxide at Elevated Pressures: Measurements and Correlation: J. Chem. Eng. Data, 49(4), 950-953.

Hickey, C.J., Spanos, T.J.T., and de la Cruz, V., 1995, Deformation parameters of permeable media, Geophysical Journal International, 121, 359-370.

Hoefiner, M. L., and H. S. Fogler, 1988, Pore evolution and channel formation during flow and reaction in porous media: AIChE Journal, 34, 1, 45–54.

Hovorka, S., 2009, Frio brine pilot: The first U. S. sequestration test: Southwest Hydrology, 8, no. 5, 26– 31.

Jacoby, M., J. Dvorkin, and X. Liu, 1996, Elasticity of partially saturated frozen sand, Geophysics, 61(1), 288-293.

Joy, C., Vanorio, T., and Sen, M., 2011, differentiating chemical effects and pressure effects on the elastic properties of the Lower Tuscaloosa sandstone in Cranfield, Mississippi, by injectiong carbon dioxide rich brine: SEG Extended Abstract

Karamalidis, A., J. A. Hakala, C. Griffith, S. Hedges, and J. Lu, 2010, Laboratory investigation of CO2 — Rock-brine interactions using natural sandstone and brine samples from the SECARB Tuscaloosa injection zone: Geological Society of America Annual Meeting, Paper no. 86-10.

Katz, A.J., and Thompson A.H., 1986, Quantitative prediction of permeability in porous rock: Physical Review, B34, 8179-8181.

King, M. S., 1977, Acoustic velocities and electrical properties of frozen sandstones and shales: Canadian Journal of Earth Sciences, 14, 1004–1013.

King, M. S. , R. W. Zimmerman, and R. F. Corwin, 1988, Seismic and electrical properties of unconsolidated permafrost: Geophysical Prospecting, 36, 349–364.

Kolodzie, S., Jr., 1980, Analysis of pore throat size and use of the Waxman-Smits equation to determine OOIP in Spindle Field, Colorado: Society of Petroleum Engineers, 55th Annual Fall Technical Conference, Paper SPE-9382, 10 p.

Kurfurst, P. J., 1976, Ultrasonic wave measurements on frozen soils at permafrost temperatures: Canadian Journal of Earth Sciences, 13, 1571–1576.

Kuster, G. T., and M. N. Toksöz, 1974, Velocity and attenuation of seismic waves in two phase media: Part I. theoretical formulations: Geophysics, 39, 587-606.

Lambert, L., C. Durlet, J.P. Loreau, and G. Marnier, 2006. Burial dissolution of micrite in Middle East carbonate reservoirs (Jurassic-Cretaceous): keys for recognition and timing. Marine and Petroleum Geology 23, 79-92.

Le Guen, Y., F. Renard, R. Hellmann, E. Brosse, M. Collombet, D. Tisserand, and J.P. Gratier, 2007, Enhanced deformation of limestone and sandstone in the presence of high PCO2 fluids: Journal of Geophysical Research, 112, B05421.

Liu, L., 2011, New optimal microstructures and restrictions on the attainable Hashin-Shtrikman bounds for multiphase composite materials, Philosophical Magazine Letters.

Lu, J., Y. K. Kharaka, D. R. Cole, J. Horita, and S. Hovorka, 2009, Reservoir fluid and gas chemistry during CO2 injection at the Cranfield field, Mississippi, USA

Lumley, D., 2010, 4D seismic monitoring of CO2 sequestration: The Leading Edge, 29, 150–155.

Martinis, B., and G. Pavan, 1967, Note illustrative della carta geologica d'Italia, Foglio 157 "Monte S. Angelo": Servizio Geologico d'Italia, Roma, 56p.

Masson, Y. J., and Pride, S. R., 2007, Poroelastic finite difference modeling of seismic attenuation and dispersion due to mesoscopic-scale heterogeneity: Journal of Geophysical Research, 112.

Mavko, G., C. Chan, and T. Mukerji, 1995, Fluid substitution: Estimating changes in Vp without knowing Vs: Geophysics, 60, 1750–1755.

Mavko, G., Mukerji, T., and Dvorkin, 2009, The Rock Physics Handbook, 2nd Edition, Cambridge University Press.

Moshier, S.O., 1989, Microporosity in micritic limestones: a review, Sedimentalogy Geology, 63, 191-213.

O'Connell, R. J., B. Budiansky, 1974, Seismic velocities in dry and saturated cracked solids: Journal of Geophysical Research, 79, 5412-5426.

Pittman, E.D., 2001, Estimating pore throat size in sandstones from routine core-analysis data: Search and Discovery Article 40009: http:www.searchanddiscovery.net/documents/pittman/index.htm.

Robinson, R.B., 1966, Classification of reservoir rocks by surface texture: AAPG Bulletin, 50, 547-559.

Rumpf, H. and Gupte, A.R., 1971. Einflu¨sse der Porosita¨t und Korngro¨ssenverteilung im Widerstandsgesetz der Porenstro¨mung. Chem-Ing.-Tech., 43, 367–375.

Saxena, N., and G. Mavko, 2014, Exact equations for fluid and solid substitution: Geophysics, 79(3), L21-L32.

Schmitt, D., 1999, Seismic attributes for monitoring of a shallow heated heavy oil reservoir: A case study, Geophysics, 64(2), 368-377.

Scotellaro, C., T. Vanorio, and G. Mavko, 2008, The effect of mineral composition and pressure on carbonate rocks: 77th Annual International Meeting, SEG, Expanded Abstracts, 26, 1684–1689.

Schowalter, T.T., 1979, Mechanics of secondary hydrocarbon migration and entrapment: AAPG Bulletin, 63, 723-760.

Smith, M., Y. Sholokhova, Y. Hao, S. Carroll, 2013, CO_2-induced dissolution of low permeability carbonates. Part I: Characterization and Experiments: Advances in Water Resources, 62, 370–87.

Sondergeld, C. and C. Rai, 2007, Velocity and resistivity changes during freeze-thaw cycles in Berea sandstone: Geophysics, 72(2), E99-E105.

Swanson, B.F., 1977, Visualising pores and non-wetting phase in porous rocks: Society of Petroleum Engineers, Annual Fall Technical Conference, SPE Paper 6857, 10p.

Timur, A., 1968, Velocity of compressional waves in porous media at permafrost temperatures: Geophysics, 33, 584-595.

Van der Meer L.G.H., R.J. Arts and L. Peterson, Prediction of migration of CO_2 after injected into a saline aquifer: reservoir history matching of 4D seismic image with a compositional gas/water model. In: D. Williams, B. Durie, M. McMullan, C. Paulson and A. Smith, Editors, Proceedings of the Fifth International Conference on Greenhouse Gas Reduction Technologies, , CSIRO, Collingwood, Australia (2001).

Vanorio, T., C. Scotellaro, and G. Mavko, 2008, The effect of chemical and physical processes on the acoustic properties of carbonate rocks: The Leading Edge, 27, 1040–1048.

Vanorio T., and Mavko G., 2011, The Effect of Microstructure on the Acoustic Properties of Carbonate Rocks: Geophysics 76, 105-115

Vanorio, T, and Mavko G., 2009, How micrite content affects the transport, seismic, and reactive properties of carbonate rocks. Implications for 4D seismic: SEG Expanded Abstracts 28, 2030.

Vanorio, T., A. Nur, and Y. Ebert, 2011, Rock physics analysis and time-lapse rock imaging of geochemical effects due to the injection of CO2 into reservoir rocks, Geophysics 76, O23, DOI:10.1190/geo2010-0390.1

Vialle, S., and T. Vanorio, 2011, Laboratory measurements of elastic properties of carbonate rocks during injection of reactive CO_2-saturated water: Geophysical Research Letters, 38, L01302, doi:10.1029/ 2010GL045606.

Vialle S., J. Dvorkin, and G. Mavko, 2013, Implications of pore microgeometry heterogeneity for the movement and chemical reactivity of CO2 in carbonates: Geophysics, 78(5), L69-L86.

Vialle, S., S. , Contraires, B. , Zinzsner, J. B. Clavaud, K. Mahiouz, P. Zuddas and M. Zamora, 2014, Percolation of CO2-rich fluids in a limestone sample: evolution of hydraulic, electrical, chemical and structural properties: Journal of Geophysical Research, Solid Earth, In print.

White, J.E., 1975. Computed seismic speeds and attenuation in rocks with partial gas saturation. Geophys., 40, 224–232.

Wu, T. T., 1966, The effect of inclusion shape on the elastic moduli of a two-phase material: International Journal of Solids and Structures, 2, 1-

Zimmerman, R. W. and M. S. King, 1986, The effect of the extent of freezing on seismic velocities in unconsolidated permafrost: Geophysics, 51, 1285-1290.

Zimmerman, R.W., 1991. Compressibility of Sandstones, in Development in Petroleum Science, vol. 29, ed. Chilingarran, G. V., Elsevier, Amsterdam.

BIBLIOGRAPHY

Andrä, H., N. Combaret, J. Dvorkin, E. Glatt, J. Han, M. Kabel, Y. Keehm, F. Krzkilla, M. Lee, C. Madonna, M. Marsh, T. Mukerji, E. H. Saenger, R. Sain, N. Saxena, S. Ricker, A. Wiegmann and X. Zhan, 2013, Digital rock physics benchmarks - Part I: Imaging and segmentation: Computers & Geosciences, 50, 25-32.

Andrä, H., N. Combaret, J. Dvorkin, E. Glatt, J. Han, M. Kabel, Y. Keehm, F. Krzkilla, M. Lee, C. Madonna, M. Marsh, T. Mukerji, E. H. Saenger, R. Sain, N. Saxena, S. Ricker, A. Wiegmann and X. Zhan, 2013, Digital rock physics benchmarks - Part II: Computing effective properties: Computers & Geosciences, 50, 25-32Grombacher, D., Vanorio, T., Ebert, Y., 2012, Time-lapse acoustic, transport, and NMR measurements to characterize microstructural changes of carbonate rocks during injection of CO2-rich water: Geophysics, 77, WA169-WA179.

Joy, C., Vanorio, T., and Sen, M., 2011, differentiating chemical effects and pressure effects on the elastic properties of the Lower Tuscaloosa sandstone in Cranfield, Mississippi, by injectiong carbon dioxide rich brine: SEG Extended Abstract

Mavko, G. and N. Saxena, 2013, Embedded-bound method for estimating the change in bulk modulus under either fluid or solid substitution: Geophysics, 78, 5, L87-L99.

Saxena, N., and G. Mavko, 2014, Exact equations for fluid and solid substitution: Geophysics, 79(3), L21-L32.

Saxena, N., and G. Mavko, 2014, Predicting Change in P-wave Modulus upon Substitution with Missing S-wave Modulus: Geophysics, in progress.

Saxena, N., Mavko, G., Mukerji, T., 2013, Change in effective bulk modulus upon fluid or solid substitution: Geophysics; 78, L45-L56.

Vanorio, T., C. Scotellaro, and G. Mavko, 2008, The effect of chemical and physical processes on the acoustic properties of carbonate rocks: The Leading Edge, 27, 1040–1048, doi:10.1190/1.2967558.

Vanorio, T., Mavko, G., 2011, Laboratory measurements of the acoustic and transport properties of carbonate rocks and their link with the amount of microcrystalline matrix: Geophysics, 76, E105-E11.

Vanorio, T., Ebert, Y., and Nur, A., 2011, Rock physics analysis and time-lapse imaging of geochemical effects due to the injectin of CO2 into reservoir rocks: Geophyics, 76, 23-33.

Vanorio, T., Ebert, Y., and Grombacher, D., 2014, What laboratory-induced dissolution tell us about natural diagenetic ttrends of carbonate rocks: *in Agar, S. M. & Geiger, S. (eds), Fundamental Controls on Fluid Flow in Carbonates. Geological Society, London, Special*

Vialle, S., Vanorio, T., 2011, Laboratory measurements of elastic properties of carbonate rocks during injection of reactive CO2-saturated water: Geophysical Research Letters, 38

Vialle, S., Dvorkin, J., Mavko, G., 2013, Implications of pore microgeometry heterogeneity for the movement and chemical reactivity of CO2 in carbonates: Geophysics, 78, L69-L86.

LIST OF ACRONYMS AND ABBREVIATIONS

EDTA	Ethylenediaminetetraacetic acid
SI	"Le Systeme International d'Unites."
MPa	Mega Pascals (pressure)
SEM	Scanning electron microscope
CT-scan	Computed tomography X-ray image
MIP	Mercury intrusion porosimetry
ϕ, Φ	porosity
ρb	bulk density
V_P	P-wave velocity
V_S	P-wave velocity